Measurement of the Dijet Transverse Thrust Distribution in Proton-Antiproton Collisions

María Verónica Sorin

Advisor: Ricardo Piegaia

Co-advisor: Daniel Elvira

This dissertation presents the first measurement in a hadron collider of an event shape variable, the Dijet Transverse Thrust T_2^t, which is sensitive to the spatial jet distribution on the plane perpendicular to the colliding $p\overline{p}$ beams. T_2^t is calculated with the two most energetic jets reconstructed with the $k_\perp$ algorithm, and it ranges from $T_2^t = 1$, for a pencil-like configuration, to $T_2^t = \sqrt{2}/2$, for two equal energy jets at 90°. The measurement is based on 87.3 pb^{-1} of data collected with the DØ detector at the Fermilab Tevatron $p\overline{p}$ Collider. The cross section is reported as a function of $1 - T_2^t$ and $\log(1 - T_2^t)$, which enhances the high statistics $T_2^t \rightarrow 1$ region, and presented for four separate event energy ranges. The measurement is in good agreement with a fixed-order $O(\alpha_s^3)$ perturbative QCD prediction, except at high T_2^t, where resummation corrections are expected to be important, and below $T_2^t \simeq \sqrt{3}/2$, where the leading order diagrams contributing to T_2^t are $O(\alpha_s^4)$. The data also show a very good level of agreement with a recent Next-to-Leading pQCD three jet generator which covers the full T_2^t range, except for the T_2^t=1 point.

Keywords: Quantum chromodynamics, $k_\perp$ algorithm, Event Shapes.

2003

Acknowledgments

I am immensely grateful to my advisor, Ricardo Piegaia. His vast knowledge both in experimental and theoretical physics has always astonished me. What I find invaluable is his enthusiasm and love for his work which he shares every day with his students. He has always been supportive and understanding and I appreciate enormously the confidence he has shown on my work.

This work would have not been possible without the help and support of my co-advisor Daniel Elvira. He has guided me throughout all the steps of this analysis. His knowledge and understanding of the many aspects involved in the complex environment of a high energy experiment were always astounding to me.

During my stay at DØ I had the opportunity to work with many people, among them Gaston Gutierrez. He is the most persevering physicist I know. His temperament and dedication to work were inspiring. I am very grateful to Emanuela Barberis, John Hobbs and Harry Melanson for their support.

I would like to thank the Editorial Board of the analysis (Brad Abbott, Tim Bolton, Anna Goussiou, Roger Moore, Thomas Nunnemann and Bob McCarthy) specially to Brad Abbott for being always supportive. Special thanks to Kate Frame and Rob Snihur, with whom I have shared the $k_\perp$ experience. I also appreciate the discussions and input from the QCD conveners and group, specially from John Krane.

I would also like to thank the DØ spokepersons, Harry Weerts and John Womersley and to Gene Fisk for his support that made possible my stay at Fermilab.

Many thanks to the Physics Department of the University of Buenos Aires, the Fermi National Accelerator Laboratory and Fundación Antorchas.

I dedicate this last paragraph to thank all the nice people I met at Fermilab, friends such as Irene, Florencia, Gervasio, Rocio, Aurelio, Cecilia and Carlos helped me throughout my stay at Fermilab. I cannot forget my friends from the University of Buenos Aires, with whom I have shared the best moments, Marina, Luciana, Mariana, Yanina, Dolores, Irene, Alejandra, Andrés, Lucas, Daniel, Richie, Marcos and, from the bottom of my heart, many thanks to my dearest friend Sara.

Contents

Chapter 1

Introduction

Elementary particle physics or High Energy physics is the subject that studies the constituents of matter and their interactions. An enormous progress has been made in this field during the last 30 years, and series of important experimental discoveries has established the existence of a subnuclear world. Nowadays, we view matter as conformed of what is called elementary particles, very small on size, much smaller than an atomic nucleus ($\sim 10^{-15}$m), and indivisible. These particles are grouped into quarks and leptons. Their dynamics is believed to be described by quantum field theories possessing local gauge symmetry. They interact through the exchange of gauge field quanta (photons, gluons and weak boson). The descriptions of these particles and their interactions is given by the Standard Model. It includes the *electroweak theory*, which describes the electromagnetic and weak interactions of leptons and quarks; and *quantum chromodynamics* (QCD) which describes the strong interactions of quarks and gluons. The predictions of this model are day by day put to test by means of different experimental techniques. One of the modern facilities built for this purpose is the Tevatron (Illinois, USA), a $p\overline{p}$ collider that started operations in 1985. DØ , an international collaboration of around 500 physicists from different institutions, one of them being the University of Buenos Aires, is one of the two experiments in the accelerator complex which has been designed to study physics at very high energy ($\sim$ 2 TeV at the center–of–mass). A major feature of this collider is jet production. When two hadrons collide, the outgoing quarks and gluons hadronize to form jets of particles. Jet and event shape measurements provide some of the cleanest tests of QCD predictions.

This work presents the first measurement of the Thrust cross section in proton–antiproton collisions at $\sqrt{s} = 1.8$ TeV in the Tevatron using the DØ detector. This event shape variable, previously studied at e^+e^- and ep colliders, has been modified in order to overcome the difficulties presented due to the busy environment of a hadron collider. The actual observable is called the Dijet Transverse Thrust. Its definition will be presented in this chapter together with a theoretical introduction. Since the variable is measured using jets, the algorithms applied to define them are also discussed, which special emphasis on $k_\perp$ jets. Chapter 2 contains the description of the Fermilab accelerator complex and the DØ detector. The energy calibration method developed for $k_\perp$ jets and the studies done to select the variable to measure are presented in Chapters 3 and 4. The methods and techniques applied in data analysis to obtain the physical quantity of interest are explained from Chapter 5 through 7. The latter includes also an analysis of the sources of systematic uncertainties relevant for this work. Final results and comparisons with theoretical predictions are presented in Chapter 8.

1.1 The Standard Model

The Standard Model [1] is a theory of interacting quantum fields, which describes what we believe are the constituents of matter and their interactions. Within this model, the fundamental building blocks of the universe consist of particles called leptons and quarks. Their interaction occurs by means of force carrier particles called bosons. The four fundamental forces acting among particles are the strong, weak, electromagnetic and gravitational force. One of the major features of the Standard Model is the fact that it treats the weak force and electromagnetism in a unified manner. These two forces are often referred to collectively as the 'electroweak' force.

Tables 1.1 and 1.2 show the particle types of the Standard Model. They are divided in three groups: leptons, quarks and gauge bosons. The first two are particles of spin 1/2 and they conform what we call matter. They are grouped into three generations, with similar properties except that masses increase with each successive generation. Ordinary matter is composed by particles of the first generation, the other ones are produced in high energy interactions.

Each generation of leptons is composed of a charged particle and a neutrino of the corresponding type, which is neutral. Leptons can interact by the electromagnetic and the weak force, while neutrinos are affected only by the weak interaction.

Quarks have two major features which qualitatively separate them from leptons. First, they have fractional electric charge. Second, they carry *color charge* which has three possible values, conventionally called 'red,' 'green,' and 'blue'. They are therefore affected by the strong force (also by the electromagnetic and weak forces), which binds quarks together inside nuclei, and is described in more detail below.

Leptons				**Quarks**			
Symbol	Name	Mass (GeV)	Charge (e)	Symbol	Flavor	Mass (GeV)	Charge (e)
$\mathbf{e}$	electron	0.0005	-1	$\mathbf{u}$	up	0.003	2/3
$\boldsymbol{\nu_e}$	electron neutrino	$< 3\,10^{-9}$ (?)	0	$\mathbf{d}$	down	0.006	$-1/3$
$\boldsymbol{\mu}$	muon	0.106	-1	$\mathbf{c}$	charm	1.3	2/3
$\boldsymbol{\nu_\mu}$	muon neutrino	$< 1.9\,10^{-4}$ (?)	0	$\mathbf{s}$	strange	0.1	$-1/3$
$\boldsymbol{\tau}$	tau	1.777	-1	$\mathbf{t}$	top	175	2/3
$\boldsymbol{\nu_\tau}$	tau neutrino	< 0.018 (?)	0	$\mathbf{b}$	bottom	4.3	$-1/3$

Table 1.1: The fundamental constituents of matter in the Standard Model [2].

Force	Gauge Boson		Mass	Charge
	Symbol	Name	(GeV)	(e)
Electromagnetic	$\boldsymbol{\gamma}$	photon	0	0
Weak	$\boldsymbol{W}$	W	80.425	± 1
	$\boldsymbol{Z}$	Z	91.187	0
Strong	$\boldsymbol{g}$	gluon	0	0

Table 1.2: Gauge Bosons, the force carriers of the Standard Model [2].

Gauge bosons are responsible for the interactions between particles. Electromagnetism ('quantum electrodynamics' or 'QED'), for example, is mediated by the photon, which couples to particles which have electric charge. The strength of this coupling changes with the energy involved in the interaction. This property is called *running coupling* and it is a general feature of interactions in the Standard Model. In this case it grows as the energy increases. The weak interaction is mediated by the massive W and Z gauge bosons. The range of this force is short ($\sim 10^{-16}$ cm) and, at energies of the order or above the exchanged gauge boson mass, the strength of the interaction is comparable to the electromagnetic one.

The strong force is described by quantum chromodynamics (QCD) [3]. In an analogy with the QED formalism, its interactions are mediated by gluons and its strength is given by the value of the strong coupling parameter, α_s. In order to explain the existence of certain observed particles (like the Δ^{++}) satisfying the Pauli exclusion principle, a new quantum degree of freedom is needed. Its named is *color* and comes in three states, 'red', 'green' and 'blue'. QCD is a gauge field theory with a local symmetry described by the SU(3) color group.

As it is the case for the electromagnetic interaction, the value of the strong coupling runs. However, the direction of the effect is different: as the energy of the interaction increases, the strength of the coupling gets smaller. This important property, called *asymptotic freedom*, allows quarks to behave nearly like free particles at very high energies ($E \gtrsim 10\,\mathrm{GeV}$), allowing the application of perturbative techniques, as the ones used for electromagnetism. That is the realm of pQCD (perturbative QCD). QCD cross sections are calculated as power series on the strong coupling constant. The contributions of each order can be represented by Feynman diagrams, which are combination of fundamental interaction vertices joined by propagators. The fundamental vertices are shown in Figure 1.1. Quarks are represented by straight solid lines and gluons by helixes. Since gluons are coloured, they can interact with each other giving rise to vertices of three and four gluons. A given cross section is obtained as the absolute value squared of the sum of all contributing matrix elements integrated over the available phase space.

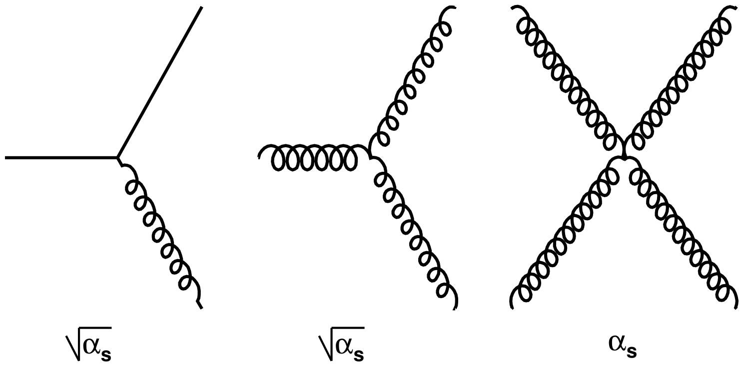

Figure 1.1: Fundamental QCD vertices.

The fact that the strength of the strong interaction increases as the energy of the interaction decreases, or equivalently, as the distance scale of the interaction increases, indicates that at large distances, quarks and gluons (often collectively called partons) are always bound together due to the strength of the coupling between them, and can never be seen as isolated particles. This is referred to as *color confinement* [4] and it states that only color–neutral states, color singlets, can exists at large distances. Quarks bind together creating hundreds of composite particles

called hadrons, divided in baryons, composed of three quarks, and mesons, consisting of a quark and an antiquark.
The other force, gravity, is supposed to be mediated by the graviton but so far there is no evidence of its existence. At present there is no workable theory of quantum gravity.
The set of elementary particles listed in 1.1 is completed with the anti–particles associated with each type. There is another boson, the Higgs , which awaits discovery. While the photon, which carries electromagnetic forces, is massless, the Z and W particles are heavy. The Higgs boson field is the mechanism which extends the Standard Model to explain how particles (fermions and gauge bosons) acquire the properties associated with mass. The Higgs boson is the exchanged particle represented this field. It is expected to be found in Run II of the Tevatron at Fermilab or when the Large Hadron Collider starts operations at CERN (European Organization for Nuclear Research).

1.2 Jet Physics

As it was stated before, the Standard Model proposes a scheme where matter is composed of elementary particles called leptons and quarks. Quarks and gluons, the mediators of the strong force, are bound into colorless states, called baryons and mesons. The hard scattering among partons can be calculated using pQCD techniques. However, color confinement does not allow a direct experimental test of the parton level hard scattering.
A high energy hadron collision will result in a hard scattering of typically one parton of each hadron. As the distance between an ejected parton and the parent hadron increases, the strong coupling potential grows large enough to generate dozens of new gluons and quark–antiquark pairs that subsequently recombine into stable, colorless hadrons. This non perturbative process called *hadronization* results in a *jet*

of particles in which most of the energy flows along the original parton direction. After the hard interaction, the initial hadrons have lost the color charge associated with the interacting partons. They are no longer stable, colorless objects. The additional hadronic products resulting from the "spectator partons" are collectively called the *underlying event*. When study *jets* its contributions are usually removed. The perturbative component of the hard scattering can be calculated analytically. The contribution of each order is represented by Feynman diagrams. Figure 1.2 shows examples of QCD process of order α_s^2. Leading order perturbative calculations do not include any internal loops. However, at higher orders in α_s, loop integrals become divergent at large momenta. These ultraviolet divergences can be isolated by the regularization procedure [5], and absorbed into the definition of the coupling strength via the renormalization process, introducing a new scale, μ_R.

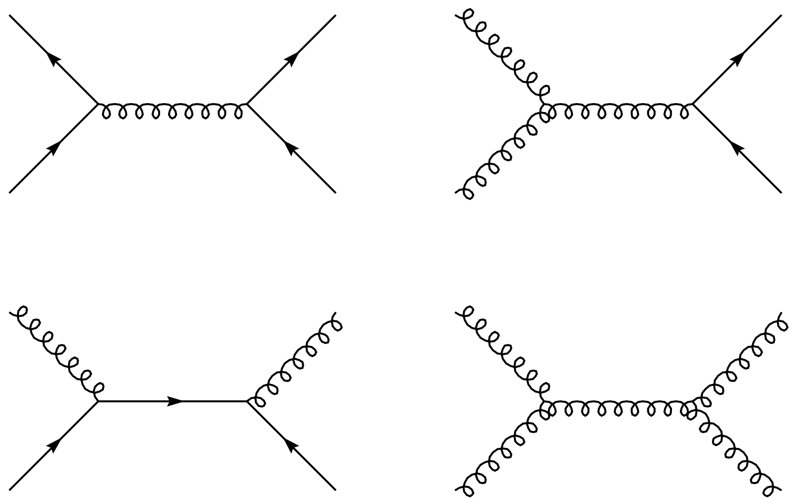

Figure 1.2: Examples of QCD processes of order α_s^2.

Quarks and gluons interact non–perturbately (at low energies) with one another within hadrons. So, the initial momentum of the partons in a hard scattering interaction is not known. However, for a given hadron, the distribution of the momenta of the various constituent partons can be determined. The PDF, parton distribution function, $f_{i/h}(x)$ is defined such that $f_{i/h}(x)\,dx$ gives the number of parton i in hadron h carrying a fraction between x and $x+dx$ of the parent hadron momentum, where x is defined as: $x = p_{parton}/p_{hadron}$. The PDF are independent of the specific interaction and can be experimentally measured.

A cross section involving partons in the initial state is given by the product of the PDF and the partonic cross section, summed over all contributing partons and integrating over all values of x. This procedure, called *factorization* of the perturbative and non–perturbative processes, introduces a scale parameter μ_F, which sets the boundary between the two.

Thus, at the final state of an hadronic collision, QCD predicts the appearance of highly collimated sprays of particles, which are called *jets* and which are the manifestations of the hard–scattered partons. The production of hadronic jets is the dominant process at energies greater than 10 GeV. The Fermilab Tevatron $p\overline{p}$ collider started operations in 1985 at a CM energy of 1.8 TeV. Today, it is the highest CM energy hadron collider offering an excellent opportunity to study jets and their properties. The comparison of experimental measurements and theoretical predictions provides of an enormous source of information about the interaction between partons and the structure of hadrons as well as tests the perturbative QCD predictions for hard scattering. Especially suited for such studies are infrared and colinear safe "jet observables" like event shape, jet rates and jet cross sections.

1.3 Jet Definition

Different algorithms has been developed to define jets. This issue is non-trivial both theoretically and experimentally. The role of these algorithms is to associate clusters of "particles", which can be detector elements or hadrons at the experimental level or partons in a pQCD calculation, into jets such that the kinematic properties of the jets can be related to the corresponding properties of the energetic partons produced in the hard scattering process. Figure 1.3 schematizes the jet production process in a hadron collider. The outgoing partons generate showers of quarks and gluons, which hadronize into particles that interact with the detector leaving energy deposits. Parton jets are defined prior to hadronization while particle jets are defined before particles enter the detector, where jets are conform by the energy deposits. Jet algorithms should yield similar results if applied to any of these steps. Experiments typically correct their measurements from detector to particle level. Theoretical predictions are usually made at parton level. At hadron colliders, the non perturbative hadronization process is regarded as non important, in the sense that it does not modify the jet observables.

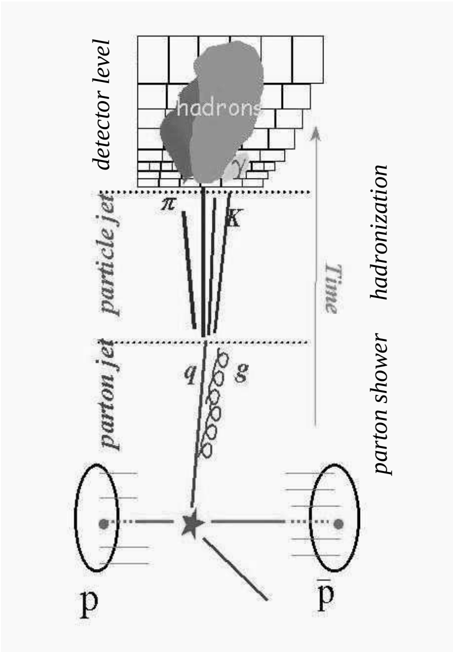

Figure 1.3: Scheme of jet production in a hadron collider.

In general, a jet algorithm must be [6]:

- Fully specified: The jet selection process, the jet kinematic variables and the various corrections should be clearly and completely defined.
- Theoretically well behaved: They should be infrared and collinear safe.
- Lorentz boost invariant: The algorithm should find the same solution independent of boosts in the longitudinal direction.
- Detector Independent: It should not depend on detector type, size,etc.
- Consistent: Equivalence at the theoretical and detector level.

The first three criteria should be satisfied by every algorithm. The last two can probably never be totally true, since it is not possible to completely remove the dependence on the particular apparatus used in the experiment.

1.3.1 Jet Kinematics

In order for the kinematic variables to accurately represent those of the partons, all particles inside the jet must be summed to give global jet quantities, such as energy and momentum. High energy hadron–hadron collisions at symmetric colliders occur in the hadronic CM frame, however, the constituent partons undergoing hard interaction are not usually in their CM frame, as they may carry different fractions of the incoming parent hadron's momentum. The final state emerging from parton–parton scattering is randomly boosted for each event along the direction of the colliding hadrons. In order to optimize the detection and reconstruction of the jets in the final state, it is desirable to use a set of Lorentz z–boost invariant variables for jet kinematics. The usual choice is: jet transverse momentum (p_T), azimuthal angle (ϕ), rapidity (y) and mass (m). The rapidity is defined as:

$$y = \frac{1}{2} \ln \frac{E + p_z}{E - p_z} = \tanh^{-1}\left(\frac{p_z}{E}\right) \tag{1.1}$$

Under a Lorentz boost along the direction of the colliding particles to a frame with velocity β, it transforms as $y \to y - \tanh^{-1}\beta$, yielding a boost–independent distribution dN/dy. The distance between two jets $\Delta R = \sqrt{(\Delta y)^2 + (\Delta\phi)^2}$ is z–boost independent. In the limit of high energies, when the mass of the jet can be neglected with respect to its energy, y is reduced to the pseudorapidity η defined as:

$$\eta = -\ln\left(\tan\frac{\theta}{2}\right) \tag{1.2}$$

which is a purely angular coordinate. In the experiment, the directly measured jet quantities are energy (E), pseudorapidity and azimuth.

1.3.2 The Cone Algorithm

Historically cone algorithms [7] have been preferred for hadron–hadron colliders. The idea is to find cones with base area πR^2 that maximize the energy contained within them. The implementation follows an iterative process which starts from cones centered about the most energetic vectors in the event ("seeds"). It maximizes energy within an area $A = \pi R^2$ in η–ϕ space, where R is the "jet radius". The jet axis, defined as the E_T weighted centroid of the cone, are then used as seeds for new cones. The procedure is iterated until the centroids are stable. This algorithm contains an arbitrary parameter, R, known as the cone size.

The fixed cone jet algorithm has several disadvantages. It allows cones to overlap, so a single vector may belong to two or more cone jets. As a result, a procedure must be included in the cone algorithm to specify how to split or merge overlapping cones. In theoretical calculations an ad hoc parameter, $\mathcal{R}_{\text{sep}}$ [8], chosen to fit the data, is required to simulate the role of seeds and splitting/merging in the experimentally applied algorithm. Even worse, the cone algorithm with seeds is sensitive to soft radiation [9]. For example, consider the case where two partons are located at opposite sides of a single cone (see Figure 1.4). The cone algorithm will reconstruct two jets. However, at NNLO, a soft gluon can be radiated, serving as a seed from which the algorithm will reconstruct a single jet [1]

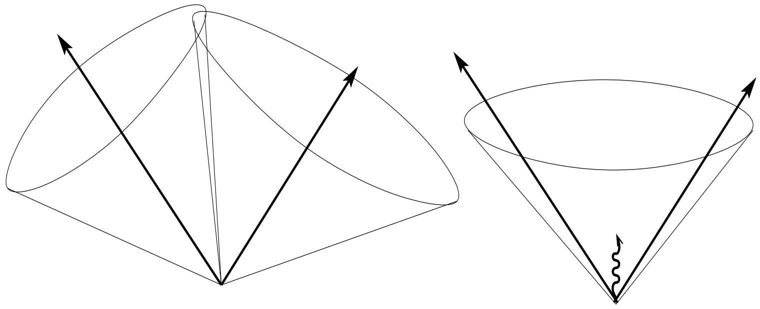

Figure 1.4: An illustration of infrared sensitivity in cone clustering. Jet clustering begins around seed particles. The presence of soft radiation between the two jets may cause the merging of jets that would otherwise not occur.

1.3.3 The $k_\perp$ algorithm

The $k_\perp$ algorithm has been developed inspired in the way partons radiate in QCD. By design, it can be applied in the same way to partons from fixed order or resummed calculations in QCD, partons or particles in a Monte Carlo event generator, or energy deposits (or tracks) in a detector. These different alternatives will be collectively referred to as "vectors". It is also infrared and collinear safe to all orders of calculation.

This algorithm successively merges pairs of vectors in order of increasing relative transverse momentum. This is illustrated in Figure 1.5. $k_\perp$ associates vectors with low $d \approx min(p_{T,A}^2, p_{T,B}^2) \times \Delta R_{AB}^2$, so this parameter is proportional to the softness and the collinearity of the two vectors. It contains a single parameter, which controls when merging stops. All vectors remaining after the clustering process are then called jets. Thus by definition, every vector in the event is assigned uniquely to a

[1] The cone algorithm with "midpoints" solves the infrared safeness problem [6].

$k_\perp$ jet.

There are various variants of the algorithm for hadron colliders [10, 11, 12]. They differ mainly on the method used to merge vectors and the criteria that determine when clustering stops. DØ has chosen the Ellis and Soper algorithm [12] based on its flexibility and because it allows relatively simple comparisons with previous results obtained with the fixed cone algorithm. It chooses as the recombination process, the covariant E scheme, which corresponds to addition of four-momenta. It is the most straightforward, has no energy defect [13] and is better suited to the calibration method described in section 3.1.

The DØ jet algorithm starts with a list of preclusters formed by detector elements (in order to reduce computer processing time, see section 2.4.1.1), or equivalently from partons or particles in a Monte Carlo event generator or pQCD calculation.

Each precluster is assigned a vector:

$$(E, \mathbf{p}) = E_{precluster}(1, \cos\phi\sin\theta, \sin\phi\sin\theta, \cos\theta) \tag{1.3}$$

where θ is the angle with respect to the beam axis, and where we define $p_T^2 = p_x^2 + p_y^2$.

The steps of the algorithm are:

1. For each pair of particles, i and j, we calculate

$$d_{ij} = minimum\left({p_{T,i}}^2, {p_{T,j}}^2\right)\frac{{\Delta R_{ij}}^2}{D^2}\, ;\, {\Delta R_{ij}}^2 = (\eta_i - \eta_j)^2 + (\phi_i - \phi_j)^2 \tag{1.4}$$

   and for each single particle i,

$$d_i = {p_{T,i}}^2. \tag{1.5}$$

2. The minimum d_{min} of all d_i and d_{ij} is found.

3. If d_{min} is a d_{ij}, particles i and j are merged into a new, pseudo-particle k with four vector: ${P_k}^\mu = {P_i}^\mu + {P_j}^\mu$. Then:

$$E_{T,k} = P_{T,k} = \sqrt{P_{x,k}^2 + P_{y,k}^2}\ ,$$

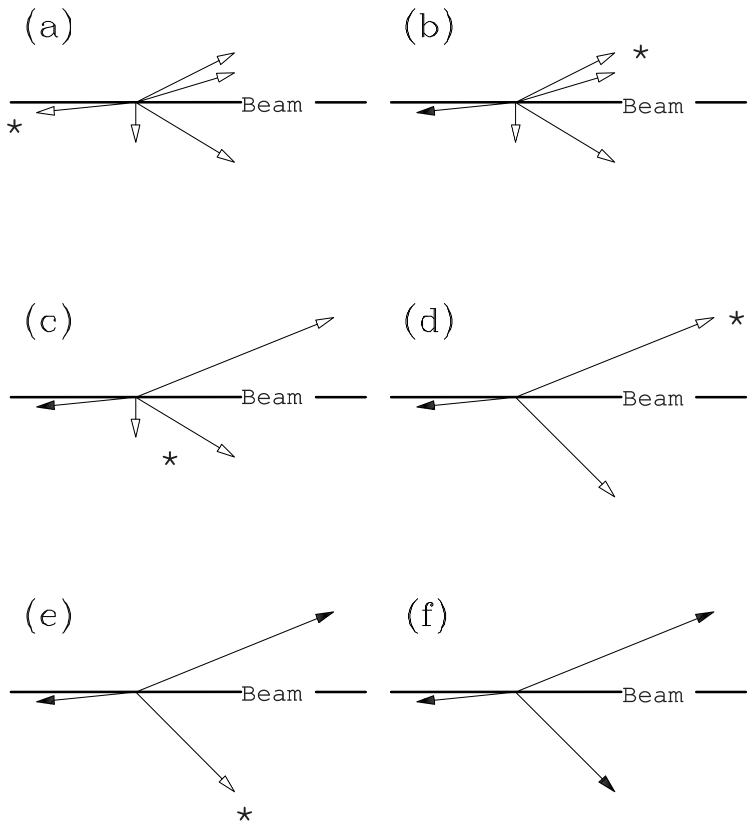

Figure 1.5: A simplified example of the final state of a collision between two beam of hadrons. The open arrows represent vectors in the event, and the solid arrows represent the final jets reconstructed by the $k_{\perp}$ algorithm. The six diagrams show successive iterations of the algorithm. In each diagram, either a jet is defined (when its vector is well separated from all other vectors), or two vectors are merged (when they have small relative transverse momentum). The asterisk labels the relevant vector(s) at each step.

$$\eta_k = -\ln\left(\tan\frac{\theta_k}{2}\right), \qquad \phi_k = \arctan\frac{P_{x,k}}{P_{y,k}},$$
$$\text{and} \quad \theta_k = \arccos\frac{P_{z,k}}{\mid \vec{P_k} \mid}. \tag{1.6}$$

4. If d_{min} is a d_i (i.e. ${R_{ij}}^2 > D^2$ for all j), then the particle is deemed not "mergeable" and it is removed from the list of particles and placed in the list of jets.

5. Loop back to step 1. Repeat steps 1-4 until all particles have been merged into jets (i.e. ${R_{ij}}^2 > D^2$ for all ij pairs).

1.4 Event Shape Variables: Thrust

Event shape variables have been extensively used in $e\bar{e}$ and ep collider experiments to study the spatial distribution of hadronic final states, to test the predictions of perturbative QCD and to extract a precise value of the coupling constant α_s. Over the last few years, they have attracted considerable interest because they have proved to be a fruitful testing ground for recent QCD developments like resummation calculations and non-perturbative corrections.

This thesis presents the first study performed in a hadron collider of an event shape variable, the thrust. This measurement is interesting both experimentally, as it complements previous $e\bar{e}$ and ep data at a higher energy scale (Q) where poorly known non-perturbative effects (of order $1/Q$) are expected to be smaller, and theoretically, because its description solely involves QCD, as opposed to $e\bar{e}$ and ep, where QCD enters as a higher order correction to the lowest order QED interaction.

1.4.1 Thrust in $e\bar{e}$ and ep colliders

There are several variables X that can be chosen to characterize the spatial distribution of the jets produced in a hard collision, the so–called event 'shape', for example whether the distribution of the particles produced is pencil-like, planar, spherical, etc. The distribution $d\sigma/dX$, called differential cross section (rate of events in finite intervals of X), is then measured and compared with the theoretical pQCD prediction. In order to be calculable by perturbation theory, the variable chosen should be infrared safe, *i.e.* insensitive to the emission of soft or collinear gluons. In particular, if p_i is any momentum occurring in its definition, it must be invariant under the branching $p_i \to p_j p_k$ whenever p_j and p_k are parallel or one of them is small. This requires the quantity to be made out of a linear sum of momenta. A widely used variable that meets this requirement is the Thrust, defined as

$$T = max_{\hat{n}} \frac{\sum_i |\vec{p}_i \cdot \hat{n}|}{\sum_i |\vec{p}_i|} \tag{1.7}$$

where the sum is done over all partons, particles or detector elements in the event. The unit vector $\hat{n}$ that maximizes the sum ratio is called the thrust axis.

The values of Thrust range from $T = 0.5$ for a perfectly spherical event, to $T = 1$ for a pencil-like event, when all emitted particles are collinear. In this latter case, the thrust axis lies along the direction of the particles.

The measurements performed in $e\bar{e}$ and ep collider experiments [14] have been found to be in very good agreement, over most of the kinematic range, with the $O(\alpha_s^2)$ perturbative QCD corrections to the lowest order QED diagram that governs the interaction. Fixed order QCD calculations are found to fail however when two widely different energy scales are involved in the event, leading to the appearance of large logarithmic terms at all order in the perturbative expansion [15]. This happens for instance in the limit of the 2-jet back-to-back configuration, when $T \to 1$. This cases are handled by a special pQCD technique, called Resummation, which consists in identifying the explicit large logarithms in each order of perturbation theory and summing their contribution to all orders. Figure 1.6 shows as an example the excellent agreement found in Delphi, once resummation and hadronization corrections are added to the $O(\alpha_s^2)$ QCD prediction [16].

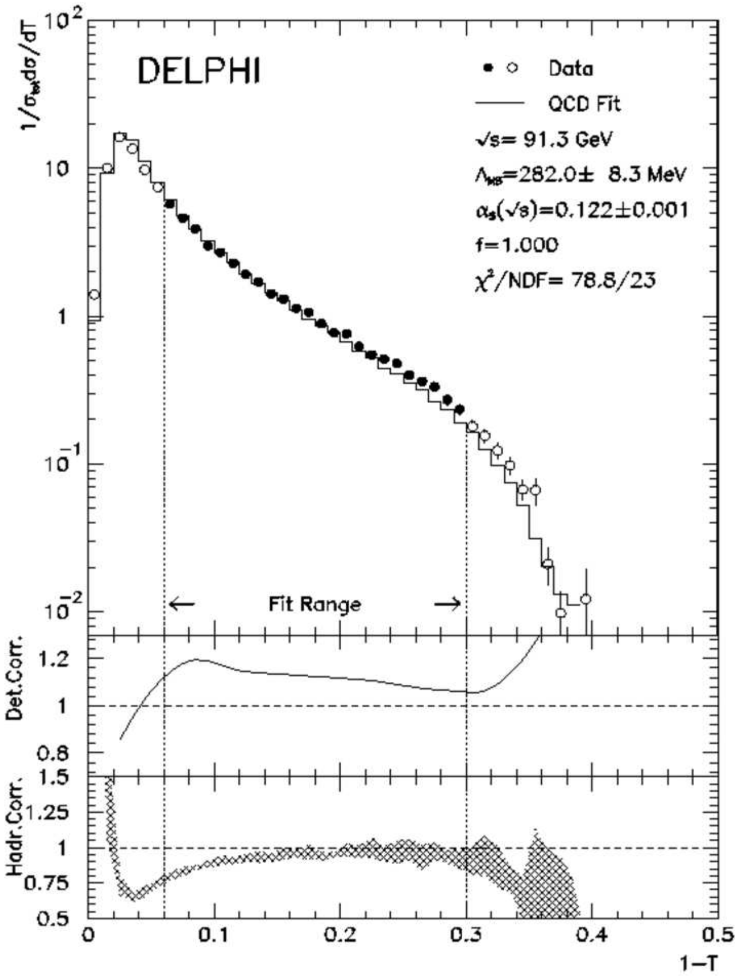

Figure 1.6: Resummed prediction for the thrust distribution in $Z^0 \to$ hadrons, corrected for hadronization, fitted to data of the DELPHI collaboration. The lower curves show the detector and hadronization correction factors.

1.4.2 Thrust in Hadron Colliders

There are two aspects that have to be considered before measuring thrust in hadron collisions, as compared to $e\bar{e}$ and ep: (a) the parton-parton center–of–mass frame is boosted from event to event with respect to the laboratory frame; (b) a fraction of the energy deposited in the detector is not associated with the primary hard interaction, but originates from the physics underlying event (contributions due to soft interactions between spectator partons), additional $p\bar{p}$ interactions, signals from previous crossings (pile–up) and noise.

Since the thrust is not invariant under boosts along the beam direction, the intuitive physical interpretation of the $T \to 0.5$ and $T \to 1$ limits looses its meaning in a $p\bar{p}$ collider. As an example, different events which have two jets back-to-back in the parton-parton c.m system, and that correspond to the same pencil like topology ($T = 1$), will appear in the lab frame with a wide range of values of thrust, depending on the particular momentum fractions of the colliding partons. This problem does not arise in $e\bar{e}$, where the c.m frame is the lab frame, nor in ep, where the electron-parton c.m system is known by measuring the momenta of the incoming and scattered electrons.

In order to avoid these ambiguities, we introduce the "Transverse Thrust", T^t, a Lorentz invariant quantity under z-boosts, which is obtained as in Eq 1.7 but in terms of transverse momenta.

$$T^t = max_{\hat{n}} \frac{\sum_i |\vec{p}_{T_i} \cdot \hat{n}|}{\sum_i |\vec{p}_{T_i}|} \tag{1.8}$$

Transverse thrust ranges from $T^t = 1$ to $T^t = 2/\pi$ ($\langle |\cos\theta| \rangle$) for a back-to-back and a circularly symmetric distribution of particles in the transverse plane, respectively.

A second problem to deal with in hadron colliders, is that thrust cannot be calculated directly from energy deposits in the detector, because only a fraction is associated with the hard interaction itself. Again, this problem does not show up in $e\bar{e}$ colliders, where there is no underlying event and the environment is much cleaner, nor in ep collisions, where a transformation to the Breit frame divides the space into two, a hard interaction and a proton remnant, hemispheres [14].

In order to single out the genuine energy arising from the hard interaction in the noisy environment of a $p\bar{p}$ collider, we have decided to depart from the $e\bar{e}$ and ep approach, that uses the energy deposited in each single detector element, and to calculate instead the thrust from reconstructed jets. The advantage of jet over raw energy deposits is that we are able to work out a correction that eliminates on average the energy contributions from sources other than the hard interaction itself (chapter 3). The jets were reconstructed with the $k_\perp$ algorithm because, as opposed to cone, it is infrared safe and well defined to all orders. This is a major feature for thrust because, as it is discussed below in section 1.5, a calculation to $O(\alpha_s^4)$ corresponds to a LO prediction for low thrust values and a NLO one for the rest of the spectrum.

1.4.3 Dijet Transverse Thrust

We have explained in the previous section that, because of our ignorance of the partonic CM frame and the noisy nature of the $p\bar{p}$ environment, a convenient variable to study in a hadron collider is the *transverse* thrust calculated using *jets* in the event. The Jet Momentum Scale (chapter 3) subtracts the contributions from noise and corrects the energy, on average, back to the particle level. Although it has been derived for jets whose energy is above 5 GeV, low energy jets, in addition to being poorly measured, have a very high probability to originate 100% from background contributions, not related at all to the hard interaction itself. This contamination is not considered in the Jet Momentum Scale, which only corrects for the added energy to genuine jets.

In Chapter 4 it will be illustrated from Monte Carlo studies how these low energy background jets, when included in the calculation of the event thrust, highly distort the shape of the physical distribution. It thus has been decided to ignore all but the two highest energy jets in the event. The inclusion or not of a third jet, required a careful analysis, as they have a large probability of being spurious. A two jet thrust measurement is indeed fully meaningful because the spatial configuration of the two leading jets inherits the information of the rest of the particles produced in the event. For example, in the typical 'Mercedes' topology, shown in Figure 1.7, two equal energy jets at 120° necessarily imply at least a third jet opposite to them, or a number of low energy jets whose momentum is equivalent to such a third jet. Including the third jet could compromise the observable becoming more sensitive to noise effects. However, when calculating the energy scale of the event, it is necessary to take it into account. In the example, not including the third jet would have incurred in a 30% error.

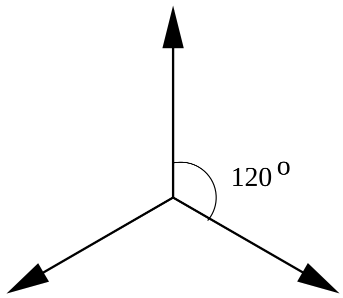

Figure 1.7: Scheme of three jets distributed in a 'Mercedes' topology.

In view of the evidence to be presented, it was decided to use the Dijet Transverse Thrust (only two jets are included in the calculation) as the physics observable to be measured. The additional physics to be gained by including a third jet did not justify the price to be paid on noise dependence. On the other hand, the third jet has been kept when calculating the energy scale of the event, $Q \approx HT3 \equiv E_{T\,1} + E_{T\,2} + E_{T\,3}$. Here the presence of the third jet cannot be inferred from the sum $E_{T\,1} + E_{T\,2}$.

The Dijet Transverse Thrust ranges from $T_2^t = 1$ for a back-to-back topology, to $T_2^t = \sqrt{2}/2$, for two equal energy jets at 90° as it is shown in Figure 1.8. In this case the calculation is reduced to:

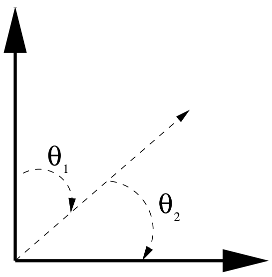

$$\frac{|p_T|}{2|p_T|}\, max(|\cos\theta_1| + |\cos\theta_2|)$$

where for $0 < \theta_1 < 90$ and $\theta_2 = 90 - \theta_1$ is equal to :

$$\frac{1}{2}\, max(|\cos\theta_1| + |\sin\theta_1|) =$$

$$= \frac{1}{2}\left(2\,\frac{\sqrt{2}}{2}\right) = \frac{\sqrt{2}}{2} \quad \text{for } \theta_1 = 45^\circ$$

Figure 1.8: Scheme of two equal energy jets at 90° and the corresponding T_2^t calculation.

1.5 Theoretical Predictions

The cross section in bins of T_2^t in a $p\overline{p}$ collision is calculated as the convolution between the parton distribution functions and the partonic cross section which is obtained by calculating the matrix elements of the contributing processes. It can be written as:

$$\frac{d\sigma}{dT_2^t} = \sum_i \sum_j \int dx_1 \int dx_2\, f_{i/H}(x_1, \mu_F)\, f_{j/\bar{H}}(x_2, \mu_F) \frac{d\sigma_{ij}}{dT_2^t}(x_1, x_2, \mu_R, \mu_F, \alpha_s(\mu_R)) \tag{1.9}$$

where the sum is over all the parton species in the proton and antiproton, $x_{1(2)}$ is the fraction of the proton (antiproton) momentum carried by the scattered partons, $f_{i/H}(x_1, \mu_F)$ represent the parton distribution functions of the proton (antiproton,$\bar{H}$) defined at factorization scale μ_F and $d\sigma_{ij}/dT_2^t$ is the partonic cross section which depends on the coupling constant evaluated at the renormalization scale μ_R. Calculations at fixed order where it is required only two, three or in general a given number of partons at final state, diverge. The infrared divergences cancel when all terms are taken into account.

The partonic cross section and the convolution 1.9 are calculated numerically in programs like JETRAD [17] which is an α_s^3 QCD event generator and NLOJET++ [18], an α_s^4 NLO three jet generator. At DØ, the $k_\perp$ and cone algorithms have been implemented in the JETRAD framework. This program requires the user to set several parameters such as the renormalization and factorization scales, μ_R and μ_F respectively. The scales should be chosen of the same order as the hard scale that characterizes the parton scattering. The larger the number of terms included in the perturbative expansion the smaller the dependence on these scales. Typically, μ_F and μ_R are set to the same value, $p_T^{max}/2$, where p_T^{max} refers to the p_T of the leading jet in an event.

The parton distribution function and the jet clustering algorithm also have to be chosen. In this analysis, jets were reconstructed using the $k_\perp$ algorithm, applied to the final state partons with the same definition than for collider data, no modifications or additional parameters have to be introduced. The CTEQ [19] family of parton distribution functions (PDF) were used for this work.

The NLOJET++ predictions presented here were provided by his author as the code has been recently developed and is not available for us to be run. It is a new NLO event generator for calculating jet observables in hadron–hadron collision (it can also be used for e^+e^- annihilation and in deep inelastic scattering).

JETRAD results, which have at most 3 partons in the final state, provide the LO prediction for T_2^t, except for $T_2^t = 1$ where it is NLO. It includes all terms of third order in α_s but does not include hadronization effects. It is clear from the kinematics that the $O(\alpha_s^3)$ calculation cannot cover the whole physical range of T_2^t. The lowest value of thrust is attained when 2 leading jets are at the largest transverse angular separation, 120°, which corresponds to $T_2^t = \sqrt{3}/2$. This means that in the range $\sqrt{2}/2 \leq T_2^t < \sqrt{3}/2$ the LO perturbative contribution is of order $O(\alpha_s^4)$. It is interesting to remark that this analysis is the only measurement in the DØ experiment that is leading order in α_s^4.

Figure 1.9 shows the JETRAD prediction for one bin of HT3, where the arrow indicates the position of the "cut off" in the theory. Since the thrust adopts values from ~ 0.7 to 1, we chose, following the approach at LEP, to plot the cross sections as a function of $1 - T_2^t$, a variable which ranges between 0 and ~ 0.3.

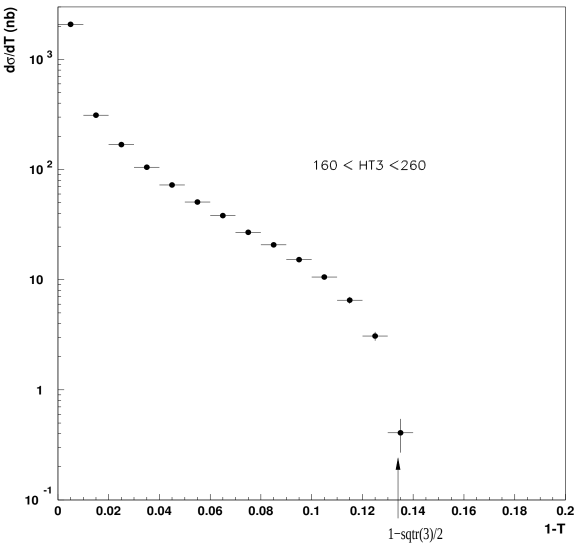

Figure 1.9: JETRAD T_2^t distribution. The *cut off* is indicated with an arrow.

It is not expected to have an agreement neither around (*i.e.,* close to the kinematic threshold) nor below the "cut off" value. JETRAD prediction are also expected to fail in the high thrust range of our measurement. This is due to terms of order $(\alpha_s \ln^2(1-T))^n$, which are large at all orders in the perturbative expansion when $T \to 1$. This is a well known problem in pQCD, that arises whenever two different energy scales are relevant for a process. In our case, a $T \to 1$ event corresponds to two opposite high energy jets, with a third low energy soft jet that slightly imbalances them out from the back-to-back configuration. The calculations of order $O(\alpha_s^3)$ done by JETRAD consists of two parts: two to two parton processes at one–loop (virtual terms) and two to three parton processes (real emission terms) at tree–level. Both contributions are infrared singular. Only the sum of the two is infrared finite and meaningful [20]. Therefore, in order to get a trustworthy prediction it is necessary to consider an observable which is inclusive enough, in our case this means to integrate over a region near $T = 1$, including this point in a suitably large bin.

In order to study the behavior of the theoretical prediction when T_2^t gets close to 1, a logarithm scale is preferred since it excludes the $T_2^t = 1$ point. In this case, the calculations only involve the real emission terms. These processes are infrared singular when two partons become collinear or when a parton becomes very soft. The terms can be split into two parts, "hard emissions" when all partons are well resolved and the "infrared" part. The hard emission parts are computed by means of Monte Carlo integration. By analytically combining unresolved real emissions with the virtual terms, a finite contribution is obtained which can be integrated numerically. The latter will contribute only to the point $T = 1$. The phase space slicing method used by JETRAD to implement the infrared cancellation, employs a resolution criterion s_{min}. It is a cut on the two parton invariant masses:

$$s_{ij} = 2\, E_i\, E_j\, (1 - \cos\theta_{ij}) \tag{1.10}$$

Clusters of partons with invariant mass less than s_{min} are treated as a single parton. The criteria simultaneously regulates both soft ($E_i \to 0$ or $E_j \to 0$) and collinear ($\cos\theta_{ij} \to 1$) emissions. s_{min} is an arbitrary parameter required only for the computer implementation of the calculation, thus, the prediction should be independent of it. In order to choose its value properly, it needs to be taken into account that as s_{min} become smaller, the infrared approximations of the matrix elements becomes more accurate. However, the concern is the numerical convergence of the calculations. As s_{min} is made smaller it becomes harder to engineer the cancellation to the precision to which one would like to compute the cross section. Besides, it can not be so large that it begins to interfere with jet clustering. In the case of T_2^t , Figure 1.10 shows three JETRAD distributions for different s_{min} values. A dependence of the predictions on the parameter can be observed. The selected s_{min} value will depend on how close to $T = 1$ the analysis will go, which is determined by experimental limitations like the finite detector resolutions (this issue is discussed in section 7.3). In our case a value of $s_{min} = 1$ GeV^2 proved to be sufficient.

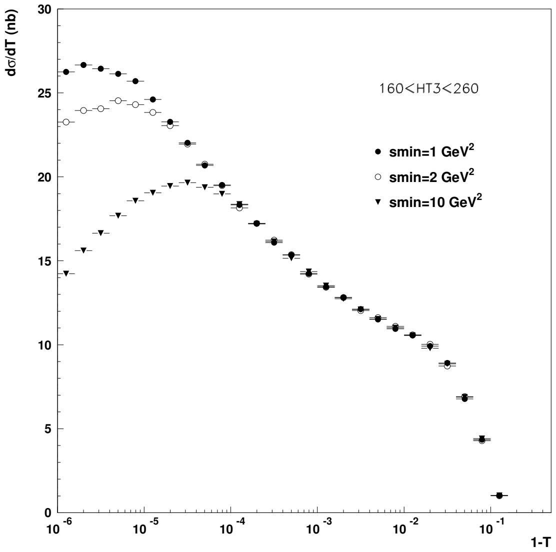

Figure 1.10: JETRAD predictions for different s_{min} values. The full circles correspond to $s_{min} = 1$ GeV^2, the open ones to $s_{min} = 2$ GeV^2 and the full triangles to $s_{min} = 10$ GeV^2.

NLOJET++ is an α_s^4 NLO three jet generator. It comprises one-loop $2 \to 3$ and tree-level $2 \to 4$ processes. The implementation of the two–loop $2 \to 2$ terms is still missing. Thus it is not possible to get a prediction of order $O(\alpha_s^4)$ for the bin which includes $T_2^t = 1$. However, it provides the LO prediction for the range $\sqrt{2}/2 \leq T_2^t < \sqrt{3}/2$ and the NLO correction for $\sqrt{3}/2 \leq T_2^t < 1$, as it is shown in Figure 1.11. Note that the bin including $T_2^t = 1$ is missing for NLOJET++ .

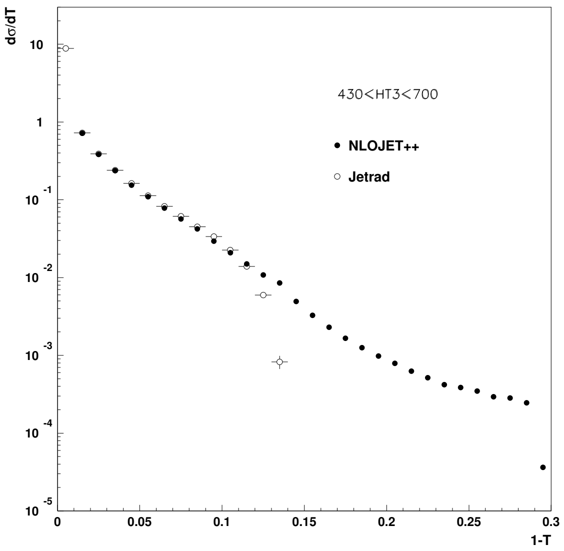

Figure 1.11: Comparison of JETRAD and NLOJET++ predictions.

Since it is a fixed order calculation, it will fail in the limit of the 2-jet back-to-back. However, being a higher order pQCD calculation than JETRAD, it is expected to yield a better agreement with data over a larger T_2^t range. Figure 1.12 shows JETRAD and NLOJET++ T_2^t cross sections in a logarithmic scale, for one HT3 bin. At lower HT3, NLOJET++ predicts smaller values of the cross section than JETRAD. A discussion on this issue is presented in chapter 8.

1.6 Monte Carlo Event Generator

Monte Carlo Event Generators are widely used in high energy experiments. They help to understand the detector behavior providing an excellent tool for jet based analysis. In this work we have used HERWIG [21], a general–purpose particle physics event generator which includes the simulation of hard lepton–lepton, lepton–hadron and hadron–hadron scattering in one package. Soft hadron–hadron collisions are also included and they can be optionally suppressed. It uses the parton–shower approach

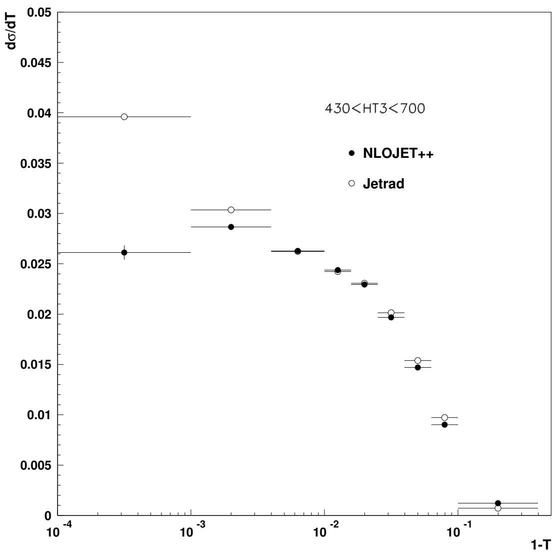

Figure 1.12: Comparison of JETRAD and NLOJET++ predictions at small $1 - T$.

for initial–state and final–state QCD radiation and a model of the hadronization process for the conversion of colored partons into the colorless objects observed in the experiment.

Fixed order perturbative calculations fail to predict details of the jet structure observed in experiments. Event generators use the "parton shower" approach to take into account higher order QCD effects. Following the leading order calculation, parton emissions are performed based on soft and collinear approximations [22], distributing the energy fractions according to the leading order DGLAP splitting functions. The parton showers are terminated when the parton momentum falls below a cut off parameter, Q_0, which is typically set to the order of 1 GeV.

The non perturbative evolution is described by a phenomenological hadronization model which turns the final state partons into hadrons locally in phase space. The hadronization process is independent of the hard process because of the cut off of the parton cascade. HERWIG's "cluster model" for jet hadronization is based on non-perturbative gluon splitting [23]. A similar cluster model is used for soft and underlying hadronic events.

In this analysis, we have generated samples with QCD $2 \to 2$ process. As an example, Figure 1.13 shows the T_2^t distribution at particle level. Jets have been reconstructed with the $k_\perp$ algorithm, applied to the final state particles. The "parton shower" approach takes into account higher order QCD effects allowing comparison with data over the whole T_2^t range.

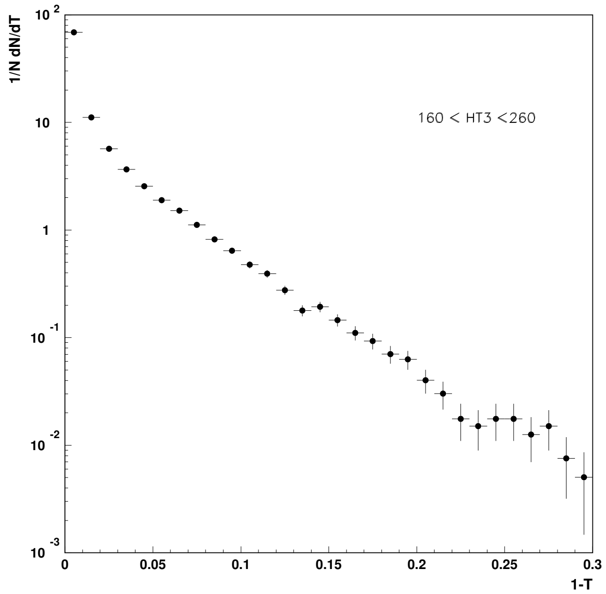

Figure 1.13: Particle level normalized Dijet Transverse Thrust distribution obtained from a HERWIG MC sample.

Although MC event generators do not fully reproduce the global characteristics of jet events, like for instance its p_T spectrum, they are an essential tool to simulate realistic collider events. In this thesis will use it to study the distortion introduced in the thrust distribution by background and detector effects, and the correction to jet energies and positions due to noise and other detector features.

Chapter 2

The Experiment

The basic steps in the acceleration process at Fermilab and a brief review of the DØ detector are presented in this chapter. A more detailed discussion on the Fermilab accelerator complex can be found in [24]. The description of the DØ detector is based on [25] [1].

2.1 The Fermilab Tevatron

The Tevatron, located at the Enrico Fermi National Laboratory (Fermilab, USA), is currently the world's highest center-of-mass (CM) energy proton–antiproton colliding beam accelerator. The Fermilab accelerator complex employs several accelerators and storage rings to produce $p\overline{p}$ collisions with an energy of 1.8 TeV in the center of mass. The Tevatron itself is the last accelerator in the chain which started operations in the mid 1980s. Figure 2.1 shows an scheme of the Fermilab complex.

From the preaccelerator, a 750 GeV beam of negative hydrogen ions emerges (accelerated by a Cockroft-Walton electrostatic accelerator) and enters into the Linac.

[1] The detector and the accelerator have undergone an upgrade process which finish on the year 2002. The descriptions presented here correspond to the period during which the data for this analysis was taken.

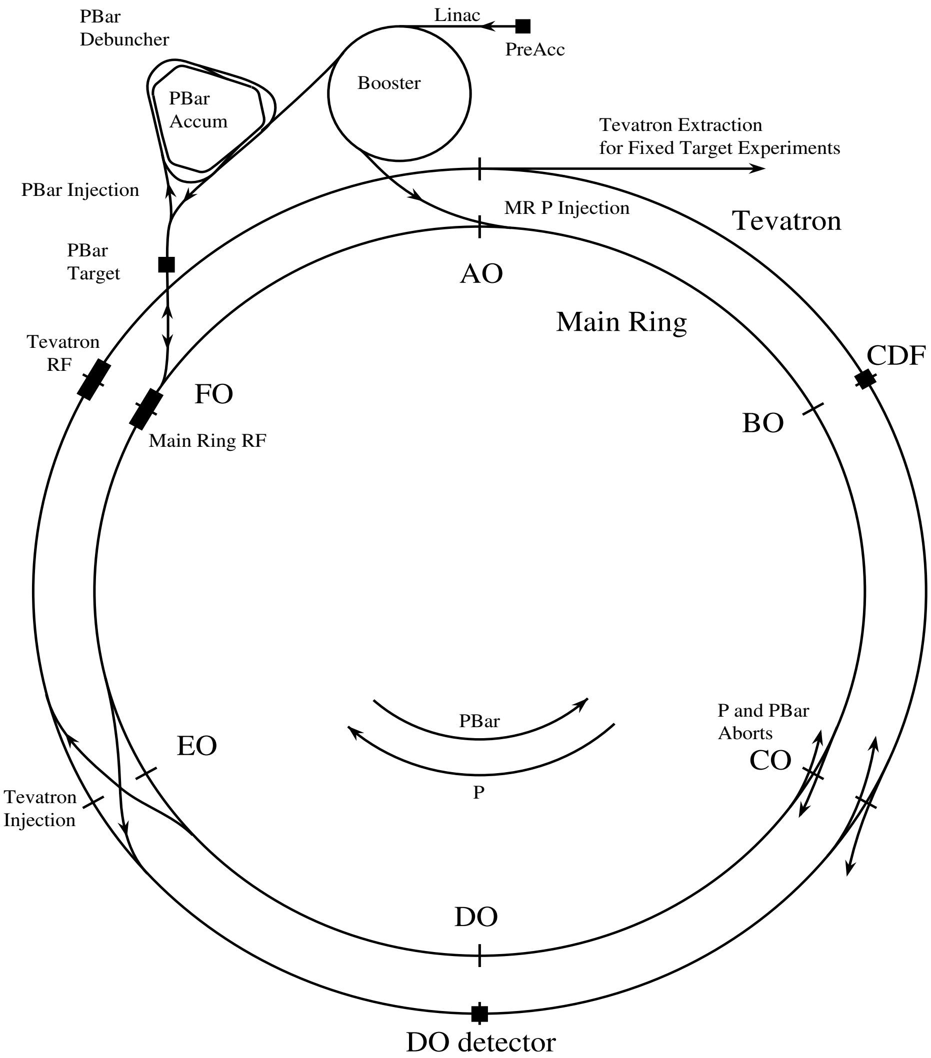

Figure 2.1: Schematic view of the Fermilab accelerator complex. Although the Tevatron and the Main Ring have the same radius, they are shown separated for clarity.

The Linac is a linear accelerator, aproximately 150 m long, from which H^- ions emerge with an energy of 400 MeV. The ions are then striped of the electrons by a carbon foil, leaving only the proton cores which are injected into the Booster, a synchrotron, where they are accelerated to 8 GeV. The next step is the Main Ring (MR). It is a synchrotron of 2 km of diameter which consists of 1000 magnets that bend and focus the protons. They can be accelerated to either 120 or 150 GeV depending on their destination.

The antiproton beam creation starts with a bunch of protons, extracted from the MR at 120 GeV, which is directed onto a tungsten target producing antiprotons with wide momentum spread. This spread is reduced in a small synchrotron, the Debuncher. They are finally sent to a storage ring, the Accumulator, where they stay until there are enough of them to be transferred to the Main Ring.

The final stage of the process occurs in the Tevatron. It receives six bunches of 150 GeV protons and antiprotons from the MR and accelerates them to 900 GeV to provide a CM energy of 1.8 TeV. This third synchrotron consists of 1000 superconducting magnets which guide the beams. The p and $\overline{p}$ bunches, which circulate in opposite directions, can collide in two interactions points, BØ (CDF) and DØ, every 3.5μs.

2.2 The DØ Detector

The DØ detector is a multipurpose apparatus designed to study proton-antiproton collisions with an energy of 2 TeV in the center of mass. It was built to cover a wide spectrum of physics topics by providing accurate measurements to test the Standard Model predictions and search for new phenomena. The strength of the detector resides in its excellent calorimetry. It has been designed to accomplish good measurement of high p_T jets through finely segmented, hermetic, linear and nearly compensating calorimeters, precise determination of the missing transverse energy in the calorimeters as a way of detecting neutrinos and possible other non-interacting particles, and an accurate identification and measurement of electrons and muons. Fully assembled, the detector stands 13 m in height, 11 m in width, and 17 m in length, with a total weight of about 5500 tons. The first data taking period, or *Run*, with the DØ detector started in 1992 and continued through 1995 (Run I). A general view of the Run I DØ detector is shown in Figure 2.2. A right handed coordinate system is adopted in which the z-axis is along the proton direction and the y-axis is upward. The angles ϕ and θ are the azimuthal and polar angles, respectively. The radial coordinate r is the distance from the beam line.

In the following sections, the different components of the detector are described, based on [25]. The description of the calorimeters is more detailed since they constitute the principal tool for jet measurements.

2.2.1 The Central Detector

The Central Detector is a system of concentric tracking and transition radiation chambers. It is illustrated in Figure 2.3. It is located between the Tevatron beam line and the inner cylindrical aperture of the calorimeters. It extends 270 cm along the z-axis, centered at $z = 0$ and it has a radius of 78 cm. Its main purpose is to reconstruct the three-dimensional trajectories of charged particles which pass through them. The tracking detectors are wire drift chambers. The innermost chamber, which surrounds the beam pipe, is the Vertex Chamber (VTX). It reconstructs tracks around the interaction point and measure the vertex position in the plane perpendicular to the beam direction with a typical resolution of 50μm. The next detector is the Transition Radiation Detector which distinguish between electrons and pions. The Central Drift Chamber is the outermost tracking detector. It provides coverage for tracks at large angles while the Forward Chambers, which cap the other central detectors, provides coverage down to 5^o.

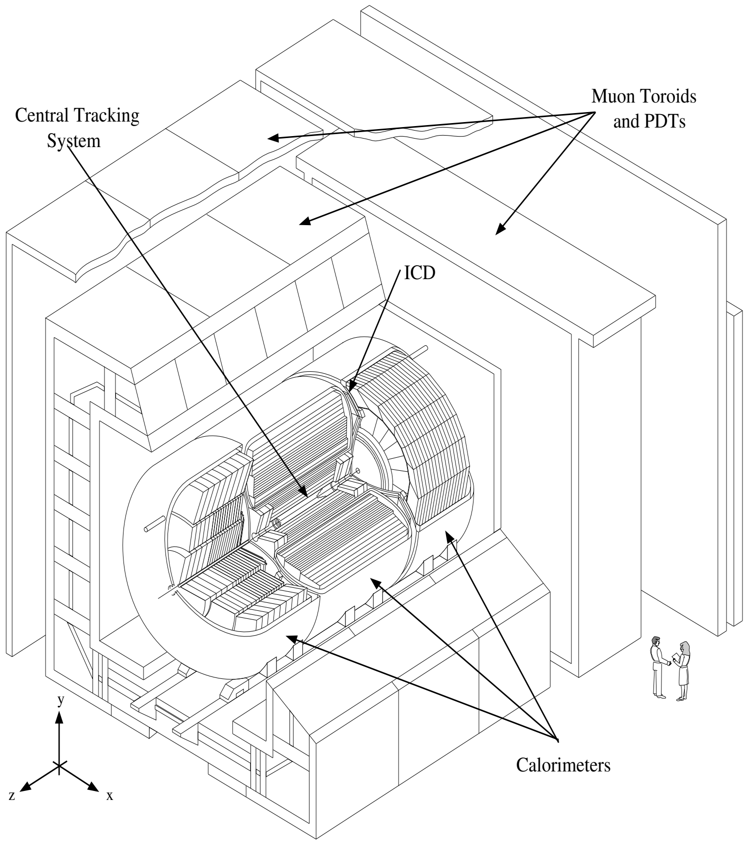

Figure 2.2: A general view of the Run I DØ detector

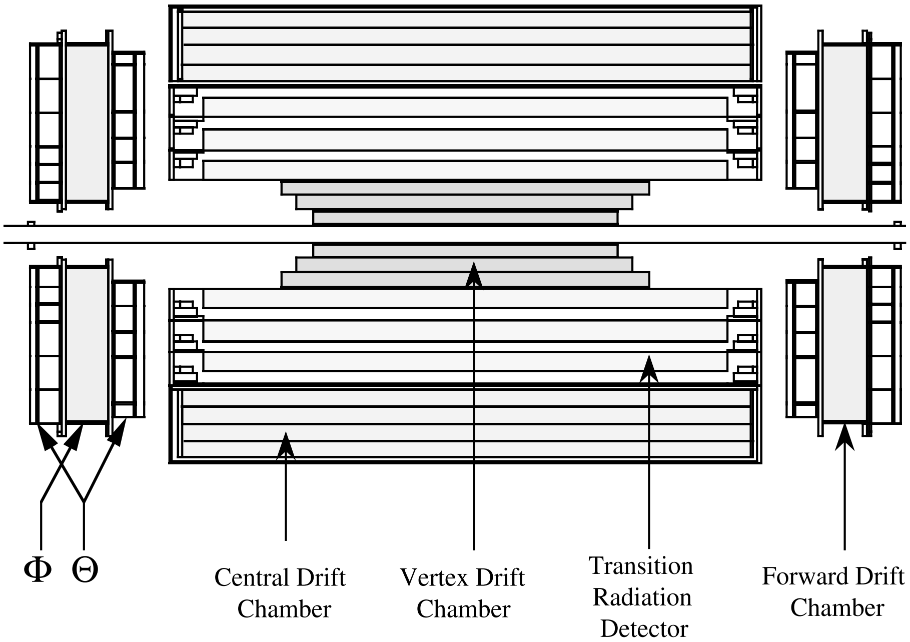

Figure 2.3: The Central Detectors.

2.2.2 The Calorimeters

The DØ calorimeters are the most important tool for jet detection. They provide energy measurement for electrons, photons and jets. Other roles of the calorimeters are particle identification and the determination of the Missing Transverse Energy ($\not{E}_T$).

As energetic particles enter and transverse the calorimeters they initiate cascades of particles, electromagnetic or hadronic showers, caused by interactions along the path of the primary ones. The characteristics of the incoming particle are reconstructed based on the precise identification and measurement of the induced shower in the material. Calorimeters can be used to measure not only the energy but also the spatial position, direction and, in some cases, the nature of the primary particle.

The DØ calorimeters correspond to a sampling design using liquid argon (LAr) as the active medium. A general view is shown in Figure 2.4. In order to have access to the Central Detectors, they are housed in three separated double-walled stainless steel cryostats, one central and two end-caps, the latter two being mirror images of each other. Excellent containment and hermicity are achieved with the Central Calorimeters (CC) providing coverage for roughly $|\eta| < 1.0$, and the two End Calorimeters (EC) up to $|\eta| \sim 4$. The number of nuclear absorption lengths, λ, is typically 7 for the CC and 9 for the EC.

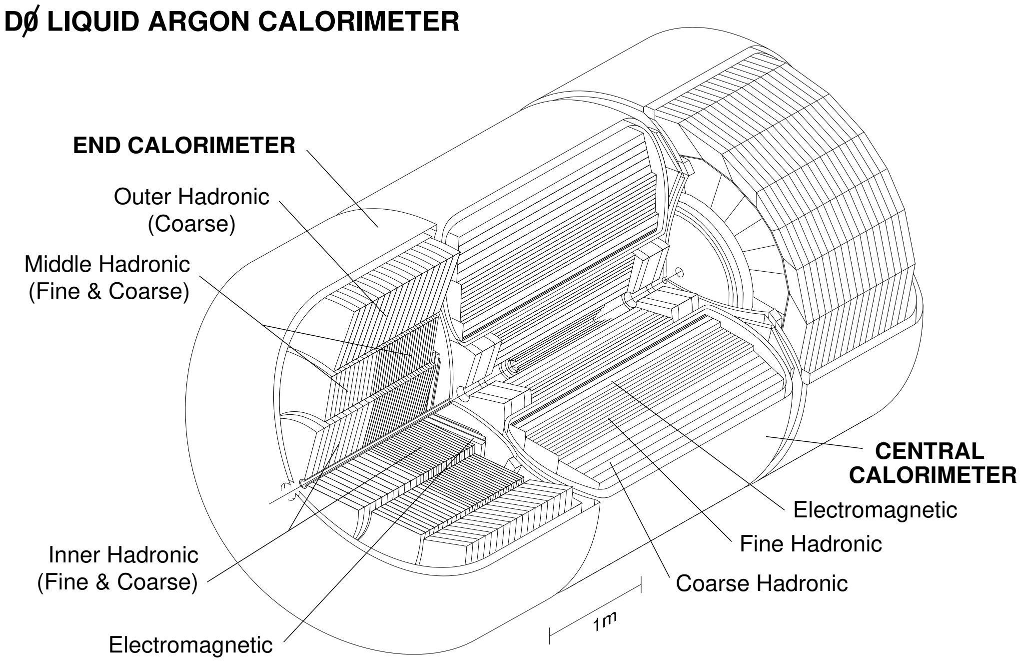

Figure 2.4: General view of the DØ calorimeters.

The basic detector unit of these sampling calorimeters is the calorimeter cell. An schematic view is shown in Figure 2.5. It consists of a grounded metal absorber plate and a signal board (anode). These two elements are separated by a gap filled with liquid argon as the active material. The particles, as they enter the calorimeter, interact with the array of absorber plates producing a shower of particles and losing most of their energy. A small fraction is deposited in the gaps as the particles ionize argon atoms. To collect liberated electrons, an electric field is applied across the gap (the signal board is kept at +2 kV potential). The charges drift towards the anode, inducing an electric signal which can be detected and read out. The signal is calibrated to the incoming particle energy.

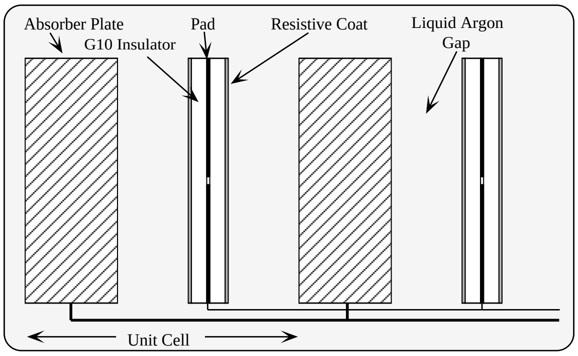

Figure 2.5: Schematic view of a calorimeter cell.

One distinct characteristic of the DØ calorimeter is its pseudo-projective geometry. Straight lines can be drawn from the interaction point through the centers of an array of cells forming a tower. Typical transverse sizes of towers are $\Delta\eta \times \Delta\phi = 0.1 \times 0.1$ radians, providing excellent shower position resolution (the typical jet size is $\sqrt{(\Delta\phi)^2 + (\Delta\eta)^2} = 0.5$). The pseudo-projective nature of the calorimeter towers is illustrated in Figure 2.6. The entire calorimeter is segmented into ~ 6000 towers.

The central calorimeters actually consist of three concentric cylindrical modules: an electromagnetic (EM) section of modules which are thick enough to contain most electromagnetic showers, a fine (FH) and a coarse hadronic (CH) section (see Figure 2.4). The EM consists of four longitudinal read out layers which have 2,2,7 and 10 radiation lengths, X_0, in depth. The segmentation of the third layer is $\Delta\eta \times \Delta\phi = 0.05 \times 0.05$ to provide better transverse measurement at electron shower maximum. The FH has three longitudinal layers with a total width of 3.2λ while the CH consist of one read out layer with the same total depth.

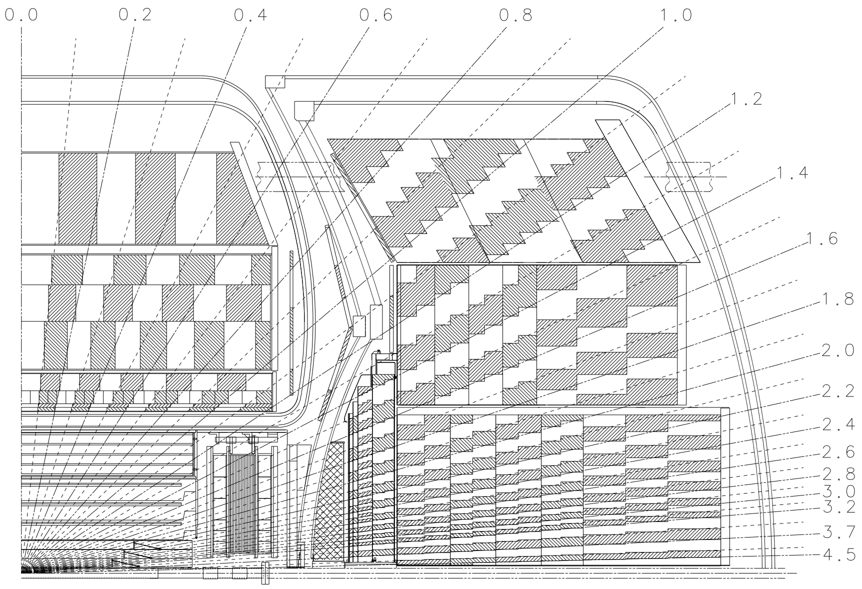

Figure 2.6: Side view of calorimeter towers.

The end calorimeters are similar to the CC. The electromagnetic module (ECEM) is divided into four read out sections with a total length of $\sim 20X_0$. There is one Inner Hadronic module (ECIH) with four read out sections each about 1.1λ thick and one coarse hadronic segment of 4.1λ in depth. Outside the ECEM and ECIH there are concentric rings of 16 Middle (ECMH) and Outer (ECOH) modules. Each ECMH module has four FH read out sections of about 0.9λ deep and one 4.4λ thick CH section. The ECOH modules have three CH readout layers and a total longitudinal depth of about 4.4λ.

2.2.3 Masless Gaps and InterCryostat Detectors

The region defined by $0.8 < |\eta| < 1.4$ is instrumented with the Masless Gaps and the InterCryostat Detectors. The ICD's are a set of scintillation counters mounted on the front surface of the EC cryostats. The MG are located inside the CC and EC cryostats. They are copper readout boards identical to single-cell structures. They provide additional sampling of the showers leaving the CC and entering the EC cryostat.

2.2.4 Calorimeter Readout

The signal induced on the readout pads are pulses with widths of ~ 500 ns. The collected electrons are integrated to produce a signal which peaks $\sim 2\mu$s after a $p\overline{p}$ bunch crossing with a decay time of $\sim 30\mu$s. Each cell is sampled twice, one at the time of the bunch crossing (base) and again 2μs later (peak). The raw energy in the cell is defined as the difference between the two voltages. The actual reading for the base sample depends on previous bunch crossings since the signal decay time is much longer than the accelerator bunch spacing (3.5μs). This luminosity dependent effect is called pile–up and leads to an average negative contribution to the measured cell's energy. Also multiple $p\overline{p}$ interactions within the same accelerator bunch crossing (luminosity dependent) contribute to the energy offset.

The average energy of individual cells is not zero even in the absence of an external particle flux. This is due to Uranium decay and electronic noise. For each cell, a distribution of this pedestal energy was measured. The mean pedestal energy was calculated and subtracted online. In order to save processing time, cells containing energy within two σ of the mean pedestal energy were not read out or recorded (*zero–suppression*). Since, electronic pulse shaping made the distribution asymmetric, the zero–suppression contributes with a positive offset to the raw energies.

2.2.5 Calorimeter Performance

Among important characteristics of the calorimeter performance, the ones often quoted are their response linearity as a function of incoming energy and their energy resolution. Test beam studies show that the energy response to both electrons (above 10 GeV) and pions (above 20 GeV) is linear to within 0.5%. The e/π response ratio falls from about 1.11 at 10 GeV to 1.04 at 150 GeV.

The sampling calorimeter fractional energy resolution σ_E/E is expected to improve as $1/\sqrt{E}$ because it is dominated by the statistical fluctuations in the number of sampled charged tracks, which is directly proportional to the incoming energy. Contributions from the noise become increasingly important at low energies. The dead material and calibration errors contribute with a constant term. Thus, the fractional energy resolution is parametrized as the sum in quadrature of these three terms:

$$\left(\frac{\sigma_E}{E}\right)^2 = \frac{N^2}{E^2} + \frac{S^2}{E} + C^2 \tag{2.1}$$

where N represents contribution from noise, S is the sampling term and C the constant offset term. Test beam studies show that the calorimeter energy resolution is approximately $15\%/\sqrt{E}$ for electrons and $50\%/\sqrt{E}$ for pions. The calorimeter energy resolution for jets is measured from collider data. It will be discussed in

Chapter 6.

2.2.6 The Muon System

The Muon system is placed right outside the calorimeters and consist of a set of saturated iron magnets and proportional drift tube (PDT) chambers. It is used to identify muons emerging from $p\overline{p}$ interactions and to determine their momenta and trajectories. There are two main sets of chambers: the Wide Angle Muon Chamber (WAMUS) which provides coverage at large angles and the Small Angle Muon Chambers (SAMUS) for small angles. They consist of three layers of individual chambers: the A layer before the iron toroids and the B and C layers after the magnets. The magnetic field of 2 Tesla bends the muons in the $r - z$ plane. The muon direction is measure before and after the magnets and the momenta is obtained from the bending angle. The muon system may be used in jet analyses to detect cosmic shower contamination and leakage outside the calorimeters.

2.3 Trigger and Data Acquisition Systems

The event readout rate at the DØ detector is about 300 kHz. Since, it is not possible to log and handle each interaction, a selection process is implemented to keep only those events of physics interest. This system is known as the "trigger". There three trigger levels involving hardware and software decisions, which are able to reduce the event rate to 2 Hz, rate at which events can be written to tape. The following is a description of the different trigger levels with an emphasis on calorimeter triggering.

2.3.1 The Level Ø Trigger

It is the first hardware trigger stage. Its main purpose is the detection of an inelastic $p\overline{p}$ collision. It also provides a measurement of the z position of the interaction vertex and of the instantaneous luminosity. It reduces the event rate from 300 kHz to ~ 20 kHz.

It consists of two scintillating hodoscopes, located on the inside faces of the end cap cryostats, perpendicular to the beam, which provide coverage for $1.9 < |\eta| < 4.3$. Coincidence between the signals from the two scintillator arrays indicates the presence of inelastic collisions with nearly 100% efficiency. By comparing the arrival times of the signals from the two arrays, the approximate z–position of the interaction vertex is obtained (with a 3.5 cm resolution).

2.3.2 The Level 1 Trigger

The aim of the Level 1 Trigger is to filter out uninteresting events within a very short time of the beam crossing reducing the rate from 20 kHz to 200 Hz. It accepts information from the Level Ø , the calorimeter and the muon systems. It reads up to 256 input trigger variables which are combined into 32 outputs (trigger bits). In the case of the calorimeters, these triggers compare the sum up of analog signals in the trigger towers, regions defined by a 0.2×0.2 solid angle in η-ϕ space with thresholds set by the user. The sums are done over all the electromagnetic and fine hadronic layers in the range $|\eta| < 4$. It thus identifies electron/photon and jet candidates. Using the Level Ø fast z vertex information the missing transverse energy of the event is calculated. Based on this information, the Level 1 Trigger checks if the event satisfies one or more of the 32 available trigger requirements. If it does, the event is passed on to the next trigger level, otherwise is discarded.

Some of the trigger bits are passed too often and saturate the next trigger level. In order to reduce the amount of data these trigger bits are *prescaled*, meaning that only one out of a fixed number of passed events will actually pass the Level 1 trigger.

2.3.3 The Level 2 Trigger

The Level 2 Trigger is a farm of a large number of VAX workstations working in parallel. The event candidates are further reconstructed using the information from the entire DØ detector, focusing on the areas identified in the Level 1. Simplified algorithms are used to reconstruct the Level 2 physics objects, like electrons, muons and jets. There are 128 software filters connected to the 32 trigger bits of the Level 1 which can also be prescaled. The Level 2 Trigger reduces the event rate to about 2 Hz.

2.3.4 The Jet Triggers

In this analysis the inclusive Jet Triggers were used. They exist in the Level 1 and Level 2. In the hardware level, jet triggers required a certain number of triggers towers or large trigger *tiles* (0.8×1.6 in η-ϕ space) to have transverse energy (E_T) above a desired threshold value. If Level 1 accepts an event, it passes the information onto Level 2. In the software filter level, the fast jet finding algorithm starts from the Level 1 "seed" tower list drawing a box of 1.4×1.4 in η-ϕ around each seed centroid. The E_T weighted centroid of this box is taken as the Level 2 jet center. All trigger towers not included into other Level 2 jets are summed up within a fixed cone radius of 0.7 in η-ϕ around the Level 2 jet centroid. If at least one jet passes a preset threshold for the designated jet filter, the corresponding trigger bit is set on and the event is accepted. Table 2.1 summarizes the Level 1 and Level 2 requirements for all the jet triggers used in this analysis.

2.4 Offline Reconstruction

DØ data go through a complicated computing process before they are ready to be analyzed in the production of physics results. At the *raw* level the data consist of dig-

Trigger Name	Run Number	Level 1 (GeV) - 1 tile with -	Level 2 (GeV) - 1 L2 jet with -
Jet_Min	all	$E_T > 3$	$E_T > 20$
Jet_30	all	$E_T > 15$	$E_T > 30$
	≤ 77824	$E_T > 35$	
Jet_50	$77825 \leq \text{run} \leq 85226$	$E_T > 25$	$E_T > 50$
	≥ 85227	$E_T > 15$	
Jet_85	$77824 \leq$	$E_T > 60$	$E_T > 85$
	≥ 85227	$E_T > 35$	
	≤ 77824	$E_T > 60$	
Jet_Max	$77825 \leq \text{run} \leq 85226$	$E_T > 35$	$E_T > 115$
	≥ 85227	$E_T > 45$	

Table 2.1: Level 1 and Level 2 inclusive trigger configurations.

itized detector electronic signals. The DØ reconstruction program (**DØRECO** [26]) turns raw data into hits, tracks and energy deposits. In a second step, **DØRECO** uses a set of algorithms to identify physics signatures, like electrons, photons, muons, jets and $\not{E}_T$. The fundamental physics quantities associated with them are also calculated and stored.

2.4.1 Jet Reconstruction Algorithms

The algorithms used at DØ to reconstruct jets were described in section 1.3.3 and 1.3.2. Since, the detector consists on $\sim$ 6000 calorimeter towers, a method has to be applied to reduce the number of inputs of the algorithms and in this way to limit the computer processing time.

2.4.1.1 Preclustering

The $k_\perp$ jet algorithm is an $O(n^3)$ algorithm [11], where n is the number of vectors in the event. Limiting computer processing time does not allow this algorithm to run on the ~ 6000 towers of the DØ calorimeters. Thus, a preclustering procedure is used [27] to reduce the number of inputs to the algorithm. Essentially, towers are merged if they are close together in η–ϕ space or if they have small (or negative) p_T. An identical algorithm is also applied to particles in a Monte Carlo generator, in order to perform consistent comparisons between the data and the simulated events. The procedure removes cells with $p_T < -500$ MeV. Cells with a small negative energy are allowed due to pile–up effects in the calorimeter. Starting at $\eta = -9$ and $\phi = 0$, closest towers are combined into preclusters, such that no two preclusters are within $\Delta R = \sqrt{\Delta\eta^2 + \Delta\phi^2} = 0.2$, following the Snowmass prescription:

$$E_T = E_{T,i} + E_{T,j}$$

$$\eta = \frac{E_{T,i}\ \eta_i + E_{T,j}\ \eta_j}{E_{T,i} + E_{T,j}}$$

$$\phi = \frac{E_{T,i}\ \phi_i + E_{T,j}\ \phi_j}{E_{T,i} + E_{T,j}}$$

The procedure continues in the ϕ direction and it is iterated over increasing η. Preclusters with $E_T < 200$ MeV are redistributed to neighboring preclusters in order to produce ~ 200 of them per event (to fit processing time constraints).

In the case of the cone algorithm, calorimeter towers are first sorted in E_T. Starting with the highest E_T tower, preclusters are formed from contiguous towers within a radius of 0.3 in η–ϕ space until all towers with $E_T > 1$ GeV have been assigned to a seed cluster.

2.4.1.2 $k_\perp$ Jet Sample

The implementation of the $k_\perp$ algorithm for offline event reconstruction was done as part of the DØfix software package. This package was not used for previous analysis which applied the fixed cone algorithms. It contains modifications from the standard reconstruction program, **DØRECO**. The DØfix code provides data samples for the $k_\perp$ and the cone algorithms in a simultaneous way. The parameters used were $D = 1$ for $k_\perp$ and $R = 0.7$ for cone.

2.4.2 Determination of the Interaction Vertex

A precise determination of the interaction vertex is essential to obtain the E_T and η of the jets. Its position in the $x - y$ plane is determined from tracks reconstructed by the VTX with a resolution of 50μm . The z-vertex resolution varies within the range $0.65 - 0.95$ cm depending on the number of tracks in the event and their angular distribution. In events with more than two reconstructed vertices, the vertex finding algorithm determines the interaction point from the candidate with more tracks [28].

2.4.3 Determination of the Event Missing Transverse Energy

The event missing transverse energy is defined as:

$$\vec{\not{E}}_T = \left(\not{E}_x \ ; \ \not{E}_y \right) = \left(-\sum_i^{cells} E_{x,i} \ ; -\sum_i^{cells} E_{y,i} \right) \tag{2.2}$$

where the sum is over all calorimeter cells including the ICD and massless gaps. In an ideal calorimeter, a non-zero $\not{E}_T$ indicates that there is a neutrino and/or a muon in the event. Neutrinos do not interact within the DØ calorimeters and high $p_T$muons only deposit a small portion of their energy. In a real calorimeter, the $\not{E}_T$ also includes the effect of the noise and the energy and position resolutions. In QCD events small values of $\not{E}_T$ are expected.

2.4.4 Detector Simulation

Monte Carlo Event Generators and Detector Simulation programs are widely used at DØ to help understand the detector behavior under known conditions. The Event Generator used on this analysis is HERWIG [21](see section 1.6). The DØ Monte Carlo simulation program is based on the GEANT [29] package developed at CERN. This tool allows to track particles through an experimental setup for simulation of detector response. The full Monte Carlo simulation of hadronic showers, while desirable for realistic evaluation of detector performance, is very time consuming of computer resources. The SHOWERLIB method [30] consists of using the full detector (full description of the geometry and composition of the entire DØ detector) and shower simulation only once to make a library of single particle shower. In subsequent simulations, a particle produced in the Monte Carlo is replaced by a shower recorded in the library based on its energy and position in the calorimeter.

Chapter 3

The Jet Momentum Scale

As it was discussed in detail in Chapter 1, this analysis is based on the $k_\perp$ algorithm for jet reconstruction. This choice is founded on its good theoretical properties, because it is infrared safe at all orders in pQCD and it can be consistently applied in an identical way at all levels, be it theoretical partons, physical particles or experimental calorimeter towers. These two properties are not shared by the cone algorithm, which has nevertheless been chosen in the past in hadron colliders due to its relatively simpler energy calibration. The $k_\perp$ jets calibration is in effect more involved in the busy environment of $p\overline{p}$ collisions, where a substantial fraction of the energy deposited in the detectors is not associated with the hard interaction, because, unlike the cone case, they do not have a well predetermined size and shape. A major part of this thesis has thus been devoted to study this problem and to design a new procedure that could be applied to $k_\perp$ jets. This section presents these studies, the method we have developed and the obtained results.

3.1 Jet Momentum Calibration

The jet momentum measured by the calorimeters is distorted by experimental effects and the physics underlying event (the contributions due to soft interactions between partons which do not participate in the hard scattering). The correction that *on average* restores the momentum back to the final state particle level jet momentum (*before* the interaction with the calorimeter) is referred to as the Jet Momentum Scale. Hadronization effects are not taken into account as there is no intention to correct the measured jet momentum to the parton level.

Given the measured jet momentum (p_{jet}^{meas}), the corresponding particle level momentum (p_{jet}^{ptcl}) is obtained through:

$$p_{jet}^{ptcl} = \frac{p_{jet}^{meas} - p_o(\eta^{jet}, p_T^{jet}, \mathcal{L})}{R_{jet}(\eta^{jet}, p_T^{jet})} \tag{3.1}$$

where $\mathcal{L}$ corresponds to the instantaneous luminosity and η^{jet} and p_T^{jet} to the jet pseudo-rapidity and transverse momentum, respectively. The offset, p_o, removes the additive contributions due to the underlying event and noise, and R_{jet}, takes into account the calorimeter response to jets. In what follows, each component is discussed in detail.

3.1.1 The Offset Correction

A hard interaction is defined as a high Q^2 elastic parton–parton scattering, while a hard $p\overline{p}$ interaction includes also the soft interactions between the spectator partons. The offset corresponds to the additive contributions to the measured energy which are not associated to the hard interaction itself. It is divided in two parts:

$$p_o = O_{ue} + O_{zb} \tag{3.2}$$

where O_{ue} is the offset due to the physics underlying event (energy associated with the spectator partons) and O_{zb} is the offset due to the experimental environment which consists in uranium noise, pile–up and additional $p\overline{p}$ interactions in the same crossing.

At DØ, a crossing triggered as a high p_T event can be modelled as the sum of a hard $p\overline{p}$ interaction and a Zero Bias event (ZB) at the same luminosity. Zero Bias data consists just in random $p\overline{p}$ bunch crossings and corresponds to the contributions of uranium noise, pile–up and additional $p\overline{p}$ interactions. In the case of the cone algorithm, where jets have a fixed area, the offset correction O_{zb} is obtained by measuring the energy density (D) in ZB events. The energy which has to be subtracted from the jet, can then be calculated as $D \times A$, where A is the area of the jet in η–ϕ space ($A = \pi R^2$). Since $k_\perp$ jets have no fixed shape, the determination of the offset correction cannot be pursued in this way. We have developed a new method [32], based on the techniques used to derive the fixed cone jet energy scale [31]. The calibration described in this section corresponds to the $k_\perp$ jet algorithm detailed in section 1.3.3 with $D = 1$. A description of the procedure used for the cone algorithm is also included for comparison purposes and crosschecks.

3.1.1.1 The Cone Jet Energy Scale: Offset Correction

In the case of the cone algorithm, the calibration has been derived almost entirely from collider data [33]. The results were implemented in a computer program, henceforth referred to as CAFIX.

Physics Underlying Event

The correction associated with the contributions from the spectator partons is measured in a Minimum Bias (MB) sample. An event is called MB if it passes the Level Ø trigger condition, that is a crossing with an inelastic $p\overline{p}$ collision. Since the average inelastic $p\overline{p}$ collision corresponds to a glancing parton interaction, the E_T density (D_{MB}) is a good estimator of the physics underlying event. The contributions from uranium noise and pile–up, also present in this data, are derived from ZBnoLØ samples, events which do not pass the Level Ø trigger (no inelastic interaction). Low luminosity ZBnoLØ and MB samples were used to suppress multiple interaction events.

The energy density due to the physics underlying event, D_{ue}, is obtained using the relation:

$$D_{ue} = D_{MB} - D_{ZB}^{noL\emptyset} \tag{3.3}$$

where $D_{ZB}^{noL\emptyset}$ is the energy density measured in the ZBnoLØ samples. The energy subtracted from the jet is then calculated as $D_{ue} \times A$, where A is the area of the jet in η–ϕ space.

Uranium Noise, Pile–up and Extra Interactions

The offset contribution from uranium noise, pile–up and extra interactions is obtained by measuring the E_T density (D_θ) in ZB events. This is not an approximation, as opposed to the D_{ue} determination, where MB data only mimics the contributions from the underlying event. Zero-suppressed (ZS) samples were used to get this correction. As it was mentioned in section 2.2.4, this cut leaves, on average, some positive energy in each cell. The magnitude of this effect depends on the number of cells suppressed in an event. The occupancy factor ($\mathcal{F}$) is the number of cells read out in a given volume. It is different within a jet and in a ZB event. It also depends on the size of the cone jet because a smaller cone has a higher fraction of its cells read out. Since the offset subtraction is applied to jets, a correction has to be applied to take into account the difference between the suppression contributions. Thus, the density contribution to the offset due to noise, pile–up and extra $p\overline{p}$ interactions is given by:

$$D_\theta = D_{ZB}^{ZS} - \delta_{ZB} + \delta_{jet} \tag{3.4}$$

where D_{ZB}^{ZS} is the measured density in a ZB sample, δ_{ZB} is the E_T density contribution of the ZS cut in a ZB sample, and δ_{jet} is the E_T density contribution of the ZS cut within a jet. In order to measure δ_{ZB} and δ_{jet}, non zero-suppressed samples (NZS) are needed. Since no jet triggers were defined in the NZS sample, and knowing that the difference between the two is due to the occupancy factors ($\mathcal{F}_{jet}$ and $\mathcal{F}_{ZB}$), a prediction for δ_{jet} is derived from δ_{ZB} following the relation:

$$\delta_{jet} = \delta_{ZB} \times \frac{\mathcal{F}_{ZB}}{\mathcal{F}_{jet}} \tag{3.5}$$

$\mathcal{F}_{ZB}$ is obtained as the number cells read out in a particular η–ϕ bin divided by the total number of cells in that area. $\mathcal{F}_{jet}$ is calculated in the same way but within a jet. Figure 3.1 shows the occupancy for 0.7 cone jets as a function of pseudorapidity and for different jet E_T ranges. The E_T dependence was considered not large enough to require a separate parametrization. The prediction of δ_{jet} was found in agreement with the measurement obtained in a MB sample where jets were reconstructed ($\sim$ 5000 events).

The D_θ results were fit to an eight–parameter function:

$$D_\theta = a_1 + a_2\eta + a_3[\sin(a_4\eta + a_5)] + a_6[\sin(a_7\eta + a_8)] \tag{3.6}$$

The parametrizations are shown in Figure 3.2 as a function of pseudorapidity, for different luminosities.

3.1.1.2 The offset correction for the $k_\perp$ algorithm

The method used for the cone algorithm, which consists in measuring the energy density in different samples of DØ noise data, can not be used for $k_\perp$ jets. They do not have a fixed area in η–ϕ space. In order to determine the offset a new method has been developed as part of this thesis work. It basically consists on overlaying actual DØ noise data on Monte Carlo simulated physics events. The data with and without noise overlayed is processed through the reconstruction programs obtaining

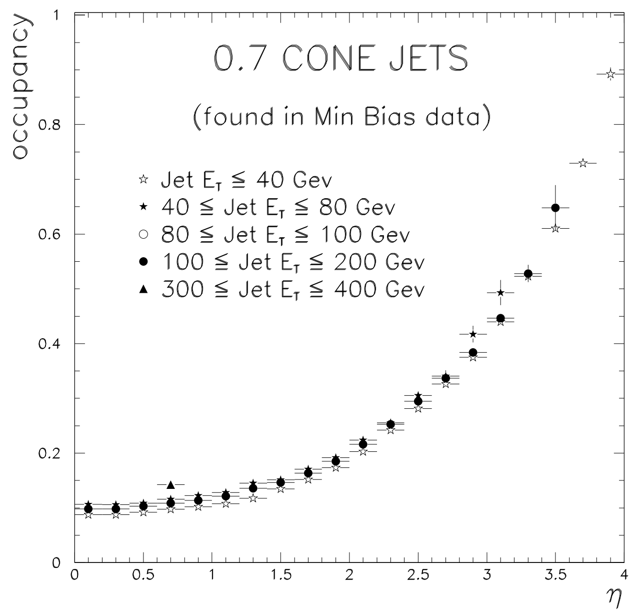

Figure 3.1: 0.7 cone jet E_T dependence of the occupancy as a function of pseudorapidity, for jets found in Minimum Bias data.

basically the same jets with and without noise contribution. The offset is then calculated by measuring the difference in jet p_T between the two samples. Three different types of DØ data are used. They are:

- **ZB** : Zero Bias data, which consists in random $p\overline{p}$ bunch crossings.
- **ZBnoLØ** : Zero Bias data not passing the Level Ø Trigger (random crossing with no inelastic interaction)
- **MB** : Minimum Bias data, which corresponds to a random inelastic $p\overline{p}$ collision.

ZB data corresponds to the contributions from uranium noise, pile–up and multiple interactions. The samples overlayed with ZB are used to get the O_{zb} offset. MB data, being basically low Q^2 $p\overline{p}$ collisions, mimics the contributions of the physics underlying event. Thus, samples overlayed with MB are used to measure the offset corresponding to the energy associated to the spectator partons. The energy from

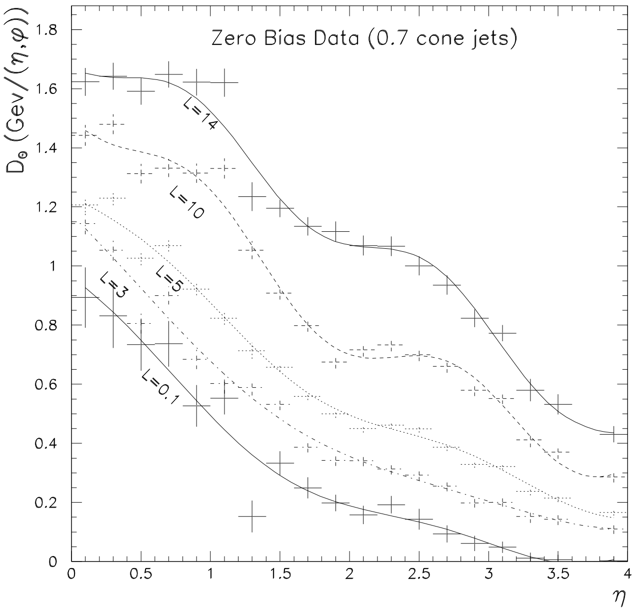

Figure 3.2: Energy density, D_θ. It corresponds to the contributions from uranium noise, pile–up and extra $p\overline{p}$ interactions. The parametrizations correspond to $R = 0.7$ cone jets.

uranium noise and pile–up, which are also present on MB data, is subtracted using the ZBnoLØ samples. Low luminosity MB and ZBnoLØ samples were used to suppress events with multiple interactions.

The Monte Carlo events were generated with HERWIG [34] with $2 \rightarrow 2$ parton p_T thresholds of 30, 50, 75, 100 and 150 GeV, and underlying event switched off. The samples were processed through the GEANT detector simulation package [29] which provides a cell–level simulation of the calorimeter response and resolution. The digitized Monte Carlo (MC) events were passed through the calorimeter reconstruction and jet finding packages, obtaining the first sample of jets. In the cases where DØ data was overlayed, the cell energies were added cell–by–cell to the energies in simulated MC jet events. Since the DØ data samples had to be non zero–suppressed, the summed cell energies were zero–suppressed offline and then passed through the calorimeter reconstruction and jet finding packages, producing a second sample of jets. The process to generate these samples is very time consuming. Although the best scenario would be to have various samples with different luminosities covering the whole range in pseudorapidity, only 5 different luminosities samples could be generated and with a range on pseudorapidity up to $|\eta| < 1$. A sample with mixed luminosities was generated extending up to $|\eta| < 3$ in order to get the functional form of the offset for the forward region ($|\eta| > 1$). Table 3.1 shows the different DØ data samples used to overlay MC events.

Type of Overlay	Herwig Threshold E_T (GeV)	Luminosity $\mathcal{L}$ ($10^{30}\,\mathrm{cm}^{-2}\mathrm{s}^{-1}$)	Jet η Range
none	30, 50, 75, 100, 150	N/A	$0.0 < \lvert\eta\rvert < 3.0$
ZB	30	5 (average)	$0.0 < \lvert\eta\rvert < 3.0$
ZB	30, 50, 75, 100, 150	0.1, 3, 5, 10, 14	$0.0 < \lvert\eta\rvert < 1.0$
ZBnoLØ	30, 50, 75, 100, 150	0.1	$0.0 < \lvert\eta\rvert < 1.0$
MB	30, 50, 75, 100, 150	0.1	$0.0 < \lvert\eta\rvert < 1.0$

Table 3.1: Availability of E_T, luminosity and η for overlayed Monte Carlo data.

Uranium Noise, Pile–up and Multiple Interactions

In order to measure the offset due to noise, pile–up and multiple interactions, a MC sample overlayed with ZB data and one without overlay are compared, on an event–by–event basis, associating the two most energetic jets in each sample. Figure 3.3 shows the distance in η–ϕ space (ΔR) between the leading jet (the most energetic one) in a MC sample with no overlay and the closest jet in the ZB sample. Two jets are then associated ("matched") when their distance is $\Delta R < 0.5$. The offset and its statistical error are extracted from the mean and RMS of the distributions of the p_T difference between matched jets (see Figure 3.4). Figure 3.5 shows the

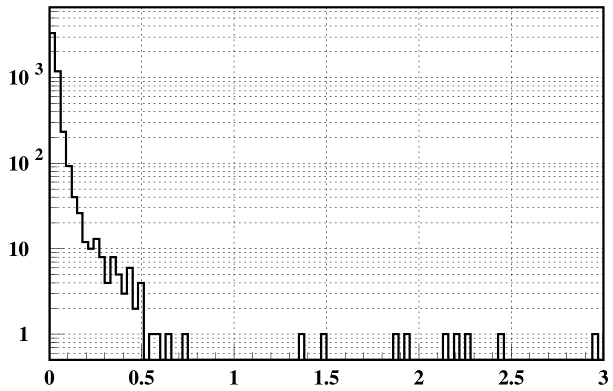

Figure 3.3: Distance in η–ϕ space from the leading $k_\perp$ jet in the MC sample without DØ data overlay to the closest jet in the sample overlayed with ZB data ($\mathcal{L} = 5$).

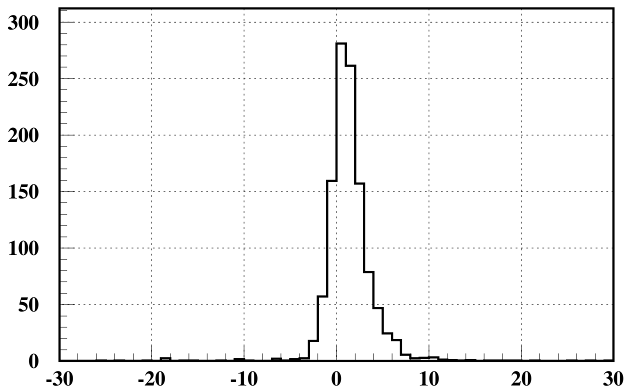

Figure 3.4: Distribution of p_T differences between corresponding $k_\perp$ jets in the MC sample overlay with ZB data ($\mathcal{L} = 5$) and the one without overlay.

offset O_{zb} as a function of pseudorapidity. The results for cone, obtained using the same method as for $k_\perp$, is shown for comparison. As it can be seen, in the central detector region, the offset is around 50% larger for $k_\perp$ than for cone. The curve obtained as a fit to the points has the same functional form that the one used for the cone calibration (see equation 3.6).

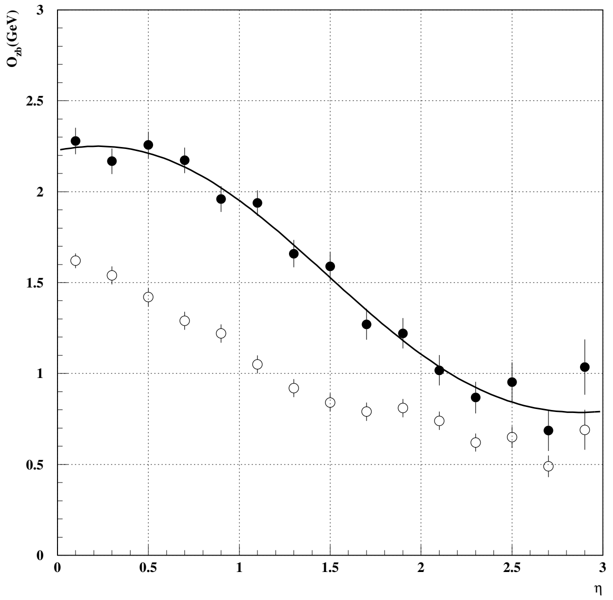

Figure 3.5: O_{zb} offset as a function of η for $k_\perp$ jets (full circles) with $30 < E_T < 50$ GeV (mixed luminosities). The result for cones are shown for comparison (open circles).

The measured O_{zb} values for $|\eta| < 1$ and for various luminosities are shown in Figure 3.6. The same functional dependence as the one obtained from Figure 3.5 has been used to estimate O_{zb} for the region $|\eta| > 1$. The curves correspond to the eight parameter function, fitted to the points and scaled with luminosity. Linear interpolations are done to extract the values for luminosities between the ones listed in Figure 3.6.

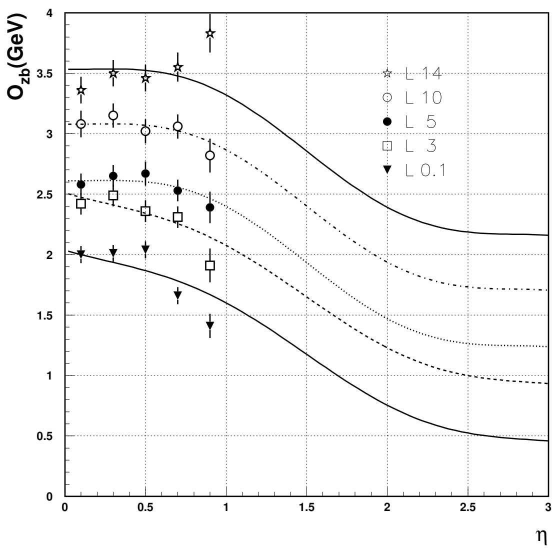

Figure 3.6: Parametrizations of the O_{zb} offset as a function of η for $k_{\perp}$ jets with $30 < E_T < 50$ GeV, for various luminosities.

The E_T dependence of the offset is shown in Figures 3.7 and 3.8. Very little dependence is observed and it becomes weaker as luminosity increases. Exponential fits were done for luminosities lower than $\mathcal{L} = 5$. A third degree polynomial is used to extract the dependence with η of the fits parameters.

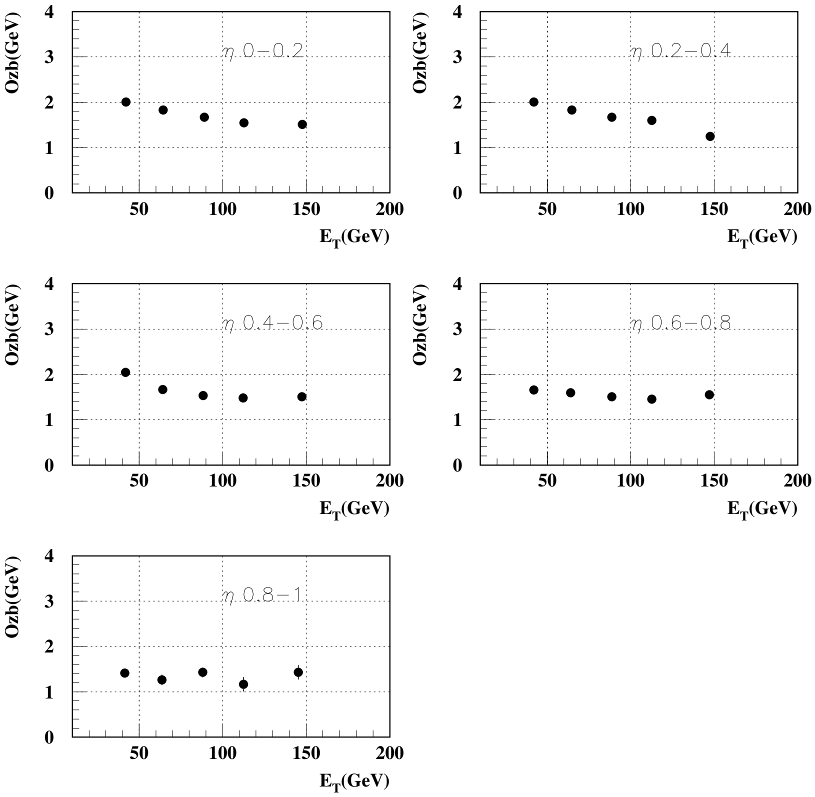

Figure 3.7: O_{zb} offset as a function of E_T at $\mathcal{L} = 0.1$ and several η bins, for $k_\perp$ jets.

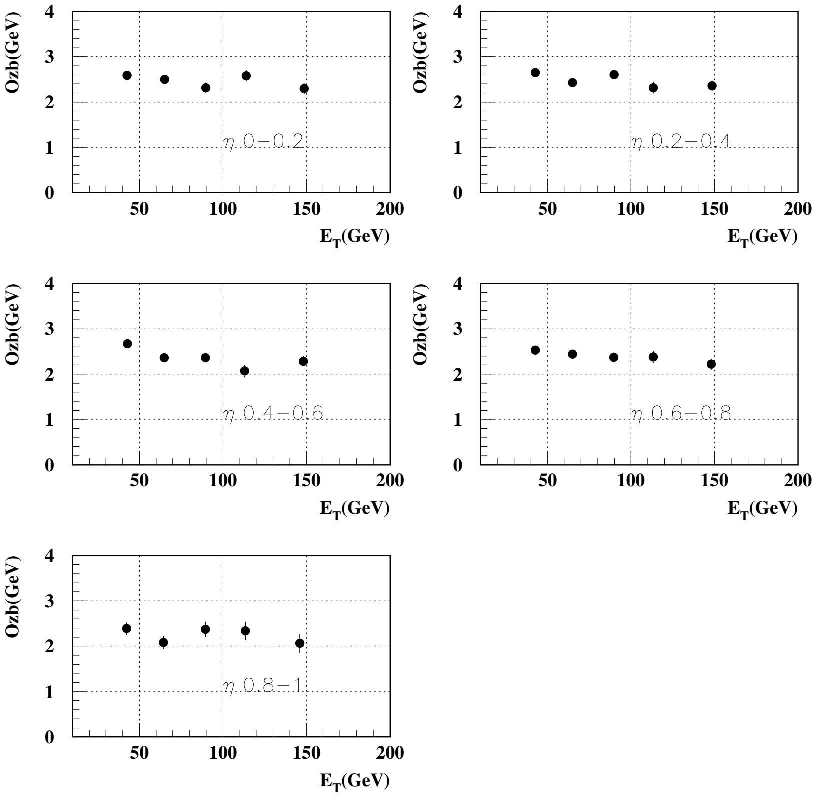

Figure 3.8: O_{zb} offset as a function of E_T at $\mathcal{L} = 5$ and several η bins, for $k_\perp$ jets.

Test of the Method

The method was tested by comparing the offset for the fixed cone jet algorithm calculated with our own method to the standard CAFIX results. Figure 3.9 shows the E_T dependence of O_{zb}. While CAFIX results were considered E_T independent, our new results show a drop with momentum. We believe this effect is real and that it was not fully appreciated in the cone analysis. Let us review how this conclusions were reached.

We think the discrepancy is due to zero–suppression (ZS) effects which depend on the number of suppressed cells. This is related with the occupancy $\mathcal{F}$, the fraction of cells read out inside the cone. The occupancy was measured for 0.7 cone jets in a MC sample overlayed with MB data and found in good agreement with the one calculated with jets taken from pure MB data (see Figures 3.1 and 3.10), showing that the overlay method correctly models the effects of underlying event and noise. By the time CAFIX results were derived, the occupancy was considered to be E_T independent. However, under close examination, an E_T dependence can be observed in Figure 3.1. When this effect is taken into account by varying the occupancy values on equation 3.5, a 30% of the O_{zb} E_T dependence can be explained (because ZS effects were not well understood, a large error was included in CAFIX). Since the E_T dependence of 0.7 cone jets cannot be confirmed with pure DØ data, a 70% of the E_T dependence correction for $k_\perp$ jets was introduced as an error.

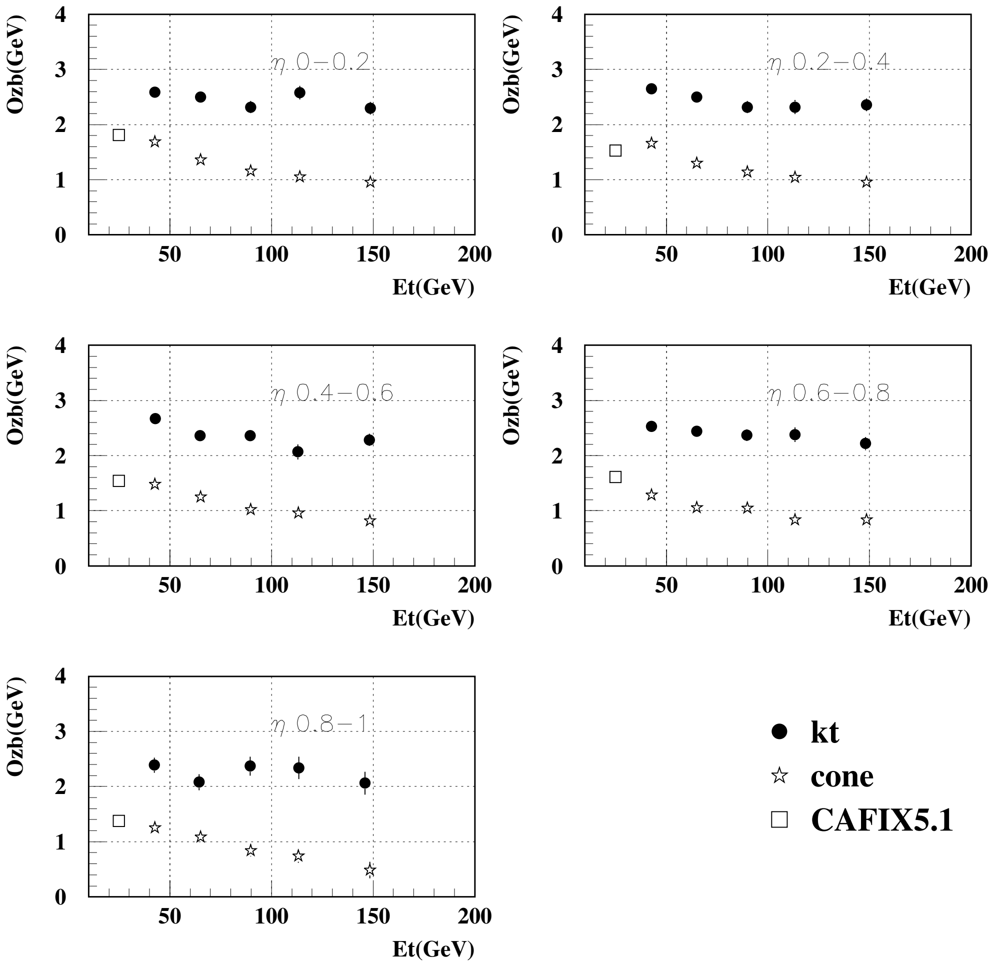

Figure 3.9: O_{zb} offset for $k_\perp$ (full circles) and 0.7 cone jets (stars), reconstructed in Monte Carlo data overlayed with Zero Bias (at $\mathcal{L} = 5$) as a function of E_T for different η bins. The CAFIX result is shown for comparison on the left (open box), but no E_T is associated with it.

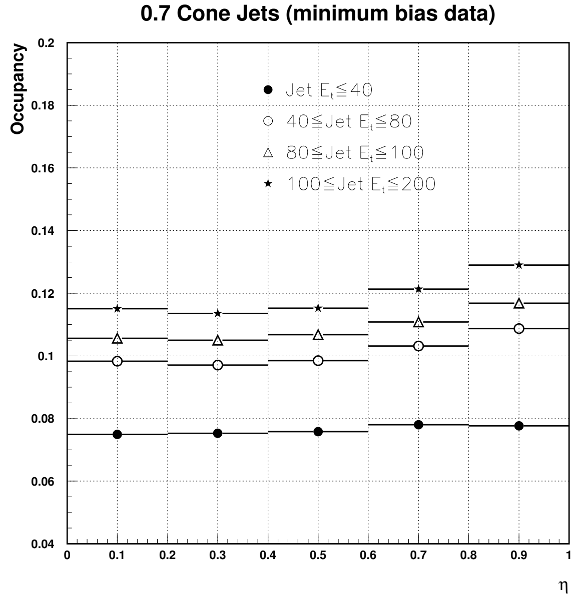

Figure 3.10: 0.7 cone jet E_T dependence of the occupancy as a function of jet pseudorapidity, for jets found in Monte Carlo events overlayed with Minimum Bias data.

Final Results

The final results, which consider together the E_T and η dependence, are shown in Figures 3.11 and 3.12. The main source of uncertainty is the error arising from the disagreement in the E_T dependence between the results of O_{zb} for cone jets and the ones from CAFIX. This uncertainty increases with energy and for low luminosities values. It can be as large as 15%. The functional form extracted from Figure 3.5 contributes with an error of 0.2 GeV calculated as the average of the largest differences between the points and the fits for each curve in Figure 3.6. No measurements exist for energies greater than 200 GeV. An additional uncertainty was introduced which rises smoothly from 0.0 to 0.2 GeV between 120 GeV and 270 GeV and above this value it remains flat.

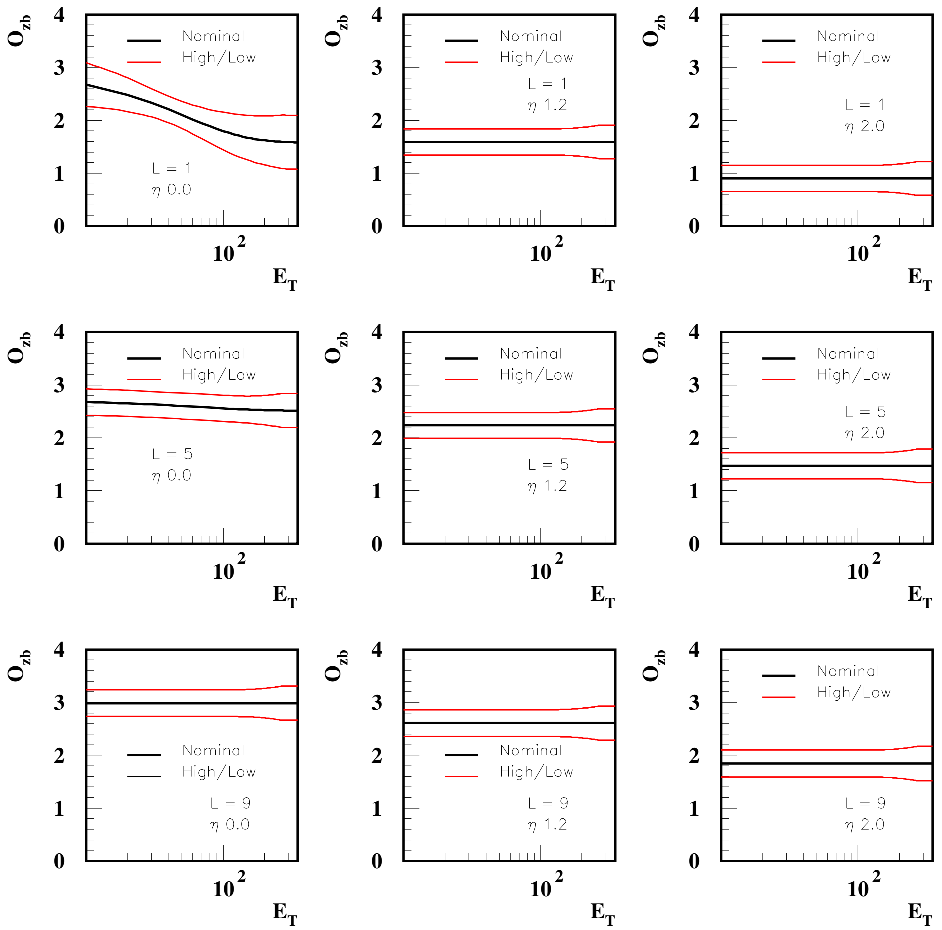

Figure 3.11: The final O_{zb} offset and the corresponding systematic errors as a function of E_T for $k_\perp$ jets with $D = 1$, at $\eta = 0.0, 1.2$ and 2, and for luminosities $\mathcal{L} = 1, 5$ and 9.

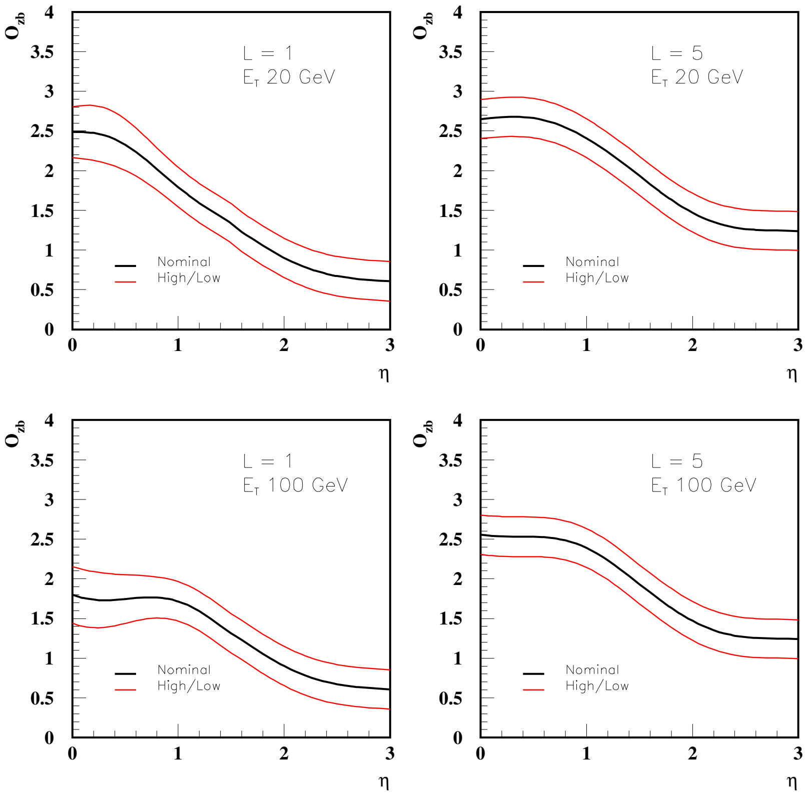

Figure 3.12: The final O_{zb} offset and the corresponding systematic errors as a function of η for 20 and 100 GeV $k_\perp$ jets with $D = 1$ for luminosities $\mathcal{L} = 1$ and 5.

Physics Underlying Event

In order to measure the contributions from the physics underlying event, jets are matched ($\Delta R < 0.5$) between the MB and ZBnoLØ samples and their energy subtracted. The dependence on E_T is shown in Figure 3.13. There is no evidence of an E_T dependence, therefore the correction is only applied as a function of η.

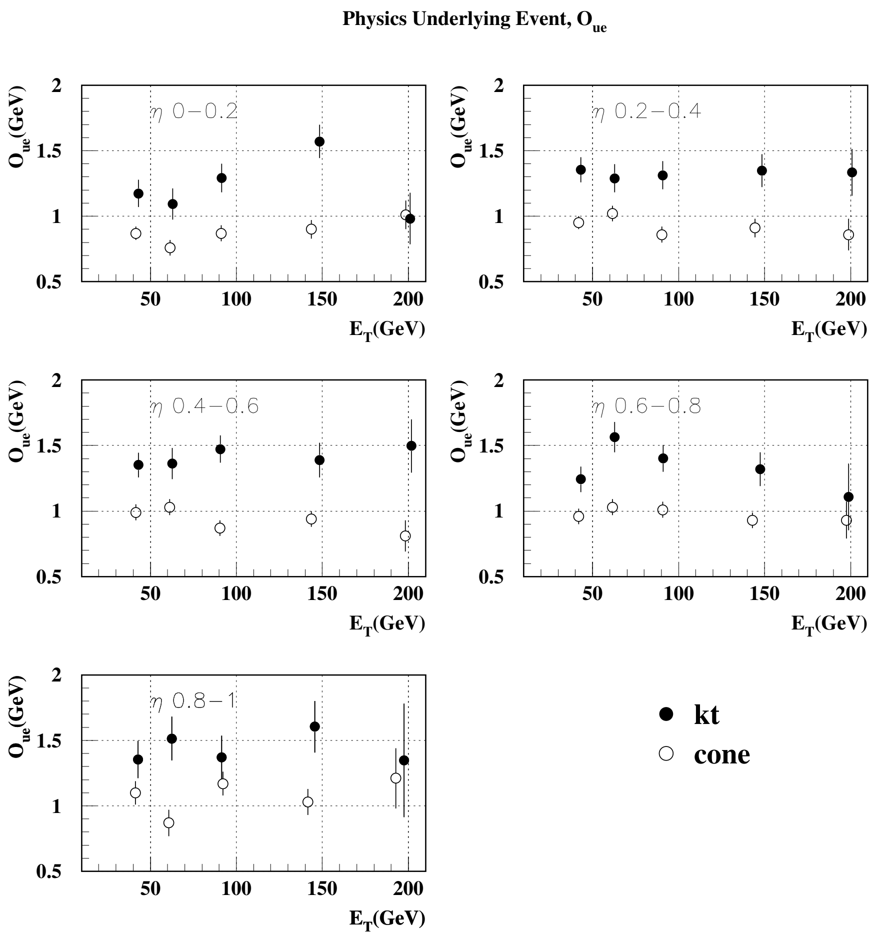

Figure 3.13: Physics underlying event offset, O_{ue}, as a function of E_T for $k_\perp$ jets. The result for cone is shown for comparison.

The functional form of the correction for regions other than the central one ($|\eta| > 1$) is based on cone results [31]. The cone offset was calculated using the overlay method and compared with the result from CAFIX. The good agreement obtained provides another successful test for the method and it allows to use CAFIX results to derive the η dependence of O_{ue} for $k_\perp$ jets (see Figure 3.14). The average difference between the $k_\perp$ and cone offset was calculated and then added to the CAFIX points normalized to our cone results. The final underlying event offset, O_{ue}, is shown in Figure 3.15. A 10% error comes from the quadrature sum of 0.1 GeV uncertainty due to the normalization process and an equal amount to accommodate a possible E_T dependence. This error was enlarged to 15% for the region $|\eta| > 1$ where no measurement of O_{ue} for $k_\perp$ jets is available.

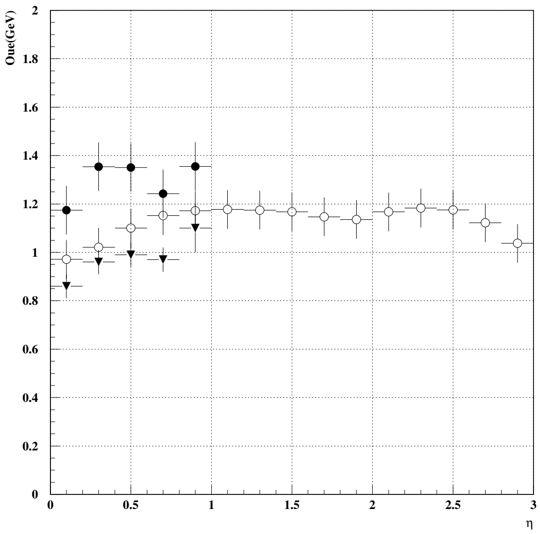

Figure 3.14: Physics underlying event offset, O_{ue}, as a function of η for $k_\perp$ jets (solid circles) and cone jets (triangles), together with the results from CAFIX (open circles).

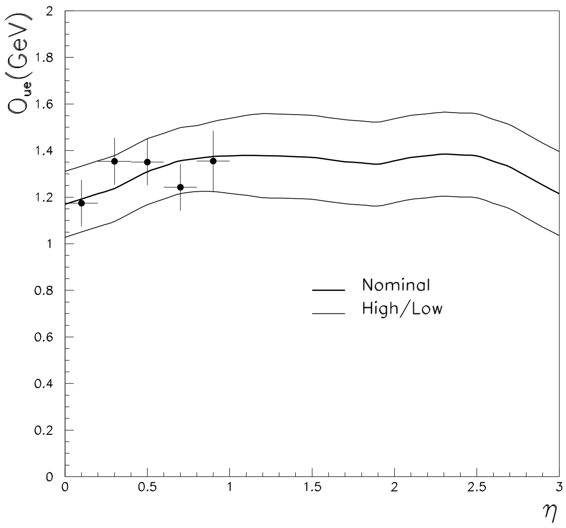

Figure 3.15: Physics underlying event offset correction, O_{ue}, as a function of η for $k_\perp$ jets with $D = 1$. The solid curve (middle) is the fit to the points, motivated by the functional form in [31], and the band represents the systematic errors.

3.1.1.3 Summary

The jet momentum measured by the calorimeters is distorted by experimental effects. The energy contributions from the physics underlying event, uranium noise, pile–up and multiple interactions (offset) have to be subtracted. Since $k_\perp$ jets do not have a fixed area, a new method was developed to calibrate these jets based on the experience with the cone algorithm. Basically, the offset is calculated by measuring the difference in jet p_T between two MC samples, where one them has been overlayed with actual DØ noise data in order to simulate the physics underlying event and noise contributions. The total measured offset in the central part of the detector is around 4 GeV with an approximated 10% error, for an instantaneous luminosity of $\mathcal{L} = 5\,10^{30}\,\mathrm{cm}^{-2}\mathrm{s}^{-1}$. This value decreases for the forward regions and increases for larger $\mathcal{L}$.

Offsets for $k_\perp$ (for $D = 1$) have proved to be in general between 50% to 75% larger than the offsets for the fixed cone jet algorithm (with $R = 0.7$). The $k_\perp$ algorithm clusters everything into jets "pulling" more noise and underlying event than a fixed cone (which excludes all energy outside the cone radius).

3.1.2 The Response Correction

The jet momentum response in the DØ experiment is measured from collider data using p_T conservation in photon–jet (γ–jet) events. In an ideal calorimeter, the total missing transverse energy should be zero. However, in real calorimeters, the measured photon and jet transverse momenta may not balance perfectly. The photon momentum scale is determined from $Z \to e^+e^-$, J/ψ and π^0 data samples using the masses of these known resonances. After calibration and recalculation of the event $\not{E}_T$, the calorimeter response to jets (R_{jet}) can be derived from :

$$\vec{p}_T^{\,\gamma} + R_{jet}\ \vec{p}_T^{\,jet} = -\vec{\not{E}}_T \tag{3.7}$$

By projecting along the transverse direction of the photon (unit vector $\hat{n}_\gamma$) and using the transverse momenta balance relation at the particle level ($p_T^{\gamma} = -\hat{n}_\gamma \cdot \vec{p}_T^{\,jet}$), equation 3.7 can be rewritten as:

$$R_{jet} = 1 + \frac{\hat{n}_\gamma \ \cdot \vec{\not{E}}_T}{p_T^{\gamma}} = 1 + MPF \tag{3.8}$$

The missing E_T projection fraction, or MPF, is the fraction of the $\not{E}_T$ projected onto the direction of the photon.

The jet response is expected to be momentum dependent. In order to avoid resolution and trigger biases, R_{jet} is binned in terms of $E' = p_T^{\gamma}\ \cosh \eta_{jet}$, and then mapped onto p_{jet}. E' depends only on photon variables and jet pseudorapidity, which are quantities measured with very good resolution. Figure 3.16 shows the calorimeter response to $k_\perp$ jets (R_{jet}) as a function of p_{jet}. The data is fit with the functional form $R_{jet} = a + b\ \ln p + c\ \ln^2 p$ (see [32]).

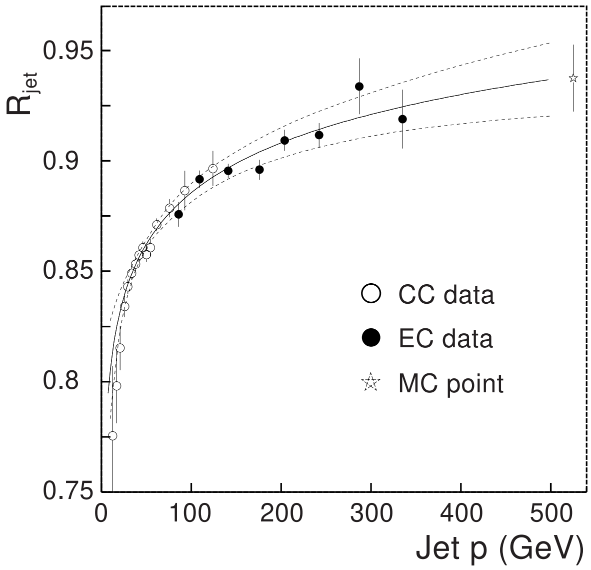

Figure 3.16: The calorimeter response correction, R_{jet}, for $k_\perp$ jets with $D = 1$, as a function of jet momentum. The Monte Carlo point is used to constrain the fit (solid) at high jet momentum. The dashed curves denote the systematic error.

3.1.3 Monte Carlo Closure

In order to test the method, the corrections were derived for a Monte Carlo direct photon sample. The $k_\perp$ jets were then reconstructed and their momentum corrected. Figure 3.17 shows the ratio of the corrected jet momentum to the corresponding particle jet momentum. The result is consistent with unity.

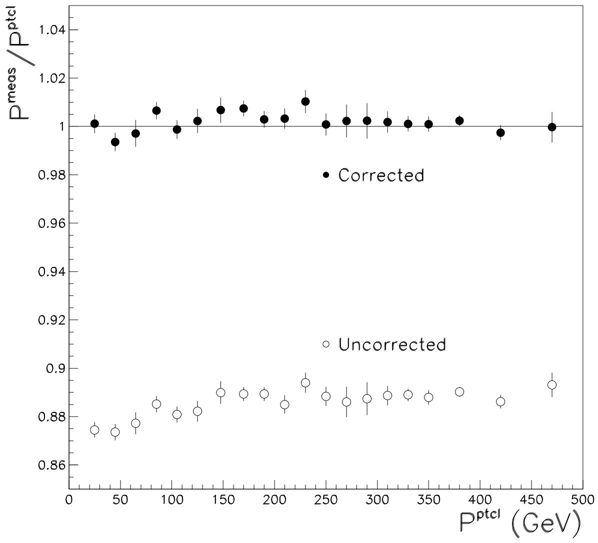

Figure 3.17: Monte Carlo closure in the central region for $k_\perp$ jets. The open circles correspond to the ratio between the uncorrected calorimeter jet momentum and the corresponding particle jet momentum as a function of particle jet momentum. The ratio is consistent with unity when the corrected momentum is used (solid circles).

Chapter 4

Selection of the Observable

Since there was no prior experience on event shapes analyses in hadron colliders, a considerable part of the work involved in this thesis consisted in the election of the observable to measure. This task was done in collaboration with members of the Fermilab Theoretical Physics Department. In particular, we would like to thanks Walter Giele and Keith Ellis for their invaluable contributions and fruitful discussions. This chapter summarizes these studies and conclusions.

4.1 Introduction

As it was mentioned in section 1.4, event shapes have been previously studied in $e\bar{e}$ and ep, however, hadron colliders presents a different environment that difficults these measurements. There are two factors that need to be taken into account. First, the parton-parton center–of–mass frame is boosted from event to event with respect to the laboratory frame and second, a fraction of the energy deposited in the detector is not associated with the primary hard interaction, but originates from the physics underlying event (contributions due to soft interactions between spectator partons), additional $p\bar{p}$ interactions, signals from previous crossings (pile–up) and noise. In order to overcome these two problems, we have decided:

- to replace the momenta by the transverse momenta, making the variable Lorentz invariant under z-boosts
- to measure Thrust using jets for which we derived a correction that removes in average noise and other experimental effects from the measured momenta (chapter 3).

We have conducted several prospective studies to define the variable to measure using HERWIG, a MC event generator. This program, together with the DØ reconstruction software, allows to compare generated events at particle level with reconstructed ones at the calorimeter. In this way, it is possible to analyze the detector performance to reconstruct events and to study the distortions introduced to the kinematic and physics variables due to genuine background sources (soft interactions among spectator partons), from the accelerator (multiple interactions and pile–up) and from the detector itself. These effects render certain observables of physics interest in $p\overline{p}$ collisions impossible to measure.

MC Samples

We generated QCD dijet events at $\sqrt{s} = 1800\,\text{GeV}$ using HERWIG 5.9 [34], requiring the parton p_T to be greater than 25, 50, 75, 110 and 150 GeV. Next, we processed the five samples through a GEANT simulation of the DØ detector (SHOWERLIB [30]) and overlayed the result with zero bias (ZB) DØ data, taken for a range of luminosities, to simulate experimental effects such as additional $p\bar{p}$ interactions, pile–up and noise. Jets were reconstructed both at particle and calorimeter level using the $k_\perp$ algorithm described in section 1.3.3 ($D = 1$).

4.2 Dijet Transverse Thrust

The distortions introduced by experimental effects on Thrust were studied with MC simulated events, by comparing particle to calorimeter level distributions, with thrust calculated with different number of jets. The method to determine the thrust axis and its values follows the algorithm described in Ref. [35] and detailed in Appendix A. From the comparison with calorimeter distributions in an ideal no-noise environment, it is possible to analyze the distortions due to calorimeter momentum response, resolutions and showering. The noise, multiple interactions and pile-up effects are studied in a sample overlayed with ZB DØ data taken at $\mathcal{L} = 5 \times 10^{-30}\,\mathrm{cm}^{-2}\mathrm{s}^{-1}$, the data average Luminosity.

Figure 4.1 shows thrust distributions calculated using all jets in the events, corrected by the Jet Momentum Scale [32]. It was required the jets to have $|\eta| < 1$ since it is the region of the detector that is better understood, where most of the analysis at DØ were performed and where calibration uncertainties are minimum. It can be observed that the effects of the calorimeter momentum response, resolutions and showering are minimal as compared to the distortion of the distribution due to noise. The Jet Momentum Scale corrects the momentum back, on average, to particle level (before the interaction with the calorimeter), but the correction does not eliminate background jets ("noisy jets") which are not related with the hard interaction itself. Events move from high Thrust bins to lower ones because on average the addition of a randomly oriented noise jet renders the event more isotropic.

The question is, therefore, how to modify the variable to be measured in a hadron collider, eliminating noise effects but without degrading the observable to the point that it loses its physical interest. This issue was discussed with theoreticians in the Run II QCD Workshop [6], held at Fermilab. One of its goals was to study and develop standard jet algorithms and to explore prospective jet measurements. It was suggested to cut the number of jets used in the calculation, since the remaining ones

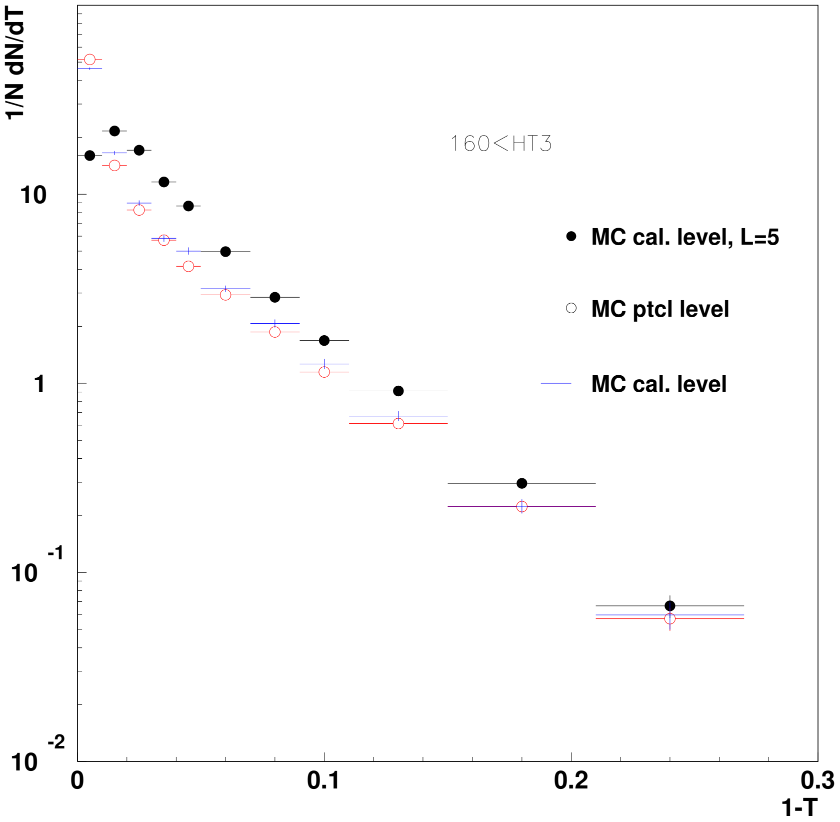

Figure 4.1: Normalized Transverse Thrust (T) distributions as a function of 1-T. Thrust was calculated using all jets in the event with $|\eta| < 1$. Full circles correspond to calorimeter level HERWIG MC overlayed with ZB data at $\mathcal{L} = 5$, open circles to particle level and lines to calorimeter level without added noise. HT3 is a measure of the energy scale of the event and is defined as the sum of the transverse momenta of the three most energetic jets.

would contain implicitly the kinematic information of the discarded jets. A cut on the energy of the jets was ruled out since it makes the theoretical predictions infrared unsafe. For example, the results will be different if a jet which passes the E_T cut is split in two of lower energy, below the E_T threshold, due to collinear emissions.

In order to determine how many jets we could use in the calculation, we studied the problem of the spurious jets. Using the MC samples, for each calorimeter jet we looked for a corresponding particle one, according to their closeness in η–ϕ space. Jets unmatched are mostly likely to be product of contamination. This is illustrated in Figure 4.2, where jets have been matched requiring $\sqrt{\Delta\eta^2 + \Delta\phi^2} < 0.5$ (see section 3.1.1.2). The plotted transverse energy spectrum corresponds only to the unmatched jets and goes up to 15 GeV. Figures 4.3 and 4.4 show how the E_T spectrum looks in data, for the cases of the third and fourth jet (numbered in decreasing order of energy). Around 40% (80%) of the third (fourth) leading jet are in the low energy range ($E_T < 15$ GeV). The probability for a jet to be displaced by a noisy one, increases as their energy decreases.

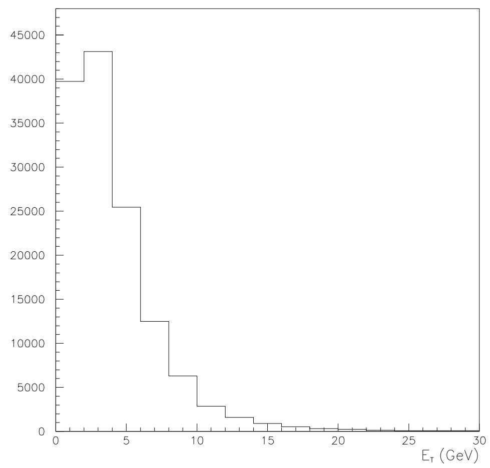

Figure 4.2: E_T spectrum of unmatched jets. The criteria used to match jets between detector and particle level was: $\sqrt{\Delta\eta^2 + \Delta\phi^2} < 0.5$.

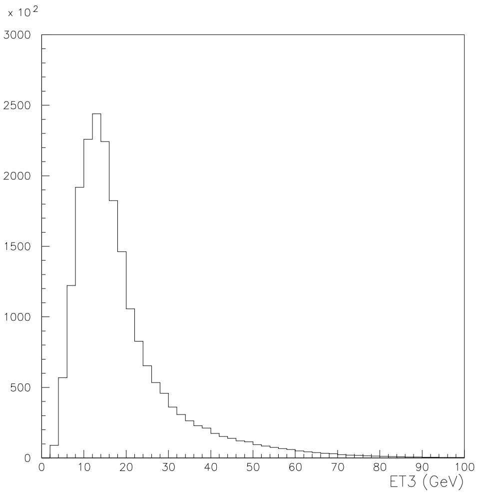

Figure 4.3: E_T spectrum of the third leading jet in data events. Around 40% of the jets are below 15 GeV.

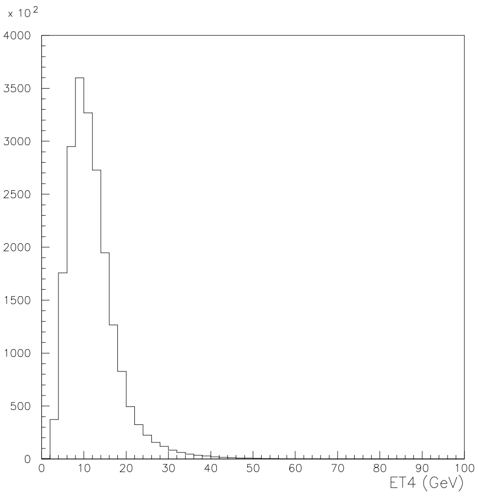

Figure 4.4: E_T spectrum of the fourth leading jet in data events. Around 80% of the jets are below 15 GeV.

We have obtained several Thrust distributions for different number of jets included in the calculation. Figure 4.5 presents the case where only two jets have been used and the ratio between the distributions in a logarithmic scale is shown in the top plot of Figure 4.6. An excellent agreement is observed between particle and calorimeter level.

On the other hand, our studies indicate that including a third jet in the calculation introduces a distortion in the measured distribution. We find that about 40% of the events entering in Figure 4.5 have a third leading jet with $|\eta| < 1$ at calorimeter level. The bottom plot in Figure 4.6 compares for these events the thrust distribution at calorimeter and particle level, where in the latter we include the third jet if $|\eta_3| < 1$. The ratio clearly departs from unity indicating that a distortion is produced by including one more jet in the calculation. This systematic effect is in part due to contamination. This is to be expected in the light that 40% of the third leading jets are in the low energy range ($E_T < 15$ GeV) where they can be displaced by a background jet which on average, as it is uncorrelated with the physics, will pull the thrust down.

In view of these results, we have decided to measure transverse thrust calculated with the two leading jets in the events. The kinematic information of other jets in the event is implicitly included through the position and energy of the leading ones. The variable will be referred to as Dijet Transverse Thrust (T_2^t)[1].

4.3 The energy scale of the event

Another issue to be studied is the variable in terms of which the T_2^t is going to be presented. One of the aims of this analysis is to measure the distributions as a function of the energy scale of the hard interaction. However, this variable is not

[1]We would like to thanks G. Sterman for his suggestion of measuring the Dijet Thrust.

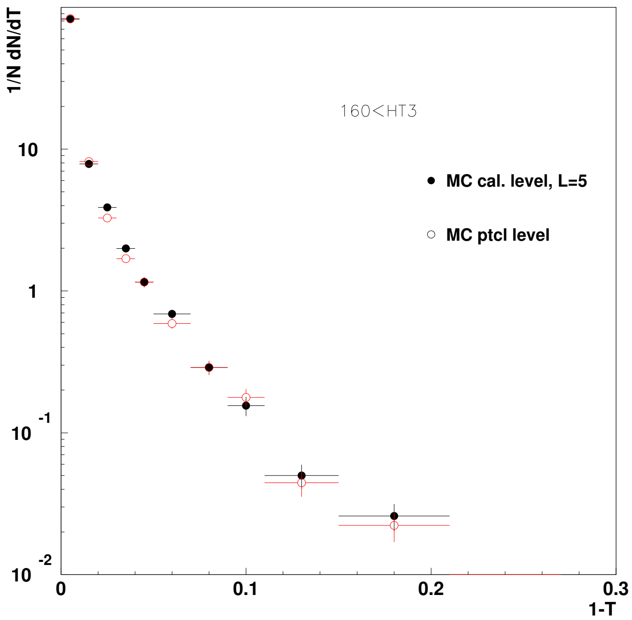

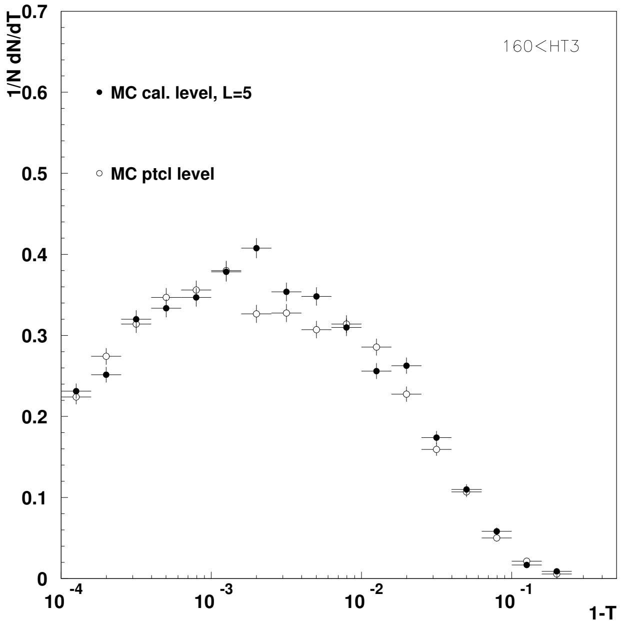

Figure 4.5: Normalized Transverse Thrust distributions as a function of 1-T. Thrust was calculated using the two leading jets in the event. Full circles correspond to calorimeter level HERWIG MC overlayed with ZB data, open ones to particle level. Bottom: results are plotted in a logarithmic scale.

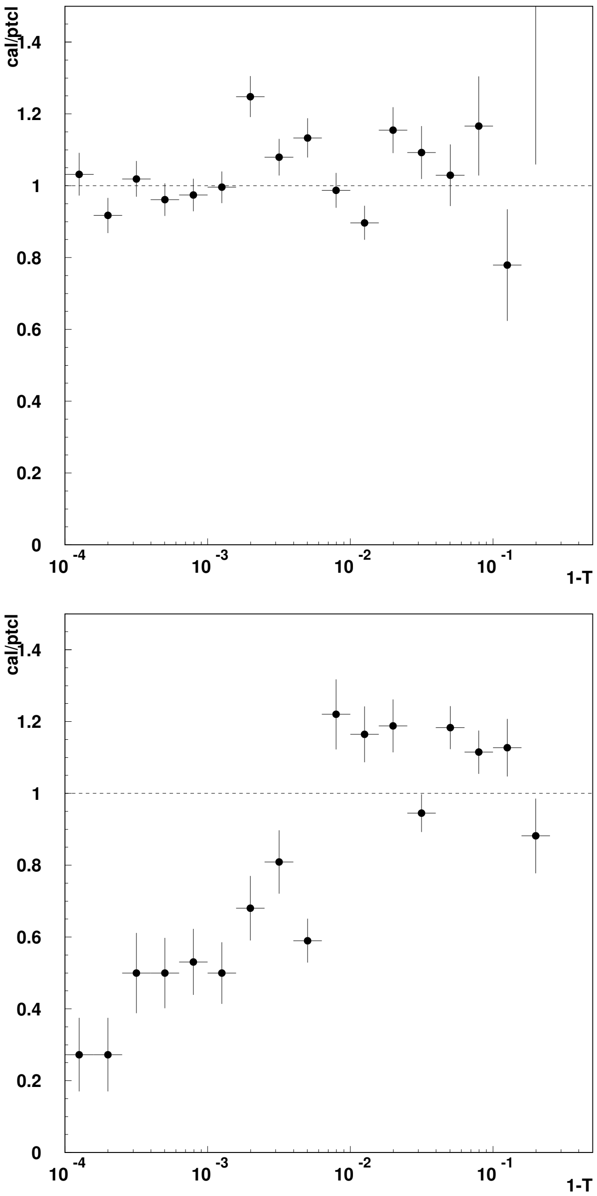

Figure 4.6: Top: Ratio between calorimeter and particle normalized Transverse Thrust distributions as a function of (1-T). Thrust was calculated using only the two leading jets in the event. Bottom: the same as the top plot when Thrust is calculated using only the three leading jets in the event. Results are plotted in a logarithmic scale.

measurable in hadron colliders. Nevertheless, there are other observables that might be used, as for example HT, the scalar sum of the transverse energy of all jets in the event. However, HT includes many low energy jets, which have a high probability to be contamination and are not eliminated by applying the Jet Momentum Scale correction. An alternative to HT is HT3, the scalar sum of the transverse energy of the three leading jets in the event. Even though there is a probability for the third jet to be spurious, this is much more unlikely, as explained before, than for lower energy jets.

The effect of the third jet in the case of HT3 is different than in the Thrust calculation. Its presence cannot be inferred from the sum $E_{T\,1} + E_{T\,2}$, as illustrated for instance in the 30% error incurred in the 'Mercedes' configuration. Using the MC samples, we have analyzed the correlation between HT3 and HT, the latter calculated at the parton level corresponds to a measure of the energy scale of the hard interaction. As shown in Figure 4.7, there is a linear correlation, with a slope close to 1, between the two observables. HT3 is then the result of a compromise of low sensitivity to noise and high correlation with the energy scale.

4.4 Kinematic cuts

Since the central region is very well instrumented and the corrections for detector effects are well understood, the η of the leading jets for the event to be considered will be required to be $|\eta_{1,2}| < 1$. Regarding the pseudorapidity range for the third jet, since the Jet Momentum Scale correction is not known when $|\eta| > 3$, it was first thought to discard events in cases where $|\eta_3| > 3$. However, this cut cannot be implemented in Jetrad in an infrared safe way, because the NLO prediction for the cross section in the bin that includes $T_2^t = 1$ becomes dependent on the unphysical s_{min} parameter (which slices for computational purposes the phase space into disjoint 2-parton and a 3-parton regions). In effect, consider a spatially well

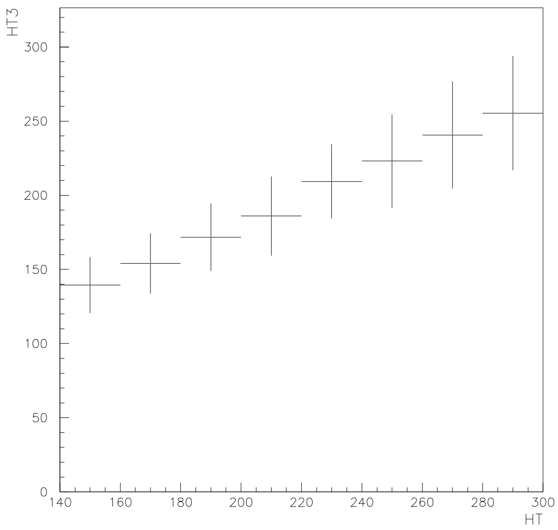

Figure 4.7: HT3 as a function of HT (calculated at the parton level), using an energy scale corrected HERWIG MC sample (overlayed with RunI DØ data at $\mathcal{L} = 10 \times 10^{-30}\,\mathrm{cm}^{-2}\,\mathrm{s}^{-1}$).

separated three parton event with a soft parton at $|\eta| > 3$. For small values of s_{min} this third parton gives rise to a jet at $|\eta| > 3$, and the event is therefore discarded. At high s_{min}, however, the third soft parton is not resolved and we get an effective two parton event, which passes our cuts. This is illustrated in Figure 4.8 which shows JETRAD predictions for $s_{min} = 1$ and 10 GeV^2. The cross section obtained with the lower s_{min} value, is negative for the first T_2^t bin. This happens since many three partons events, needed to compensate the large negative value for the point $T_2^t = 1$, are discarded due to the pseudorapidity cut. Instead those events make it to the cross section for $s_{min} = 10$ GeV^2 since they are not considered three parton but two parton events. We thus decided to keep all of them regardless of the kinematics of the third jet. For the cases where $|\eta_3| > 3$, the third jet will not be included in the calculation of HT3 (this effectively means to use HT2 instead of HT3).

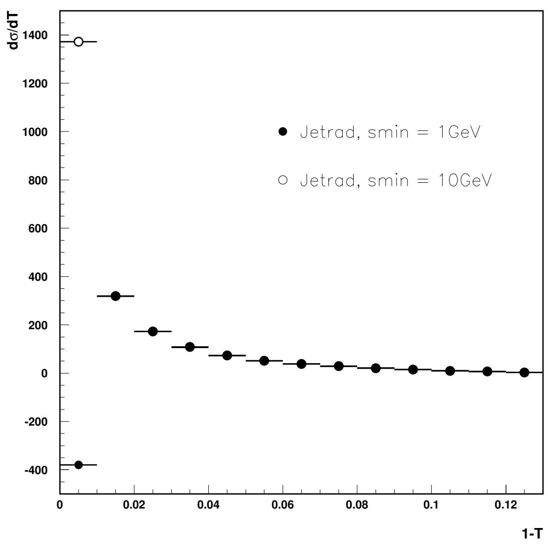

Figure 4.8: Jetrad predictions for different s_{min} values when imposing an η cut on the third jet used to determine HT3. The full circles corresponds to $smin = 1$ GeV^2 and the open ones to $smin = 10$ GeV^2.

Chapter 5

Data Samples

The analysis is based on Run Ib data, reconstructed in the DØfix environment [36]. This software package includes the $k_\perp$ ($D = 1$) and cone ($R = 0.7$) algorithms. Events were required to pass the inclusive jet triggers Jet_30 Jet_50 Jet_85 and Jet_Max (section 2.3.4).

Although the observed jets are most often produced as a result of hard $p\overline{p}$ collisions, there are other processes that can mimic the energy deposits of genuine jets in the calorimeter. These processes include cosmic rays, losses of protons from the main ring[1], electrons or photons misidentified as jets, and electronic malfunctions. This chapter presents the corrections applied to the reconstructed QCD events and the cuts the DØ QCD group has designed to remove "fake" jets from the data sample.

5.1 The treatment of Hot Cells

During Run Ib a cell suppressor, called AIDA [37] (Anomalous Isolated Deposit Algorithm), was introduced in order to remove cells with spurious energies and unusual high frequencies of occurrence (*hot cells*). The appearance of the cells is

[1] The Main Ring pipeline runs through the calorimeter.

due to electronic noise and hardware failures in the calorimeter.

AIDA is applied event by event, prior to jet finding. Cells with $E_T > 10$ GeV and more than 20 times the average E_T of its first longitudinal neighbors (adjacent cells with lower and higher layer numbers), are suppressed. The disadvantage of this procedure is that it damages many genuine jets by eliminating good isolated cells which are the result of natural fluctuations due to the stochastic nature of hadronization and shower development, and calorimeter segmentation. Following [37], AIDA cells, were restored to the jet provided their distance, in the $\eta - \phi$ space, is less than $\Delta R = 1$ respect to the original jet direction, and its energy is less than 50% of the jet transverse energy. All the relevant variables were recalculated following the $k_\perp$ algorithm recombination scheme.

5.2 The $\vec{\mathcal{H}}_T$ Correction

Due to the high instantaneous luminosity, $p\overline{p}$ bunch crossings could have more than one inelastic interaction. In these cases, the event vertex is determined as the one which minimizes the magnitude of the vector sum of the jet transverse energy ($\vec{\mathcal{H}}_T$). This procedure is called Revertexing [38]. If the selected vertex is not the one choose by the tracking software (the candidate with more tracks) all the relevant variables are recalculated. We found that 20% of the events need to be revertexed.

5.3 Jet Quality Cuts

Noise sources like instrumental background and Main Ring activity leave energy deposits in the calorimeter which are misidentified as jets. In order to remove these "fake" jets, the standard jet quality cuts were applied [39] (after running the cell restoration algorithm and the $\vec{\mathcal{H}}_T$ correction) in a jet-by-jet basis. These cuts are based on the EMF and CHF variables which are defined as the fraction of the energy deposited in the electromagnetic and hadronic sections of the calorimeter, respectively. The requirements for each variable are:

$0.05 < EMF < 0.95$

$CHF < 0.4$

Events are discarded if at least one of the two leading jets was determined to be a *bad jet*. In case the third jet is *bad*, HT2 is used instead of HT3.

5.4 Event quality Cuts

Events are selected by applying cuts on the missing transverse energy and on the primary vertex position. These cuts are applied after running the cell restoration algorithm and the $\vec{\mathcal{H}}_T$ correction.

5.4.1 R_{MTE} cut

In order to eliminate cosmic ray events and to remove unusual *fake* jets that survive the standard cuts, it was required [40] that each event satisfies the following condition on the ratio between the missing E_T ($\not\!\!E_T$) and the transverse energy of the leading jet (E_T^{Ljet}):

$R_{MTE} = \not\!\!E_T / E_T^{Ljet} < 0.7$

This cut takes care of most cosmic rays events (except those that happen to pass through the beam spot) because they are not transversely balance in energy.

5.4.2 Vertex cut

The measured primary z-vertex was required to be $|z| < 50\,cm$. This cut is implemented to preserve the projective geometry of the calorimeter towers. Figure 5.1 shows the distributions of the z coordinate of the vertex position for each trigger.

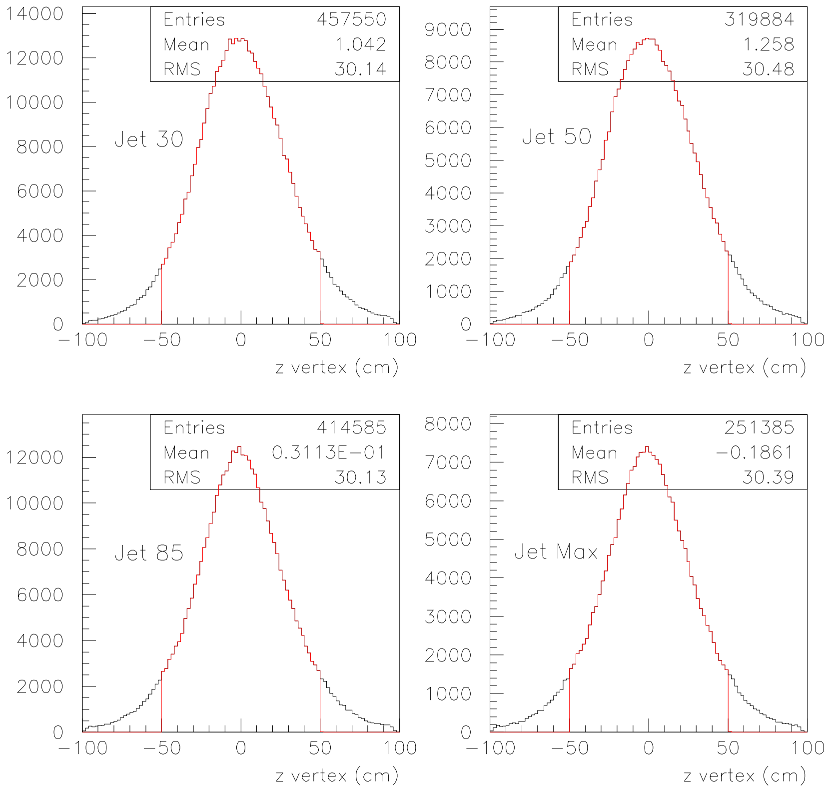

Figure 5.1: Distributions of the z-vertex for each trigger

5.5 Cut efficiencies

Good events or jets, which sometimes fluctuate outside the thresholds described above, could be erroneously eliminated. In order to compensate for their removal, event and jet efficiencies were derived for each of the cuts previously mentioned. Details of the calculation can be found in [39]. Basically, each variable is plotted and fit to a smooth curve, obtaining what is called the *true* distribution. The efficiencies are defined as the fraction of good jets (or events in the case of the z-vertex and the $\not{E}_T$ cut) between the thresholds.
The jet quality cuts efficiency, e_{qc}, is parametrized as a function of E_T as [41, 42]:

$$e_{qc} = 0.9997 + (-0.21\,10^{-4}) \times E_T \tag{5.1}$$

Since the calculation of the T_2^t cross sections could involve two or three jets (it depends on the η of the third jet, see section 4.4), the total efficiency for the event is obtained through:

$$e_{qc} = \prod_{i}^{N} e_{qc_i} \tag{5.2}$$

where e_{qc_i} is the efficiency corresponding to the i–th jet and N is the number of jets used in the calculation.

Table 5.1 shows the z-vertex cut efficiency (e_{zvtx}) obtained from Figure 5.1. The $\not{E}_T$ cut was determined to be 99.8% efficient (e_{met}) [40].

Jet_30	Jet_50	Jet_85	Jet_Max
0.8995 ± 0.0003	0.8969 ± 0.0004	0.8985 ± 0.0004	0.8960 ± 0.0005

Table 5.1: Vertex cut efficiency for each trigger.

5.6 Trigger Thresholds

The T_2^t cross section will be presented in four HT3 bins. Figure 5.2 shows the distributions of HT3 for each jet trigger, corrected by inefficiencies and momentum scale. Only one trigger is used per HT3 bin, whose limits are chosen so that the trigger is fully efficient over its whole range. The trigger efficiencies as a function of HT3 are however involved because they are not determined by HT3, but by the highest energy jet in the event. As an example, Figure 5.3 shows the trigger turn on as a function of jet E_T, for the Jet_85 trigger [42]. In terms of HT3 this curve gets smeared (Figure 5.5), because two events with equal HT3 can have widely different efficiencies, as illustrated by the following example. Consider an HT3=300 GeV Jet_85 event. If it is a 2-jet event, then E_T =150 GeV (HT3/2), and the efficiency is 100%. On the other hand, if the event has three similar energy jets, then $E_T \sim 100$ GeV (HT3/3), and the event efficiency drops to 10%.

The only way to impose a 100% efficiency requirement on HT3 is by ensuring that all contributing events have their leading jets in the 100% efficiency region. Figure 5.4 illustrates the situation for the Jet_30 and Jet_50 triggers. For the first (second) one the jet energy threshold is 60 GeV (100 GeV), and this requires an HT3 threshold of 160 GeV (260 GeV). It is unfortunate that many 100% efficient events are lost in this procedure (all the events in the upper left quadrant in the Figure), but it is essential to eliminate the contamination from partially understood kinematic regions that would bias our sample. The resulting HT3 threshold values are shown on the respective turn-on plots on Figure 5.5 and presented in Table 5.2.

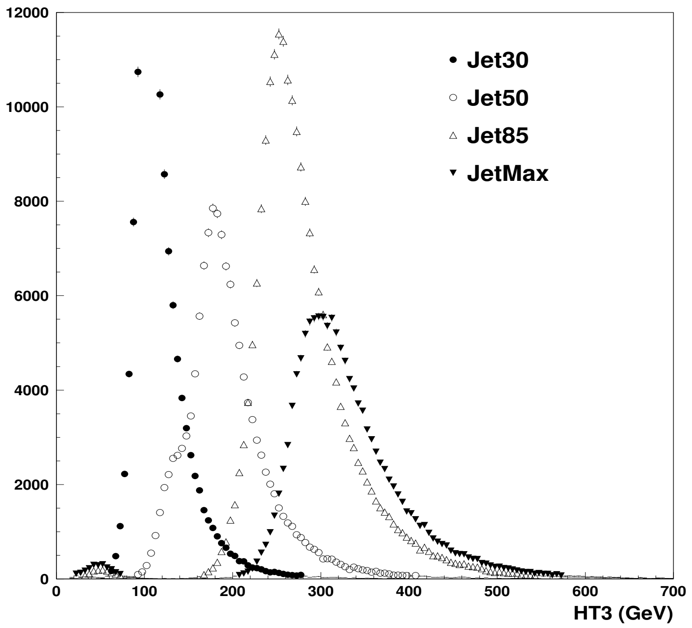

Figure 5.2: HT3 spectrum for various jet triggers.

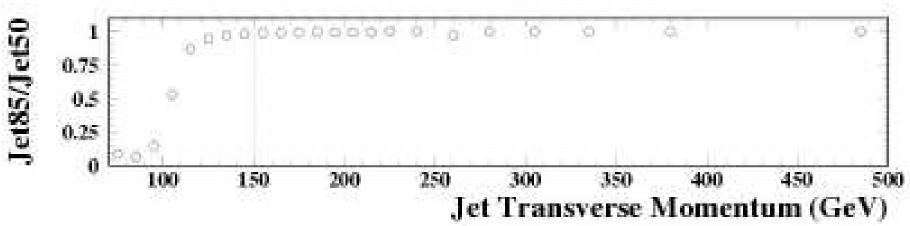

Figure 5.3: Turn on for *Jet_85* . The dashed line shows the threshold from where the trigger is fully efficient.

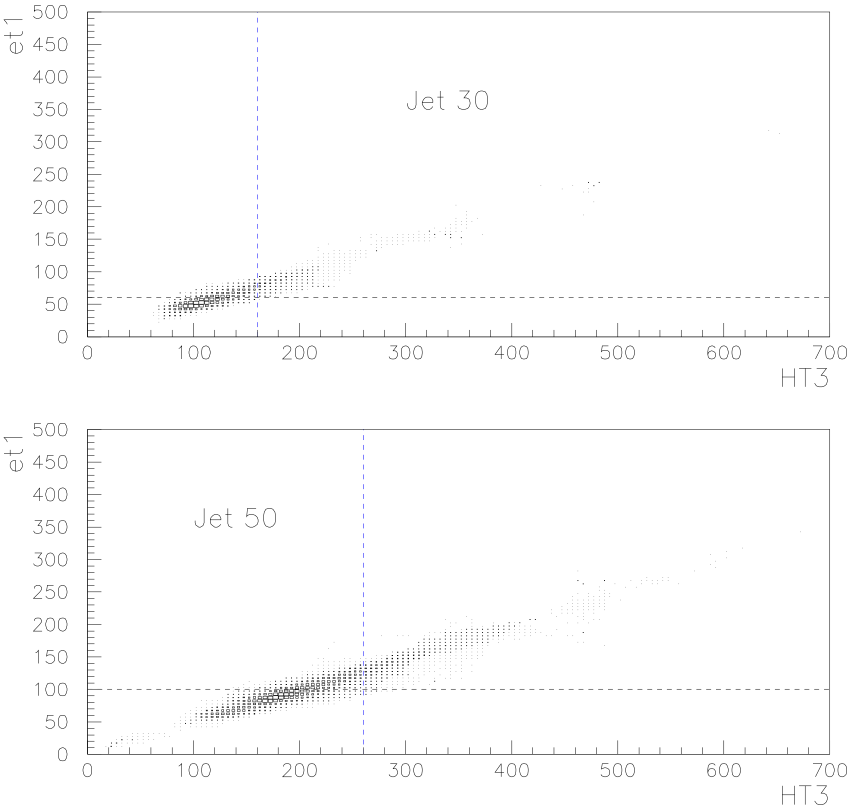

Figure 5.4: Leading jet E_T as a function of HT3, for triggers Jet_30 and Jet_50 . The dashed lines show the threshold from where the triggers are considered to be fully efficient.

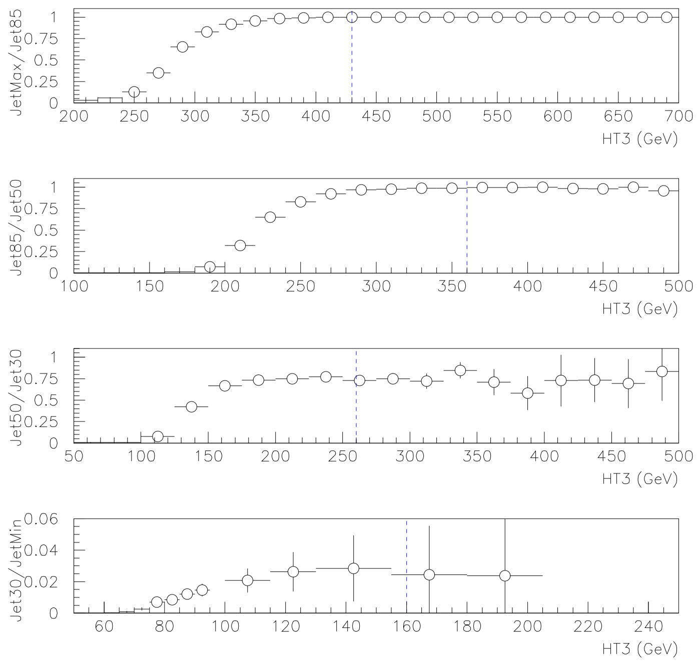

Figure 5.5: Triggers turn on. The dashed lines show the thresholds from where the triggers are fully efficient.

Jet Trigger	HT3 bin (GeV)
Jet_30	$160 - 260$
Jet_50	$260 - 360$
Jet_85	$360 - 430$
Jet_Max	$430 - 700$

Table 5.2: HT3 bin for each trigger. The thresholds were selected by requiring the jet triggers to be fully efficient.

5.7 Luminosity Determination

The integrated luminosity is calculated by summing up measured instantaneous luminosities ($\mathcal{L}$, number of $p\overline{p}$ crossings per second and per cm^2) over a specified period of time. It is determined separately for each trigger to account for individual prescales and dead times. The integrated luminosities for Jet_85 and Jet_Max are extracted from the production database (PDB), based on the run number information (see Table 5.3). Their relative luminosities are cross-checked by fitting a constant to the ratio of their HT3 spectra, as shown on Figure 5.6. The result agrees well with the ratio of the PDB values. Due to discrepancies observed among trigger versions the luminosities for Jet_50 and Jet_30 were not extracted from the PDB. They have instead been measured relative to that of Jet_85, by fitting a constant to the ratio of their respective HT3 spectra.

Final results and errors are shown in Table 5.3. Since there is no information for the DØfixed streams in the production database, it is not possible to obtain the errors accurately [43], thus a conservative value of 8% is assigned to each trigger luminosity. In the cases of jet triggers Jet_50 and Jet_30 the error also includes the uncertainty due to the matching procedure.

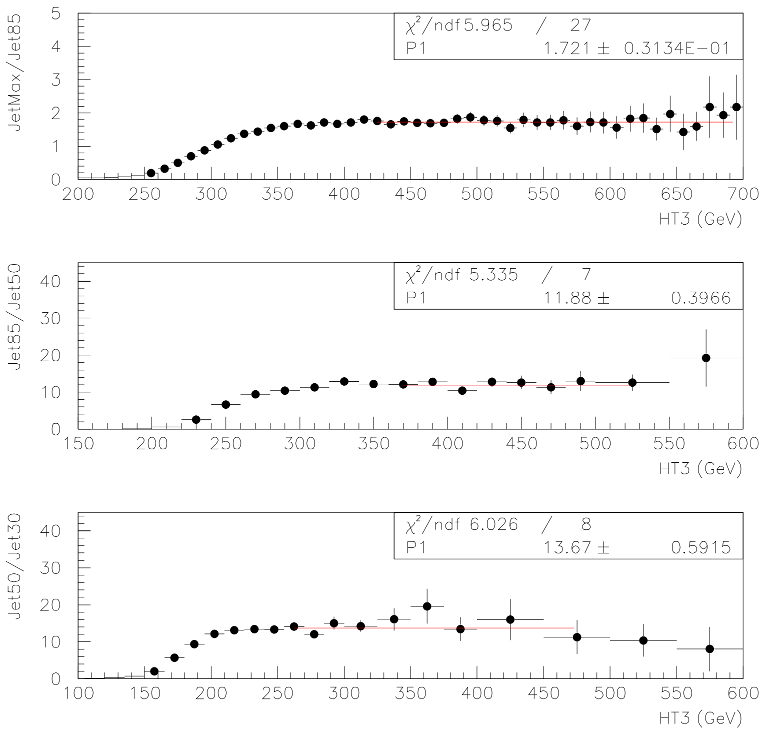

Figure 5.6: Ratio of HT3 spectra, from top to bottom: Jet_Max/Jet_85, Jet_85/Jet_50, Jet_50/Jet_30 .

Jet Trigger	Integrated Luminosity (pb^{-1})	Error (%)
Jet_30	0.34	9.5
Jet_50	4.35	9
Jet_85	51.5	8
Jet_Max	87.3	8

Table 5.3: Integrated Luminosities for each jet trigger.

Chapter 6

Detector Resolutions and Position Bias

The calculation of T_2^t involves three variables per jet: transverse momentum and angular position. Thus, it is essential to determine how this magnitudes are affected by experimental effects (finite detector resolution, noise, multiple interactions, etc) as well as to understand the implication of a change in their values on the thrust itself. This chapter presents the methods used to measure detector resolutions and angular biases and the corresponding results. The impact of these effects on the T_2^t cross sections is studied in the next chapter.

6.1 Energy Resolutions

This section presents the measurement of the transverse momentum resolutions, for jets reconstructed with the $k_\perp$ algorithm (parameter $D = 1$), for various η bins. The procedure applied here follows the one detailed in [42]. It is based on the dijet p_T asymmetry, A, defined as :

$$A = \frac{(p_{T,1} - p_{T,2})}{(p_{T,1} + p_{T,2})} \tag{6.1}$$

where $p_{T,1}$ and $p_{T,2}$ correspond to the transverse momenta of the two leading jets. In dijet events, the deviation from zero of the variable A is a signal of finite detector resolution. Assuming $p_T \equiv (p_{T,1} + p_{T,2})/2 \approx p_{T,2} \approx p_{T,1}$ and $\sigma_{p_{T,1}} = \sigma_{p_{T,2}} = \sigma_{p_T}$ the fractional resolutions can be found as :

$$\frac{\sigma_{p_T}}{p_T} = \sqrt{2}\ \sigma_A \tag{6.2}$$

where σ_A is the standard deviation of the asymmetry distribution. Dijet events were selected from the data sample described in Chapter 5 by applying a back-to-back cut of 5° in azimuth for the two leading jets, which were required to be in the same η region and to pass the jet quality cuts. The asymmetry distributions were considered in bins of average transverse momentum of the two jets and fitted to Gaussians.

There are two systematics effects that produce a finite A not related to resolutions and that need to be accounted for. The presence of low energy jets may prevent the two leading jets to balance on the transverse plane. We have corrected for this by calculating A for different cuts on the third jet p_T and taking the measured fractional resolution to be the value extrapolated to $p_T \to 0$. This value has been corrected by subtracting the fractional p_T resolution due to particle imbalance. This effect reflects the fact that even at the particle level dijet events may not balance due to misclustering (incorrectly assigned, or not assigned, momentum to the jets). To evaluate it, the same procedure applied to data was used on particle level jets from HERWIG MC samples.

Figures 6.1–6.3 show the fractional resolutions for three different η ranges. They have been parametrized as:

$$\frac{\sigma_{p_T}}{p_T} = \sqrt{\frac{N^2}{p_T^2} + \frac{S^2}{p_T} + C^2} \tag{6.3}$$

The resolutions for the range $|\eta| < 0.5$ were already derived for the inclusive jet cross section measurement. Thus, the results are taken from [42].

The total uncertainty combines the statistical error from the fits and the systematic from the particle imbalance correction. In order to determine the accuracy of the asymmetry method a MC closure was performed. The closure is a test done by comparing the resolutions obtained from MC samples following the asymmetry variable procedure and the "straight" one, in which the resolutions are obtained from the p_T ratio of matched jets between calorimeter and particle level. The results were found to be in good agreement within errors. A 0.5% was assigned as a systematic error due to the measurement method.

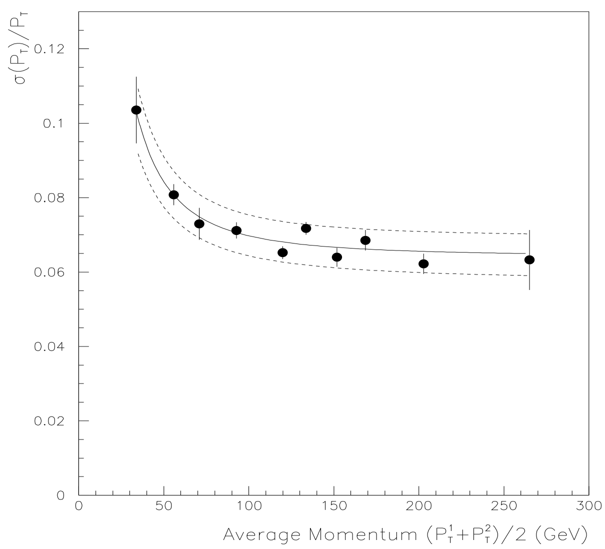

Figure 6.1: P_T Fractional Resolution for $0.5 < |\eta| < 1$

6.2 Position Bias and Resolutions

Due to a combination of factors, such as fluctuations in the evolution of the calorimeter shower, calorimeter response, uranium noise, pile-up and multiple interactions, a mismeasurement of jet position can be produced. In order to determine the angular bias and resolutions, different MC samples have been used. They were generated

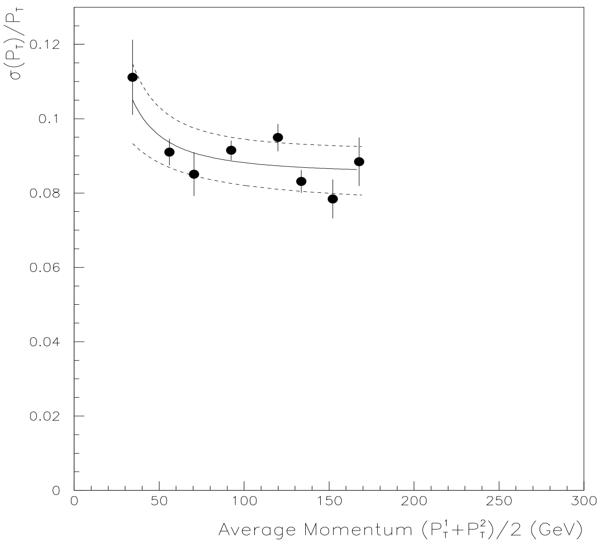

Figure 6.2: P_T Fractional Resolution for $1 < |\eta| < 1.5$

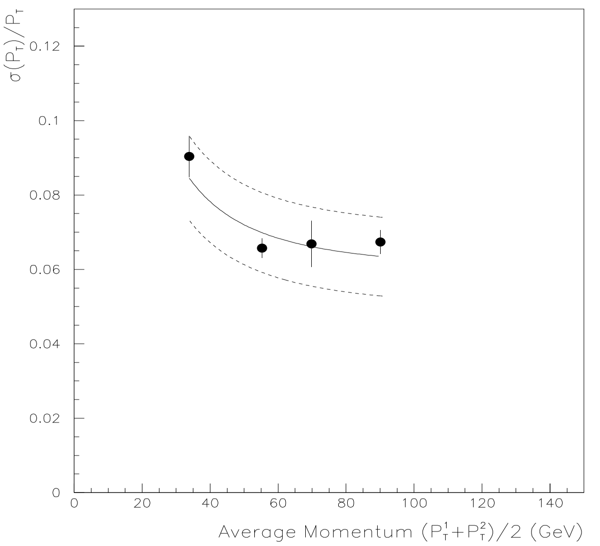

Figure 6.3: P_T Fractional Resolution for $1.5 < |\eta| < 3$

with HERWIG [21], with underlying event turn on, for different parton p_T thresholds and processed through the detector simulation SHOWERLIB [30]. The result was overlayed with zero bias (ZB) data, taken for a range of luminosities ($\mathcal{L}$ = 3,5,19 $\times 10^{-30}\, cm^{-2}\, s^{-1}$) to simulate the effects of pile-up, multiple interactions and noise. Jets were reconstructed with the $k_\perp$ algorithm. This work closely follows the procedure for the determination of biases and resolutions for the cone algorithm [44].

6.2.1 Position Biases

In order to calculate the η bias, jets at calorimeter and particle level were matched requiring $\Delta R < 0.5$ ($\Delta R = \sqrt{\Delta\eta^2 + \Delta\phi^2}$). The bias can be defined as:

$$\eta_d^{ptcl} = \eta_d^{reco} + \delta(E_{jet}^{reco}, \eta_d^{reco}) \tag{6.4}$$

where η_d^{reco} is the reconstructed calorimeter jet η, E_{jet}^{reco} is the energy of the reconstructed jet, η_d^{ptcl} is the η position of the particle jet and δ is the bias calculated as the average of $\eta_d^{ptcl} - \eta_d^{reco}$. The η position is in all cases referred to the center of the detector and indicated as (η_d).

Figure 6.4 shows the bias for five different E_{jet}^{reco} ranges as a function of η_d^{reco}. The shape of the bias can be due to the difference in the calorimeter response as a function of η. The fact that the jets tend to move towards the beam can be explained as a result of the noise effect, since it increases as we approach the beam pipe.

In order to determine the correction, the values have been projected from the negative to the positive side assuming the bias is antisymmetric. The result has been fit for the 4 first E bins with:

$$\delta(E_{jet}^{reco}, \eta_d^{reco}) = A + Bx + Cx^2 + Dx^3 + Ex^4 + Fx^5 \tag{6.5}$$

and for the last bin:

$$\delta(E_{jet}^{reco}, \eta_d^{reco}) = A + Bx + Cx^2 \quad \text{for } |\eta| < 0.85 \tag{6.6}$$

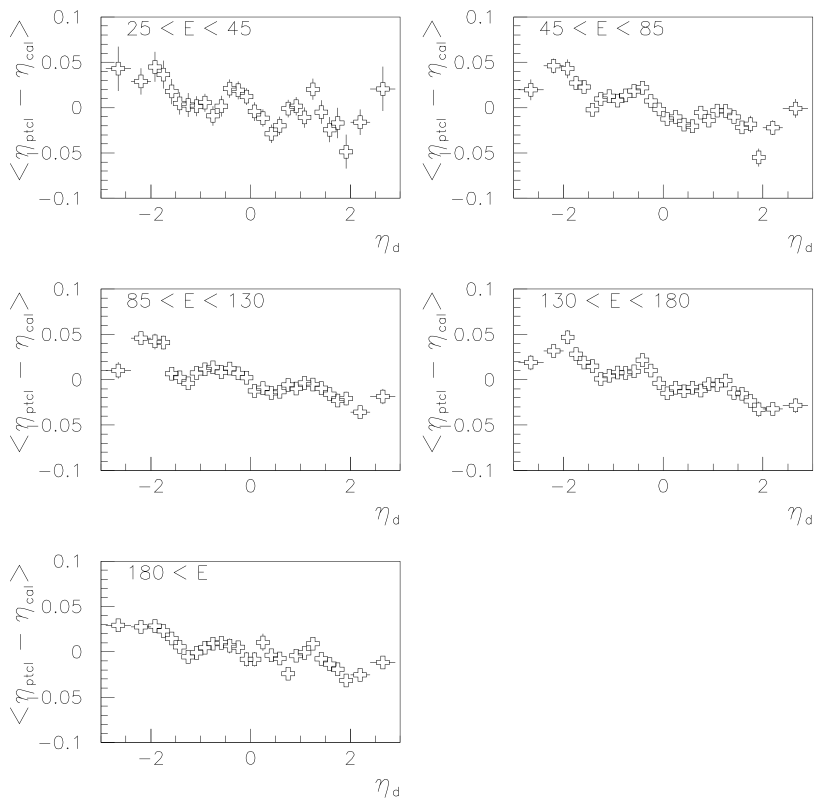

Figure 6.4: η bias for 5 different E bins as a function of η_d, calculated for a MC sample overlayed with ZB taken at $\mathcal{L} = 5$.

and

$$\delta(E_{jet}^{reco}, \eta_d^{reco}) = D + Ex + Fx^2 + Gx^3 \quad \text{for } |\eta| > 0.85 \tag{6.7}$$

As it is shown on Figure 6.5, no distinct η bias is observed after the correction is applied to the reconstructed jets.

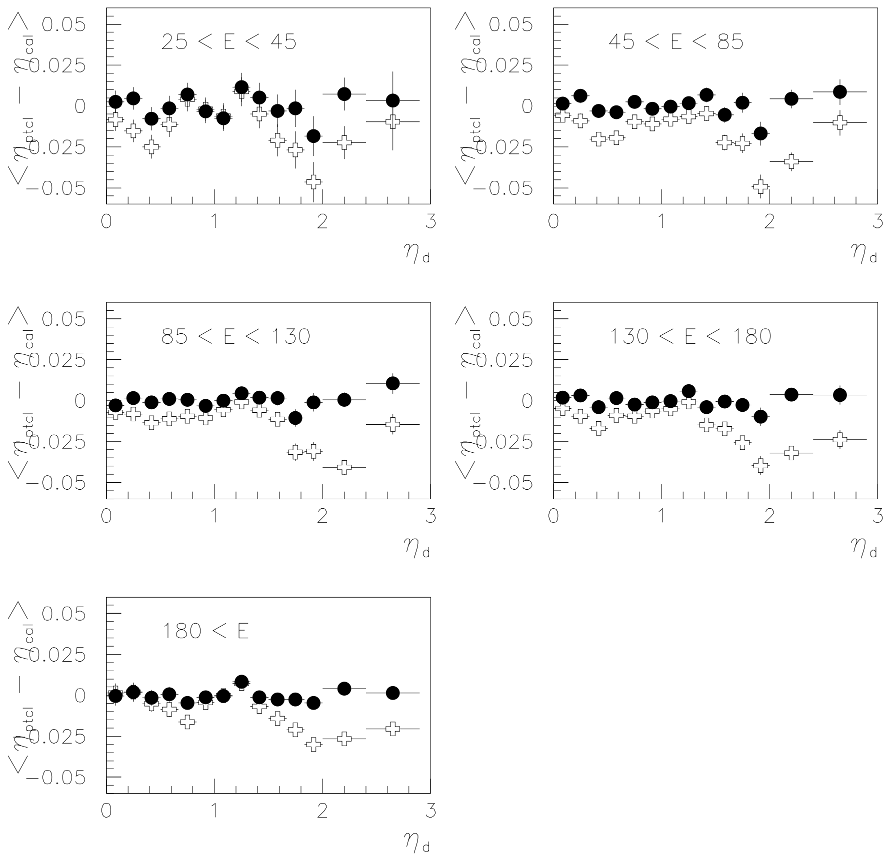

Figure 6.5: η bias before (crosses) and after (circles) the correction is applied.

The dependence of the bias on the luminosity ($\mathcal{L}$) was studied using the MC samples overlayed with ZB data taken at various values of $\mathcal{L}$. Figure 6.6 shows the corresponding results as a function of η_d and also, for comparison, the bias for a sample with no overlay. As it can be seen it is dominated by the effect of noise, pile-up and multiple interactions. The nominal value has been extracted from the fits for $\mathcal{L} = 5$ and the errors calculated as the maximum difference to the fits for $\mathcal{L} = 3$ and $\mathcal{L} = 19$. The final results are shown in Figure 6.7.

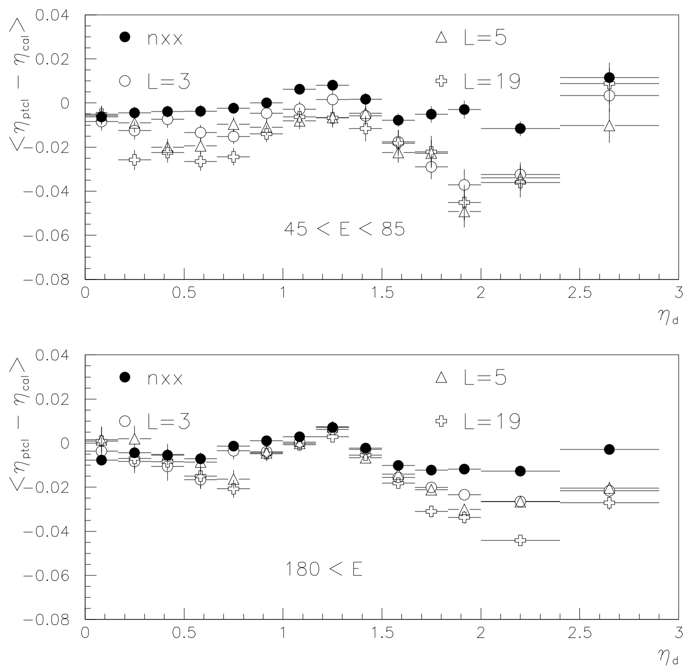

Figure 6.6: η bias for 2 different E bins as a function of η_d, calculated for MC samples overlayed with ZB taken at L=3,5 and 19 and also for a sample without noise overlay (full circles).

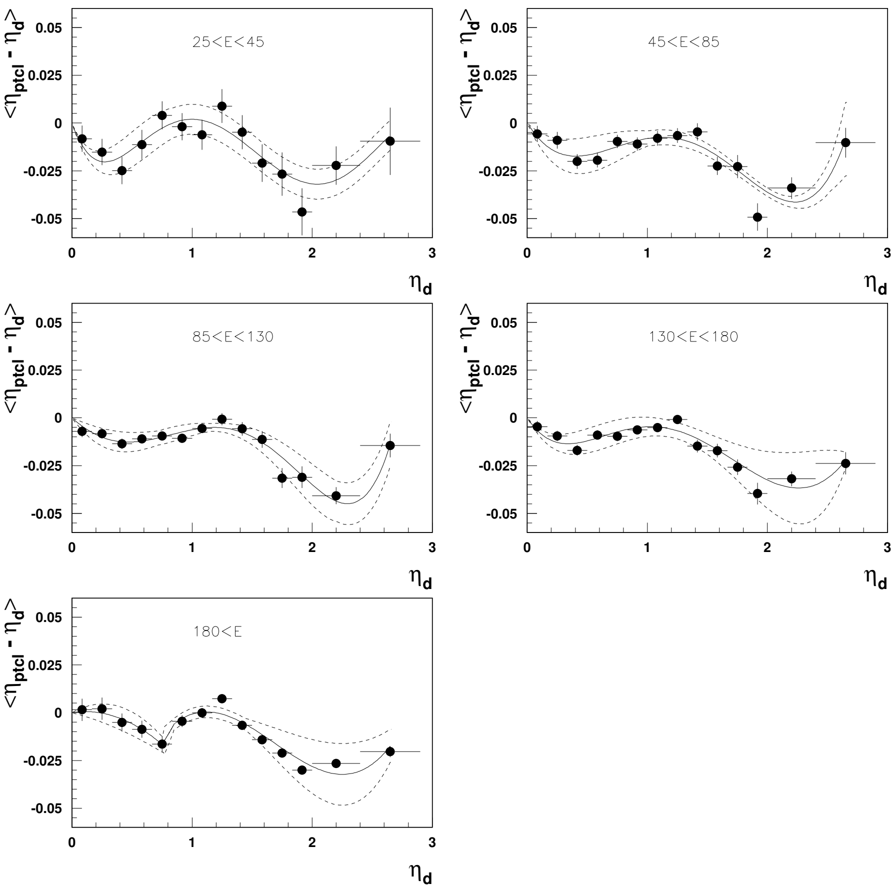

Figure 6.7: η bias for 5 different E bins as a function of η_d, calculated for a MC sample overlayed with ZB taken at L=5. The dotted lines correspond to the systematic errors, which cover the dependence with Luminosity of pile-up and multiple interactions contributions.

6.2.2 Position Resolutions

After correcting the jet positions for the bias, we studied the effects due to the finite calorimeter resolution. The distributions corresponding to $\eta_d^{ptcl} - \eta_d^{reco}$ were fitted with gaussian functions, as illustrated in Figure 6.8, and the standard deviation taken as the jet η resolutions. Five different bins on E_{jet}^{ptcl} have been used for 5 different η ranges, and the results parametrized as:

$$\sigma_\eta(E,\eta) = A + \frac{B}{E} + \frac{C}{E^2} \tag{6.8}$$

This procedure was applied for different luminosities, see Figures 6.9. The nominal values correspond to the results for $\mathcal{L} = 5$ and the errors have been calculated as the maximum difference to the fits corresponding to $\mathcal{L} = 3$ and $\mathcal{L} = 19$. Resolutions decrease at high energies because noise becomes relatively less important while they increase for jets located near the beam pipe where the contamination is larger.

Final results are shown in Figure 6.10.

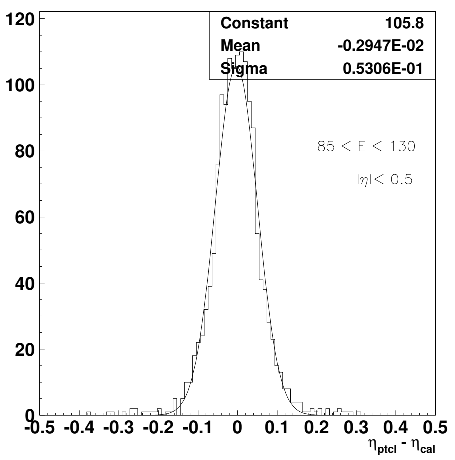

Figure 6.8: Distribution of $\eta_d^{ptcl} - \eta_d^{reco}$ for $|\eta| < 0.5$ and energies between $85 < E < 130$ GeV. The line corresponds to a gaussian fit.

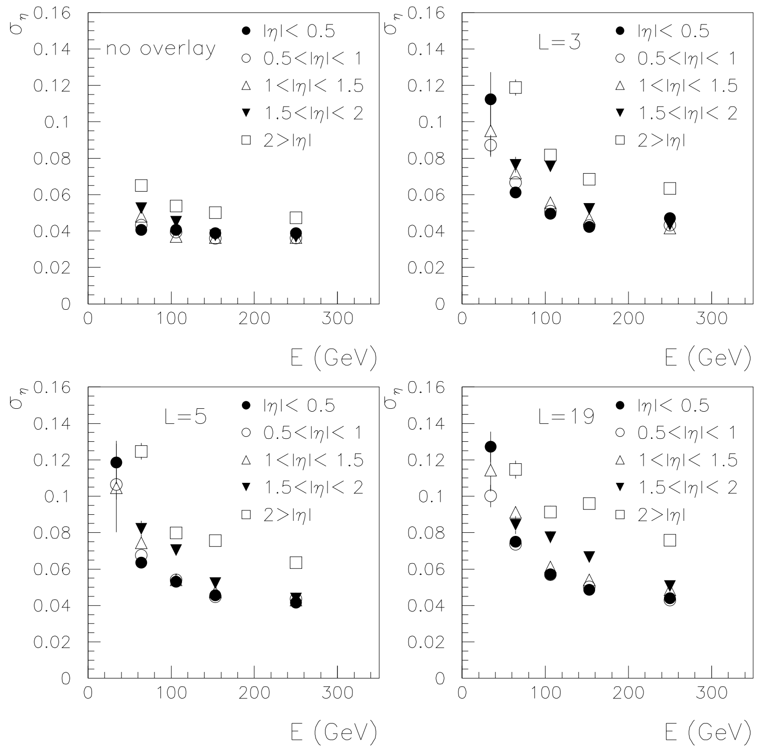

Figure 6.9: η resolution for 5 different η ranges, as a function of E, calculated with MC samples with and without ZB overlay.

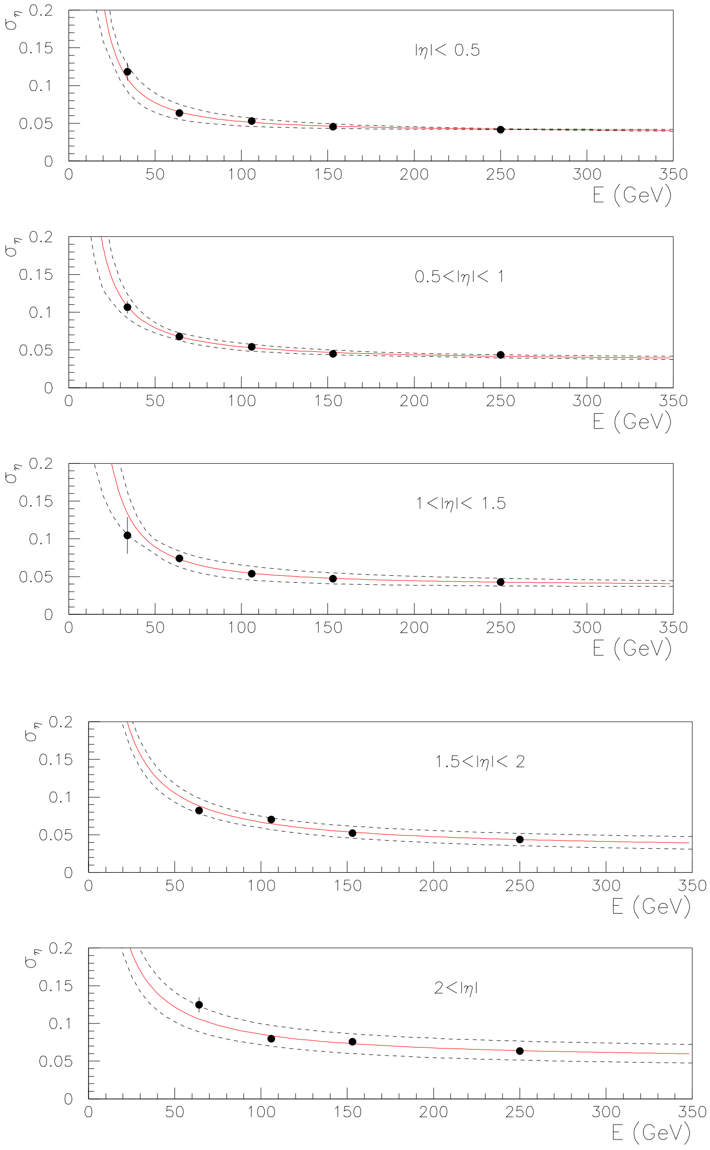

Figure 6.10: η resolution for 5 different η ranges, as a function of E. The points are the results for a MC sample overlayed with $\mathcal{L} = 5$ and the dotted lines correspond to the systematic errors, which cover the Luminosity dependence of effects such as pile-up and multiple interactions.

6.3 ϕ Resolutions from data

The influence of the ϕ resolutions onto the T_2^t cross section are studied in detail in section 7.3.1, where it is shown that they are critical in the $T \to 1$ limit, becoming the dominant effect. Thus, we have measured the resolutions using two different methods. On one side, we have calculated them from the MC with the same method as for η, by plotting the ϕ difference between matched calorimeter and particle jets. In what follows we will refer to this as the "straight method". On the other hand, we have attempted to extract them directly from data, exploiting the fact that in dijet events both jets have to be produced back to back ("dijet method"). Any deviation from $|\phi_1 - \phi_2| = \pi$ should thus be due to angular resolution, once a correction for imbalance due to the presence of a lower energy third jet is accounted for.

The results using the "straight method" are shown in Figures 6.11 and 6.12. The first one presents the resolutions for different luminosities. The nominal value was extracted from the results corresponding to $\mathcal{L} = 5$ and the errors were calculated as the maximum difference to the fits corresponding to $\mathcal{L} = 3$ and $\mathcal{L} = 19$. The final results are shown in the second figure.

In the "dijet method", which closely follows the one used for the E_T resolutions, we plot for several $\langle E_T \rangle = (E_T^1 + E_T^2)/2$ bins the difference between the ϕ position of the leading jets ($\Delta\phi = |\phi_1 - \phi_2| - \pi$) for various cuts on the energy of the third jet as it is exemplified in Figure 6.13.

A straight line is fitted to the variances obtained from these plots, as shown in Figures 6.14–6.15, and the resolutions extracted from a linear extrapolation to zero, using the relation $\sigma_\phi = \sigma_{\Delta\phi}/\sqrt{2}$.

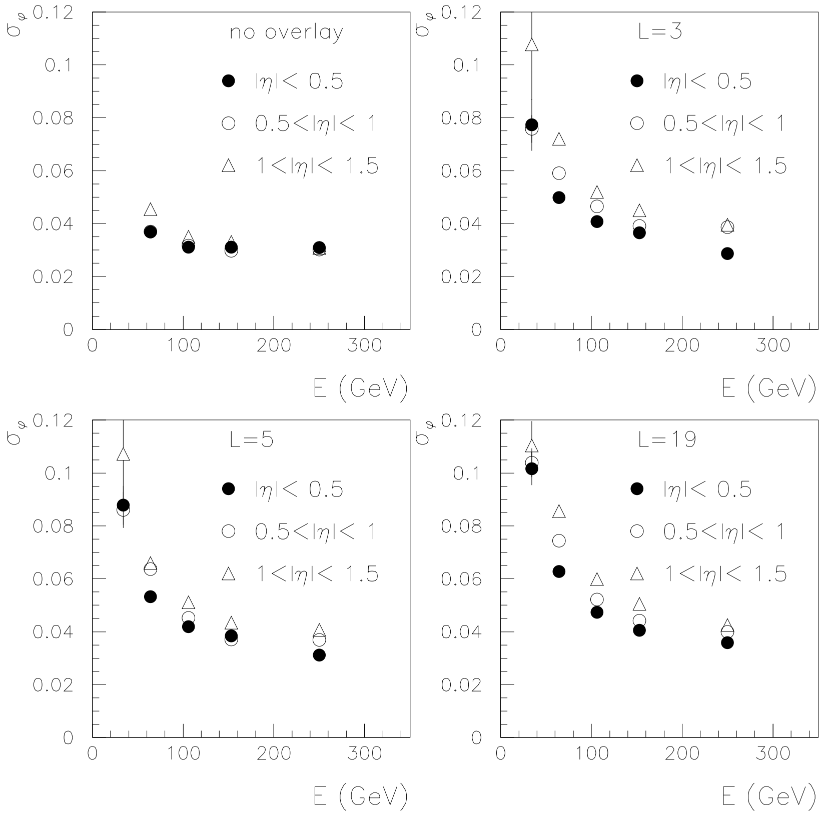

Figure 6.11: ϕ resolution for 3 different η ranges, as a function of E, calculated with MC samples with and without ZB overlay.

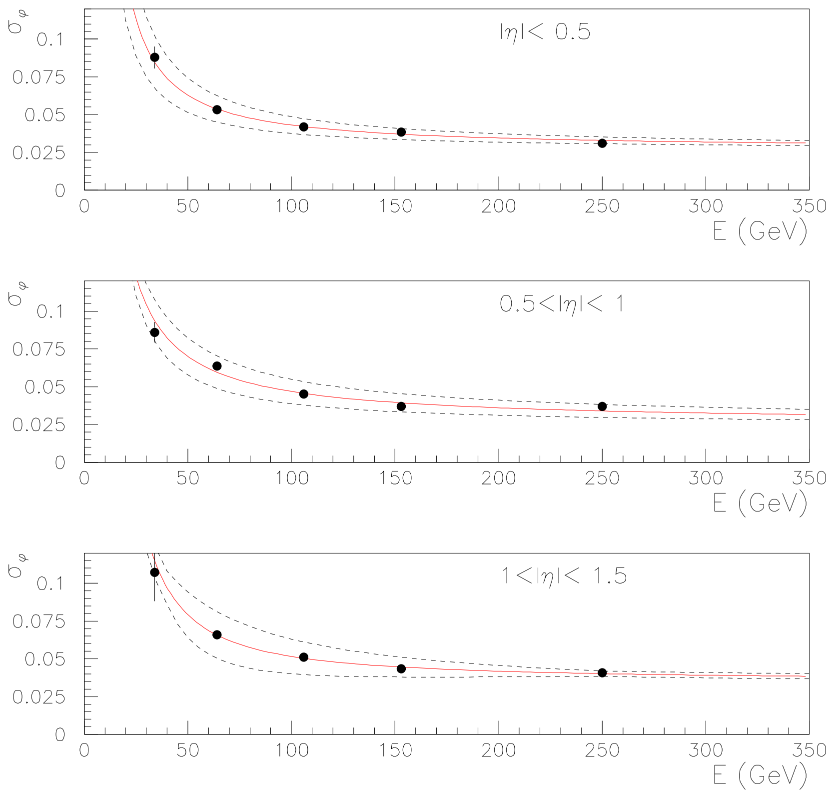

Figure 6.12: ϕ resolution for 3 different η ranges, as a function of E. The points are the results for a MC sample overlayed with $\mathcal{L} = 5$ and the dotted lines correspond to the systematic errors, which cover the Luminosity dependence of effects such as pile-up and multiple interactions.

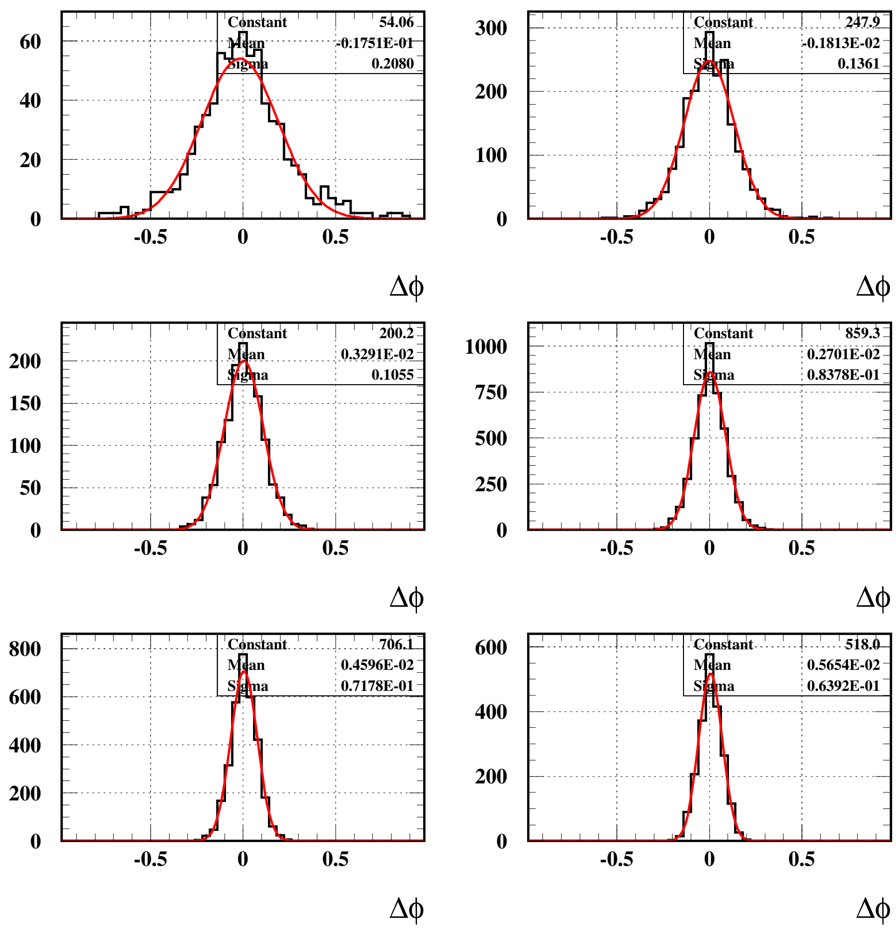

Figure 6.13: Distributions of the difference between the ϕ position of the leading jets for different $\langle E_T \rangle = (E_T^1 + E_T^2)/2$ bins and for events were the third jet is greater that 10 GeV.

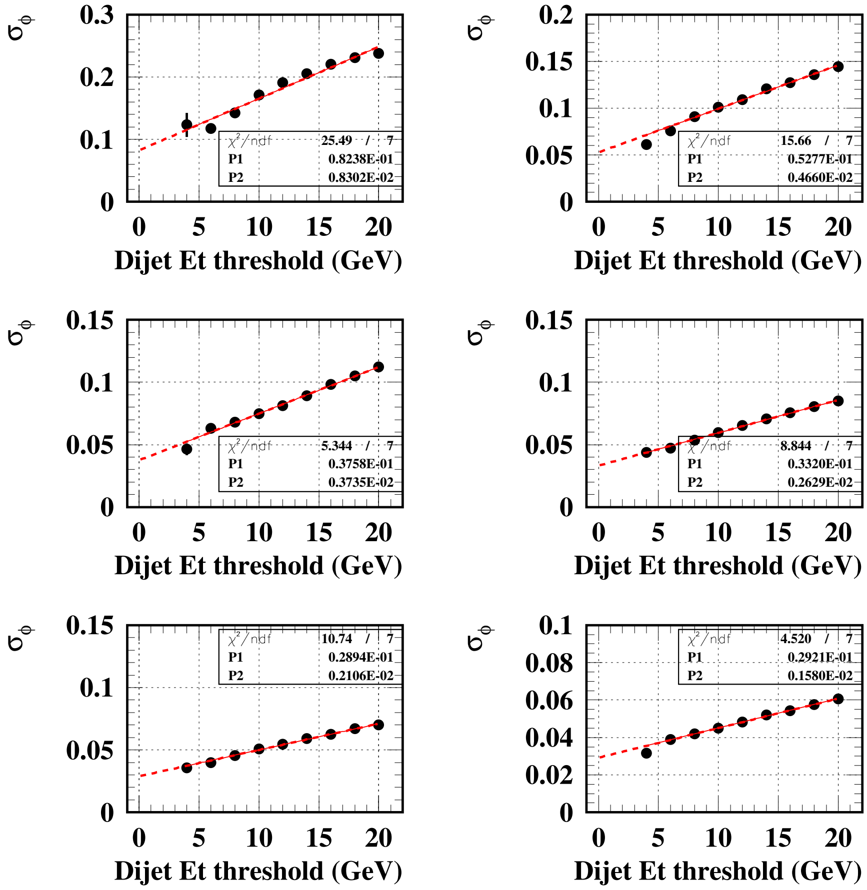

Figure 6.14: σ_ϕ as a function of E_{T_3} threshold in bins of $\langle E_T \rangle$ and for events where the leading jets have $|\eta| < 0.5$

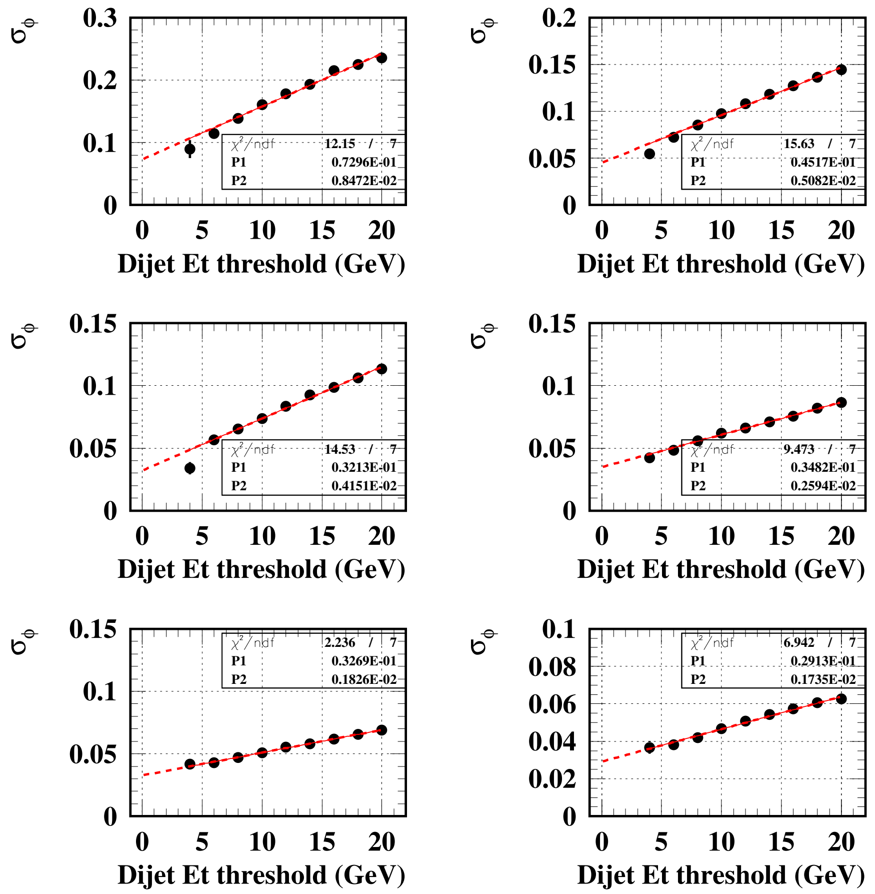

Figure 6.15: σ_ϕ as a function of E_{T_3} threshold in bins of $\langle E_T \rangle$ and for events where the leading jets have $0.5 < |\eta| < 1$

The final results are shown, for two different η ranges of the leading jets in Figures 6.16–6.17 (the contribution of the imbalance at particle level has been subtracted).

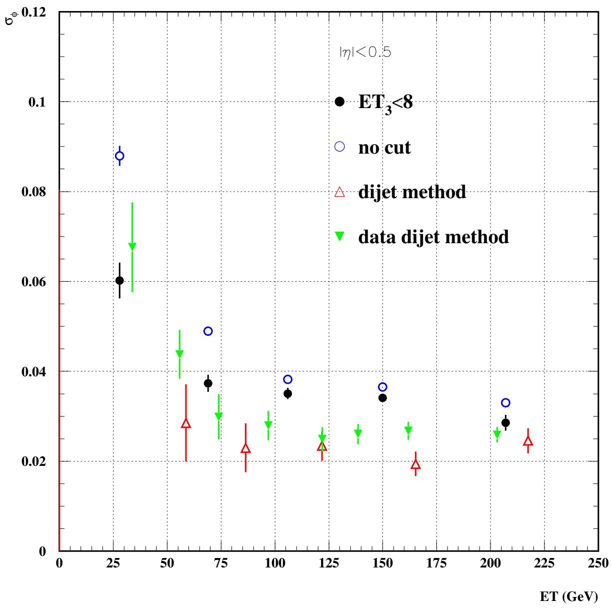

Figure 6.16: The open circles correspond to the MC straight resolutions as a function of E_T, for the full ones $E_{T_3} < 8\,\mathrm{GeV}$ was required. The open triangles correspond to the MC resolutions calculated with the "dijet method" while the full ones are the corresponding results extracted from data.

We find that the MC straight resolutions are higher than those obtained from the data via the dijet method. In order to validate the MC results, we have measured the resolutions by applying the dijet method on the HERWIG samples. As it can be observed in the Figures, the same results are obtained from data and MC. Thus, we are confident that the MC simulation describes well the data. Investigating the source of the difference between MC straight resolutions and data, we found that the straight resolutions are dependent on the cut on the energy of the third jet.

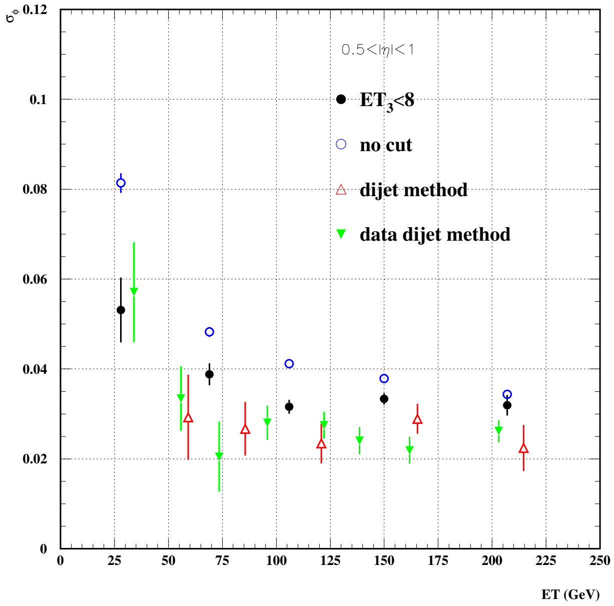

Figure 6.17: The open circles correspond to the MC straight resolutions as a function of E_T, for the full ones $E_{T_3} < 8\,\text{GeV}$ was required. The open triangles correspond to the MC resolutions calculated with the "dijet method" while the full ones are the corresponding results extracted from data.

Resolutions are smaller for a sample where E_{T_3} is required to be less than 8 GeV, indicating that the presence of a high E_T third jet degrades the angular resolution of the leading jets (see Figures 6.16–6.17, full and open circles). As a consequence, the dijet data method turns out to be biased, because it preselects a sample where jets inherently have better resolutions. We conclude that the straight resolutions are the correct ones to use, as they represent the average resolution over the whole sample.

This exercise has proved very useful. The agreement between the results from data and MC using the dijet method is very important and shows that we can trust the results from the MC simulation.

Chapter 7

The measured T_2^t cross sections and systematic errors

The dijet transverse thrust cross section is denoted $d\sigma/dT_2^t$ and it is experimentally determined by:

$$\frac{d\sigma}{dT_2^t} = \frac{N}{\Delta T_2^t \; L \; e_t} \tag{7.1}$$

where N is the number of events in a given ΔT_2^t bin, L is the integrated luminosity and e_t is the total efficiency due to the quality and acceptance cuts (*i.e.*, $e_t = e_{qc}\, e_{met}\, e_{zvtx}$).

We chose to present the results both as a function of $1 - T_2^t$, as this variable ranges between 0 and ~ 0.3, and as a function of $\log(1 - T_2^t)$. The linear scale is best suited to study the cross section over the whole kinematic range, while the logarithm version enhances the high thrust region, allowing a detailed analysis of this zone where most of the statistics resides.

The T_2^t cross sections are measured from the data collected by each of the four inclusive triggers: Jet_30, Jet_50, Jet_85 and Jet_Max. Only one trigger was used for each HT3 bin. HT3, a measure of the energy scale of the event, is defined as the scalar sum of the transverse momenta of the three leading jets.

The T_2^t variable is measured using the two leading jets in the event, requiring $|\eta| < 1$. Since there is no jet momentum scale correction for jets with pseudorapidity greater than 3, in cases where the η of the third jet has $|\eta| > 3$, HT3 is replaced by HT2, the scalar sum of the transverse energy of the two leading jets, as previously discussed in Chapter 4.
Figures 7.1 and 7.2 present the observed T_2^t cross sections, corrected by inefficiencies, jet momentum scale and position bias, in linear and logarithmic scales. Errors are only statistical. The cross section falls steeply with respect to $1 - T_2^t$ and as HT3 increases it shifts towards higher values of thrust.

These cross sections are distorted by the finite resolutions of the detector. The last section of this chapter is devoted to the discussion of the method applied to remove these effects from data. Prior to that, we analyze the sources of systematic errors that affect the T_2^t measurement, which are in general luminosity dependent. As the luminosity increases there is more energy deposited in the detector which can distort the kinematic variables and physical observables. Although each source is studied independently, an overall study of the T_2^t dependence on the luminosity is presented in the next section.

7.1 Consistency Studies: Luminosity Dependence of the T_2^t cross sections

Run 1b data have been taken in a high luminosity environment. The probability of having multiple interactions in a bunch crossing increases with the instantaneous luminosity ($\mathcal{L}$). It is at most 18% for $\mathcal{L}$ less than $5 \times 10^{-30}\, cm^{-2}s^{-1}$ and at least 46% for $\mathcal{L}$ greater than $10 \times 10^{-30}\, cm^{-2}s^{-1}$. Thus, extra energy, which is not related to the hard primary interaction, is deposited in the calorimeter. This affects several of the relevant systematics of this analysis. It increases the amount of energy that

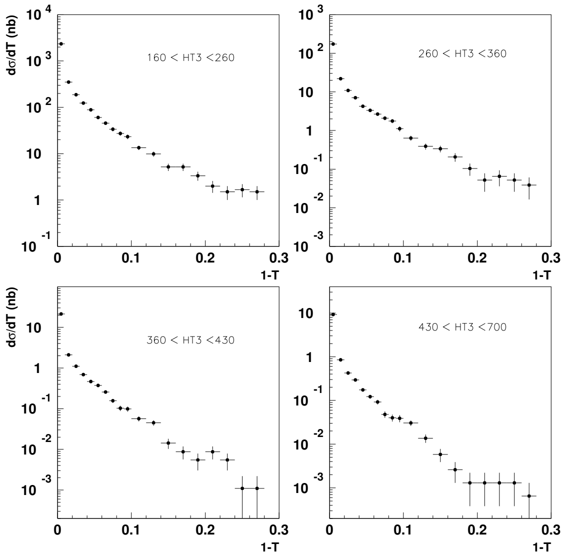

Figure 7.1: T_2^t distributions obtained from Run 1b data, for each HT3 bin.

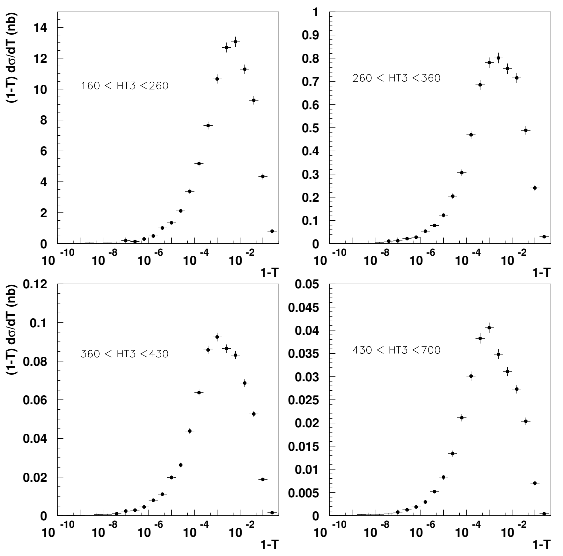

Figure 7.2: T_2^t distributions obtained from Run 1b data, for each HT3 bin. The logarithmic scale enhances the region close to $T_2^t = 1$.

has to be subtracted to each jet (offset correction) and the probability of having background jets (*i.e.*, not related with the hard scattering itself). It can also cause a degradation of the position and energy resolutions. Finally, multiple interactions can produce a mismeasurement of the primary vertex (misvertexing). It is important to notice that the offset correction has been already parametrized as a function of luminosity [32] and that the revertexing procedure is supposed to correct for misvertexing. A luminosity dependence study of the T_2^t cross section allows to find out if any mistake has been done or if additional corrections are needed.

With this purpose, by calculating the average instantaneous luminosity $\mathcal{L}$ for each run, we divided the data sample for each trigger into two subsamples of comparable statistics as it is shown in Table 7.1. The election of two disjoint bands has been done in order to maximize any systematic effect that could be present.

Jet Trigger	$\mathcal{L}$ **range** $(10^{-30}\, cm^{-2} s^{-1})$
Jet_30	$\mathcal{L} < 2$
	$\mathcal{L} > 5$
Jet_50	$\mathcal{L} < 2$
	$\mathcal{L} > 4$
Jet_85	$\mathcal{L} < 4$
	$\mathcal{L} > 6$
Jet_Max	$\mathcal{L} < 4$
	$\mathcal{L} > 9$

Table 7.1: $\mathcal{L}$ range of each subsample for each jet trigger.

The integrated luminosities of each subsample were extracted from the Production Data Base (PDB) and the ratio between the corresponding T_2^t distributions was measured. Since the results from the PDB cannot be fully trusted for subsamples to within less than 10%, a cross-check was done by studying the ratio of the E_T spectra of the leading jet, which is not supposed to be luminosity dependent, as well as for HT3, all of them corrected by inefficiencies and energy scale. The PDB luminosities were adjusted with a multiplicative factor obtained from the E_T ratios which proved to be consistent with a constant fit. The details are presented in appendix B.

Figures 7.3 and 7.4 show the T_2^t distributions corresponding to the different subsamples for two jet triggers. The ratios are consistent with no luminosity dependence (the same occurs for triggers Jet_30 and Jet_85) indicating that the systematic effects are smaller than the statistical uncertainties.

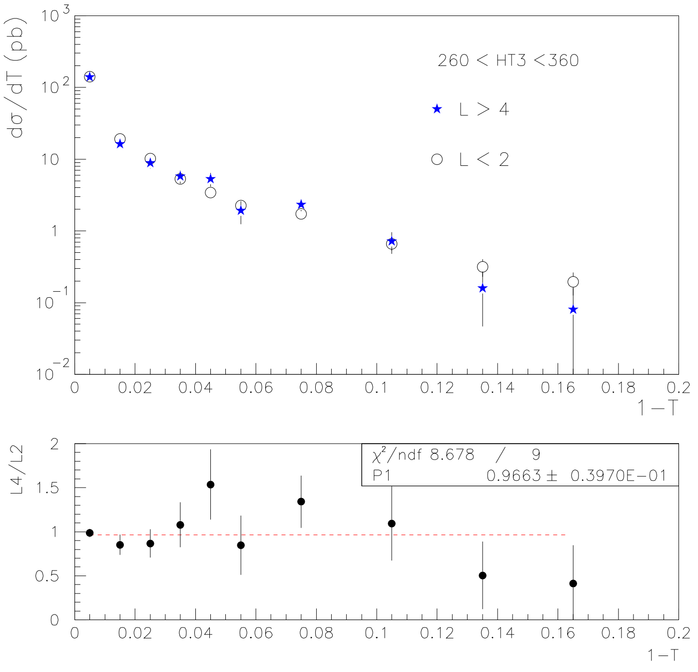

Figure 7.3: T_2^t distributions for two subsamples of Jet_50. The ratio is shown on the bottom plot.

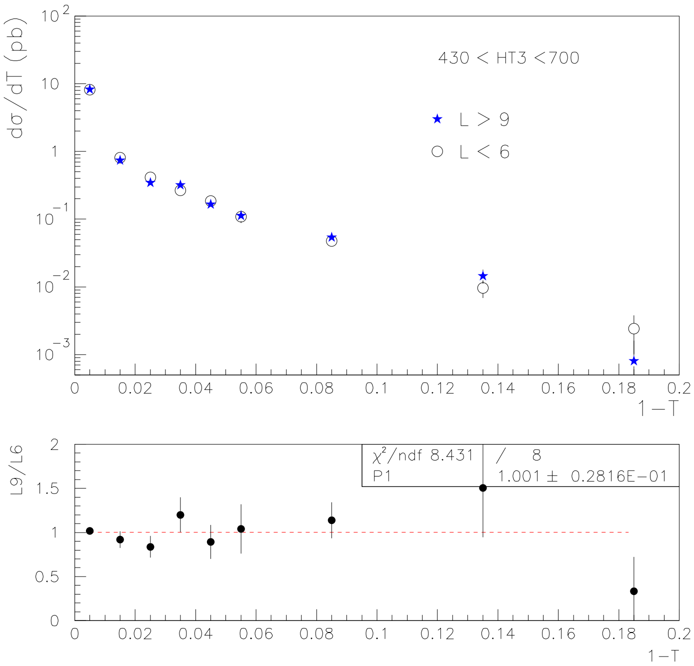

Figure 7.4: T_2^t distributions for two subsamples of Jet_Max. The ratio is shown on the bottom plot.

7.2 Systematic Uncertainties

The different sources of systematic errors, Jet Momentum Scale, Cut Efficiencies, Position Bias and Luminosity uncertainties, have been discussed in detail in previous chapters. In this section we study their contribution to the T_2^t cross sections. We also analyze the error introduced by reconstruction inefficiencies and "noisy" jets (jets from background).

7.2.1 Momentum Scale Correction

As it was mentioned through this work, by applying the momentum scale, the momentum of each jet is restored (in average) back to the particle level. The uncertainty in the Jet Momentum Scale (JMS) propagates to the thrust distribution via two mechanisms. First, the value of T_2^t of each event changes as the energies of the jets are corrected. Second, the value of HT3 is itself affected, resulting in a net flux of events in and out of each of the four HT3 bins. We have investigated the relative importance of these two effects and concluded that the second one is the dominant. This was to be expected due to the definition of the variable where the two jets involved have similar momenta and in the ratio the correction almost cancels. The systematic effect via HT3 is illustrated in the top plot in Figure 7.5 which shows the T_2^t cross sections obtained using the nominal JMS correction for the thrust and the high and low ones for HT3. The high (low) corrected momentum is defined as the nominal momentum plus (minus) $1\,\sigma$, where σ is the error of the JMS correction. A net effect is observed, fully correlated from bin to bin, which is interpreted as a uniform loss of 20% of the events when going from the high to the low correction. This is to be expected, given that the cross section is a steeply falling function of HT3, and the JMS increases the measured jet energies. We thus see that the Jet Momentum Scale systematic error amounts basically to a global normalization uncertainty, and it does not affect the shape of the distributions. The errors for each bin of HT3, calculated as the ratio between the high(low) and the nominal distribution (see the bottom plot of Figure 7.5), range between 10 and 25%.

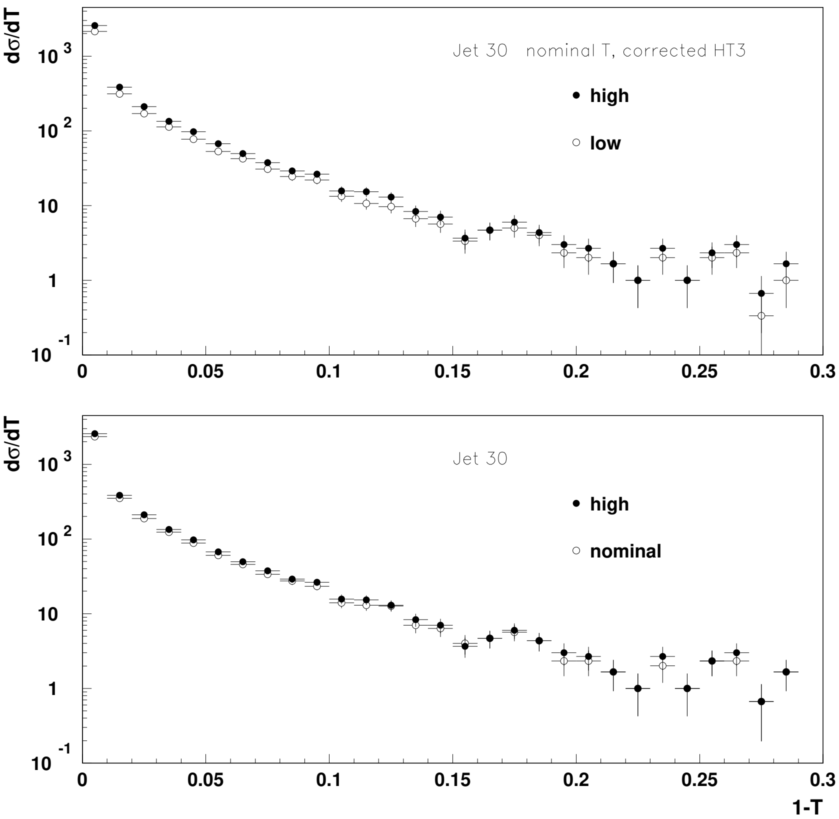

Figure 7.5: Top: The full circles correspond to the nominal corrected T_2^t distribution binned in terms of an HT3 calculated by applying the high momentum scale correction instead of the nominal one. For the open circles the low correction was used. Bottom: T_2^t cross section where the nominal (open circles) and the high (full circles) JMS correction was applied for both T_2^t and HT3.

7.2.2 Low energy jets

Many of the third jets which contribute to the HT3 calculation are low E_T jets, having a high probability of being produced by noise. On the other hand, the reconstruction efficiency at low E_T is not 100%. We studied both issues by matching calorimeter and particle jets in a HERWIG MC sample overlayed with Zero Bias events taken at the average luminosity of our data sample, $\mathcal{L} = 5$.

The top plot in Figure 7.6 illustrates the distribution of unmatched calorimeter jets showing that more than 95% of them are below 10 GeV. We have thus estimated a lower error band by assuming that all jets with $E_T < 10$ GeV are noise jets, which amounts to replacing HT3 by HT2 for those events where $E_{T_3} < 10$ GeV.

The bottom plot in Figure 7.6 illustrates the distribution of unmatched third particle jet, where the jet was required to be separated from the leading ones, in η–ϕ space, by $\Delta R > 2$. In this way the jet is isolated avoiding the possibility of not finding a matching calorimeter jet due to merging with the leading ones. The spectrum indicates that the reconstruction efficiency above 10 GeV is basically 100%. The upper error band is thus (over)estimated by assuming the existence of an unreconstructed 10 GeV jet in all events that do not have a third jet above that threshold. This amounts to replacing the calculation of HT3 by HT2 +10 GeV when $E_{T_3} < 10$ GeV.

Both effects, noise jets and reconstruction inefficiencies, contribute basically in the region of high T_2^t values, where the events usually have a low E_T third jet. The size of the error band varies from 2 to 7% depending on the HT3 bin, as seen in Figure 7.7. It is considerably smaller than major systematic sources, like the Jet Momentum Scale.

7.2.3 Cut efficiencies

In Chapter 5 we described the quality and acceptance cuts events and jets have to pass in order to be included in the sample. Since each of these cuts eliminates some

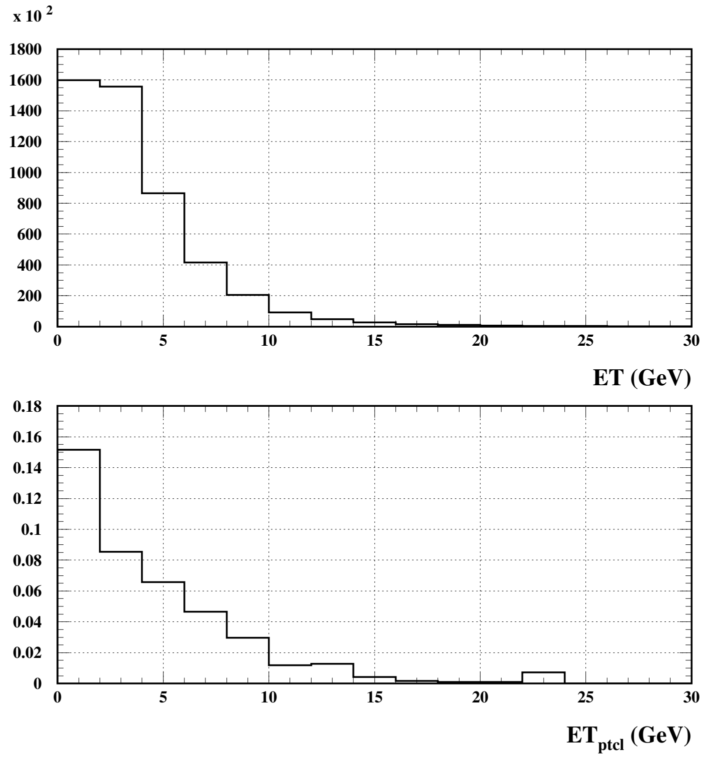

Figure 7.6: Top: E_T spectrum of unmatched calorimeter jets showing that more than 95% of noise jets have $E_T < 10$ GeV. Bottom: Fractional number of unmatched particle jets, indicating that the reconstruction efficiency is basically 100% for $E_T > 10$ GeV.

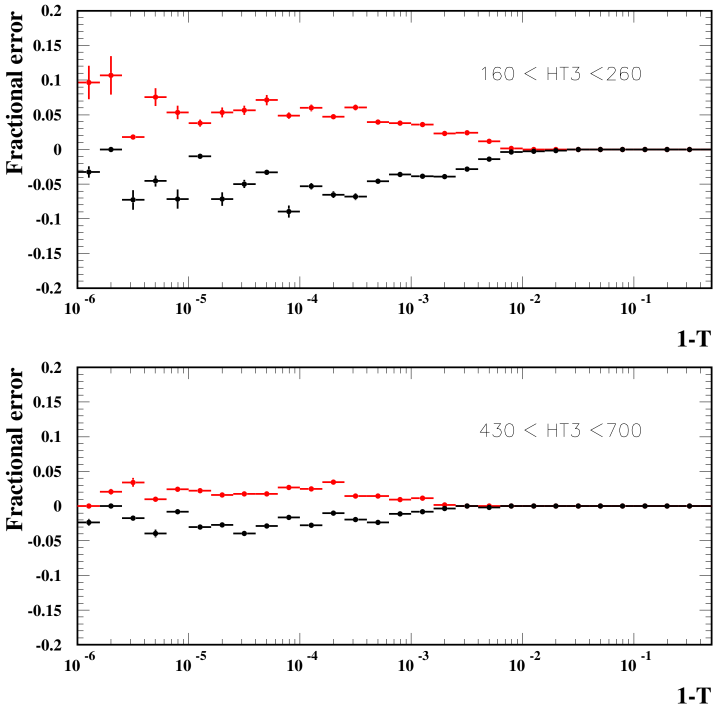

Figure 7.7: Fractional error which accounts for the probability of low E_T jets of being contamination and for the fact that the reconstruction efficiency is not 100%.

good events/jets, an efficiency was included in Eq. 7.1 to account for this effect. The method to calculate these efficiencies carries an uncertainty which translates into an error in the T_2^t distribution. The contributions related with the vertex and the missing E_T cuts are negligible. Thus, the major cut uncertainty comes from e_{qc}. We made a conservative estimation of the error based on results obtained for the inclusive jet cross section [40]. By assuming a 2% error for each e_{qc_i}, and that they are not correlated from jet to jet, the uncertainty of e_t corresponds to 3.5%.

7.2.4 Position Biases

The calculation of the η bias is detailed in chapter 6. In this section we study the effect of the bias on T_2^t. We have calculated the difference between the distribution for which the jet position has been corrected and the uncorrected one. As it is shown in Figure 7.8, this difference is in general less than 2%. The increment on the total number of events occurs because a larger fraction of two leading jets pass the kinematic cuts. The error bars correspond to the difference between the distribution where the low/high correction has been used and the nominal corrected one. This error translates to an uncertainty of less than 2% on the Thrust.

7.3 Detector Resolution Effects and Unfolding

7.3.1 Detector Resolution Effects

The detector has both finite position and energy resolutions. In this section we study how they distort the measurement of the T_2^t cross section.

Energy Resolution

In order to understand how they affect a jet, consider a sample of monoenergetic jets of energy E_0 entering the calorimeter. The energies measured by the detector will be different than E_0 because of fluctuations in the energy detection process and

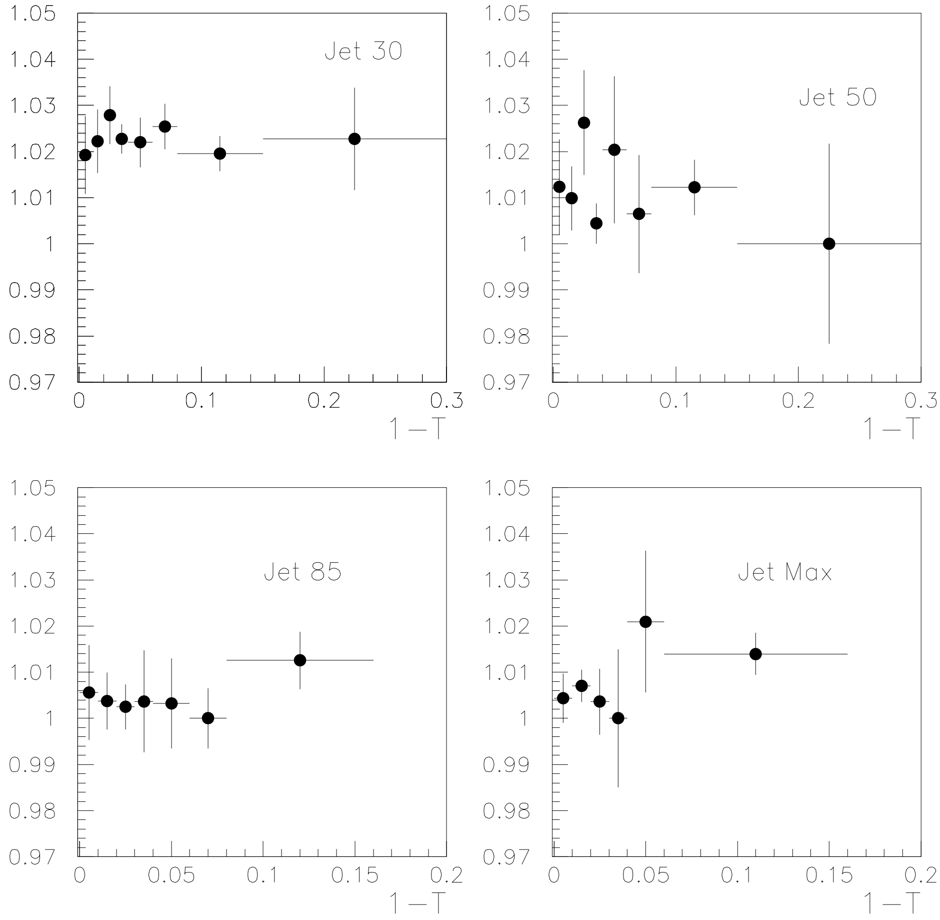

Figure 7.8: Ratio between position bias corrected T_2^t distribution and the uncorrected one. The errors correspond to the difference between the distribution corrected with the nominal biases and the high and low ones.

in the particle showers development. In the DØ calorimeter the measured energy will be "smeared" around the true value, E_0, by a Gaussian (because of the hermeticity and linearity of the DØ calorimeters) with a finite width. Since the HT3 spectrum is a falling distribution in the ranges where T_2^t is measured, the smearing will result in more events migrating to higher HT3 values than vise versa (see Figure 7.9).

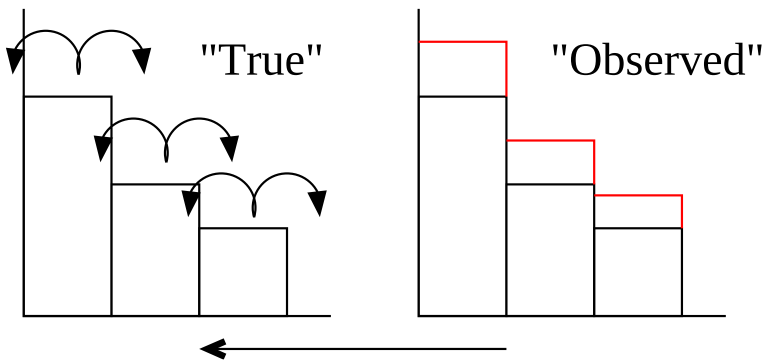

Figure 7.9: Cartoon of the effects of the energy resolutions onto the HT3 distribution. More events migrate from lower to higher HT3 bin due to its falling distribution.

The effects of the energy resolution onto the T_2^t cross section were studied by smearing with a Gaussian function the transverse energy of a sample of HERWIG particle level jets. The width of the gaussian corresponds to the resolutions derived in chapter 6. Figure 7.10 shows the comparison between the particle level T_2^t distributions with and without E_T resolution smearing.

Although the changes on the transverse momentum of the jets could affect the T_2^t value itself (principally if a swap in the E_T ordering is produced), the small differences observed in Figure 7.10, of around 5%, are mostly due to the migration of events from HT3 bins, as explained above.

Position Resolutions

In the case of the η resolutions, the smearing process would affect T_2^t by changing the number of events that pass the η requirements. Since the resolutions are small

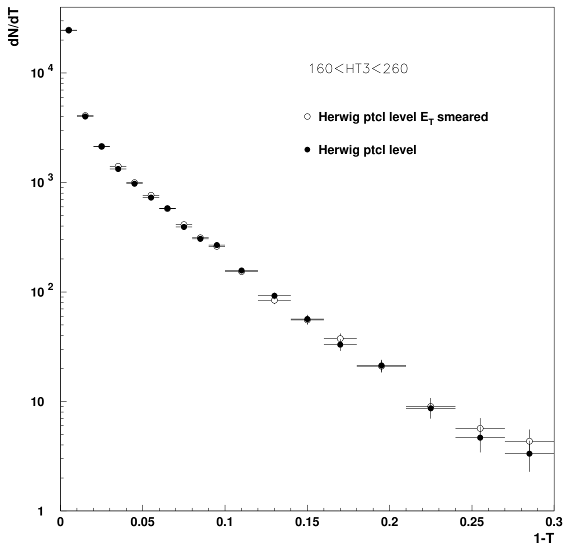

Figure 7.10: The full circles correspond to the particle level distribution. For the open ones the events have been smeared by E_T resolutions.

and the position is smeared randomly, the effect is negligible, as it can be observed in Figure 7.11.

With respect to the ϕ resolutions, the smearing will produce a migration of events between T_2^t bins. This effect is important for T_2^t close to 1 where events move from very high T_2^t bins to lower ones. Consider for example two jets in a back-to-back configuration. If their relative position is modified from $\Delta\phi = \pi$ to $\Delta\phi = \pi - \delta$ taking for example $\delta = 0.04$, a value of the order of the ϕ resolutions, the thrust value changes from 1 to $1 - T_2^t = 2\,10^{-4}$. This is illustrated in Figure 7.12. Events which pass the HT3 cut have been smeared by ϕ resolutions and a profile plot was done as a function of $1 - T_2^t$ (unsmeared). The spread in the high T_2^t bins indicates that we cannot measured the cross section below 10^{-4}. We can only provide an upper limit. Also new bins need to be defined when T_2^t is close to that value, otherwise big uncertainties will result.

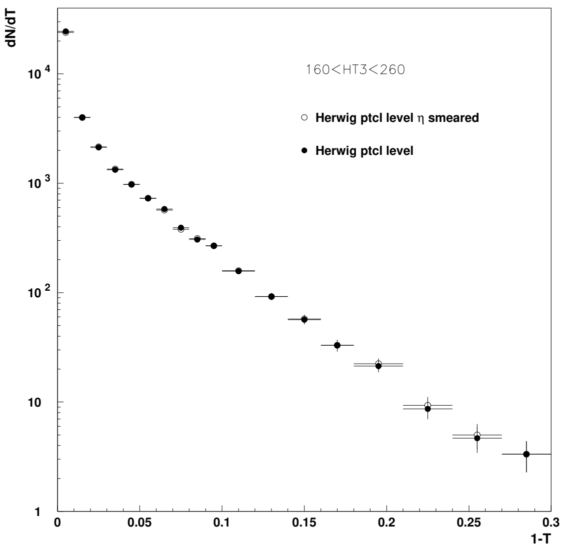

Figure 7.11: The full circles correspond to the particle level distribution. For the open ones the events have been smeared by η resolutions.

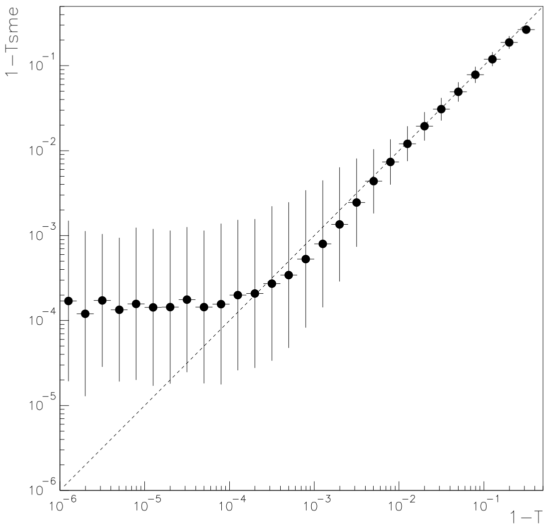

Figure 7.12: Profile plot of the smeared $1 - T_2^t$ as a function of the unsmeared one (calculated with a Herwig particle level distribution), for the lowest HT3 bin.

7.3.2 Unsmearing

In order to compare the experimental results with theoretical predictions, detector resolutions effects have to be either included in the theory (*i.e.*, to "smear" the theory) or removed from the data ("unsmearing"). The option of smearing the theory was ruled out due to its break down when $T_2^t \to 1$, discussed in section 1.5. Furthermore, unsmearing the data yields a true physical measurement, which can be compared to any theoretical prediction. A method which has been often applied at DØ, consists on accepting the hypothesis that it exists a "true" distribution of the variable under study which can be approximated by an ansatz function. By smearing the E_T with a gaussian of width equal to the jet momentum resolution, (in our case, the ones obtained in chapter 6), the resulting function should describe well the observed data. Finally, the unsmearing correction is obtained by taking bin–by–bin the ratio between the original hypothesis and the smeared function. This ratios are called unsmearing factors [39].

In order to unsmear the T_2^t cross sections, we have applied a procedure based on the method described above. However, to free ourselves from any functional form we have implemented the method of the "unbiased binned correction factors" [45]. Instead of selecting a particular function, we chose to use the MC particle level T_2^t distributions as an ansatz, which we will show that once they are smeared, they agree with data. The next sections are devoted to describe in detail this unsmearing method.

7.3.2.1 Comparisons between MC and Data distributions

In order to be able to use the MC particle level T_2^t distributions as an ansatz, it has to be shown that they correctly describe the experimental cross sections once they are smeared by position and energy resolutions. We have compared the measured T_2^t cross sections with HERWIG particle level T_2^t distributions, smeared by E_T , ϕ

and η resolutions, and normalized to data. As it can be seen in the top plots on Figures 7.13 and 7.14, there is a good agreement over almost the whole T_2^t range, except at low values of the variable. In these regions, we reweighted the MC events, by a factor calculated as the ratio Data/MC, using an iterative process. The result can be observed in the bottom plots on Figures 7.13 and 7.14.

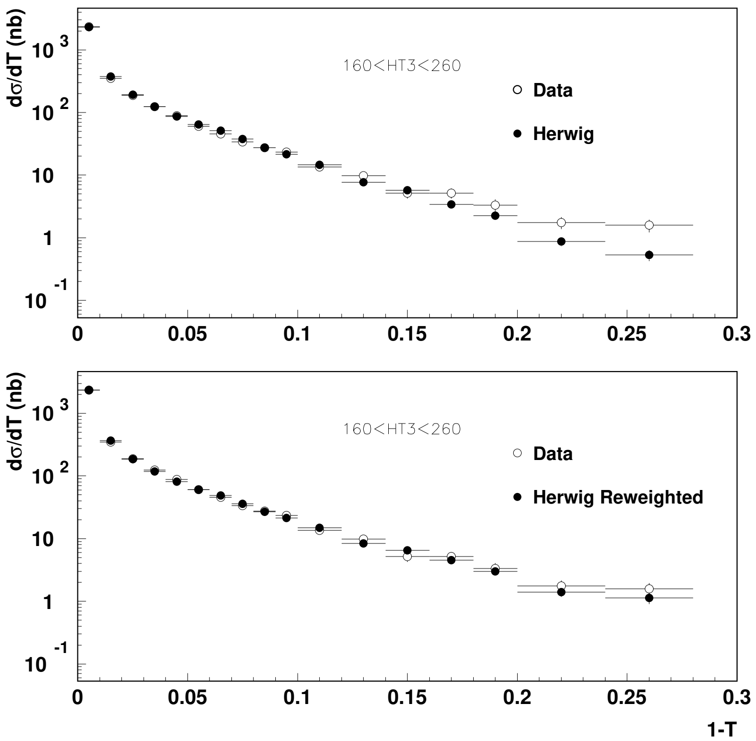

Figure 7.13: Top: Data comparison with Herwig particle level distributions smeared by E_T , η and ϕ resolutions for the lowest HT3 bin. Bottom: MC events have been reweighted in order to make the smeared distribution agree with data.

7.3.2.2 Correction Factors

Having shown that the MC reweighted T_2^t distributions can be used as an ansatz, the correction factors, for each T_2^t bin, were obtained as the ratio between the unsmeared and smeared MC distributions. The results are presented in Figure 7.15–7.16 for a

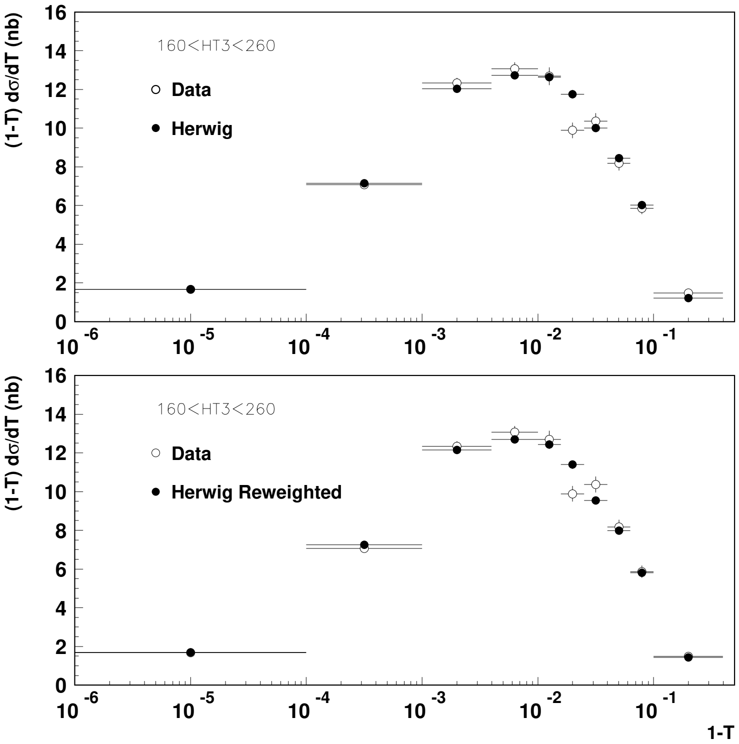

Figure 7.14: Top: Data comparison with the Herwig particle level distribution smeared by E_T , η and ϕ resolutions for the lowest HT3 bin. Bottom: MC events have been reweighted in order to make the smeared distribution agree with data.

linear and logarithmic $1-T_2^t$ scale. The correction is extracted point to point except in the regions shown in the Figures, where fits have been done to smooth out the statistical fluctuations. In linear scale the correction is dominated by the smearing due to the E_T finite resolution which, as we have mentioned, is around 5%. The ϕ resolutions affect basically only the first bins by moving events from higher to lower T_2^t values, canceling partially the effect of the E_T smearing for the first bin and enhancing it in the second one. In the logarithmic scale the main effect is the migration of events due to the ϕ resolutions. At very high T_2^t values, the correction is greater than one since the smeared distribution loses events in these bins, which move to lower T_2^t ones. Thus, the correction in these bins is less than one, by almost 20%. As T_2^t decreases the effect of ϕ resolutions is less important because bins are larger and there is very little migration from one bin to another. The remaining effect is due to E_T resolutions.

Systematic Errors

The effect of the ϕ resolutions is so important in the $T_2^t \to 1$ limit, that large variations in the shape of the proposed ansatz could result, after smearing, in a distribution that also agrees with data within errors. Thus, since we do not know to what extent HERWIG simulates the actual thrust cross section, we introduce an error to take proper account of the uncertainty on the ansatz. With this purpose we developed the following method. We have allowed the number of generated events in each of the ten bins of the logarithmic plot to vary freely, under the constraint that, within errors, the respective smeared distributions agree with the data. This is implemented by assigning a weight $(1+y_i)$ to the events in each bin, where $\{y_i = 0\}$ corresponds to the nominal HERWIG distribution shown in Figure 7.14 (bottom plot). For each set $\{y_i\}$ the corresponding smeared distribution is obtained and the χ^2 difference to the nominal distribution computed. We find that $\chi^2(y_1, y_2, ..., y_N)$

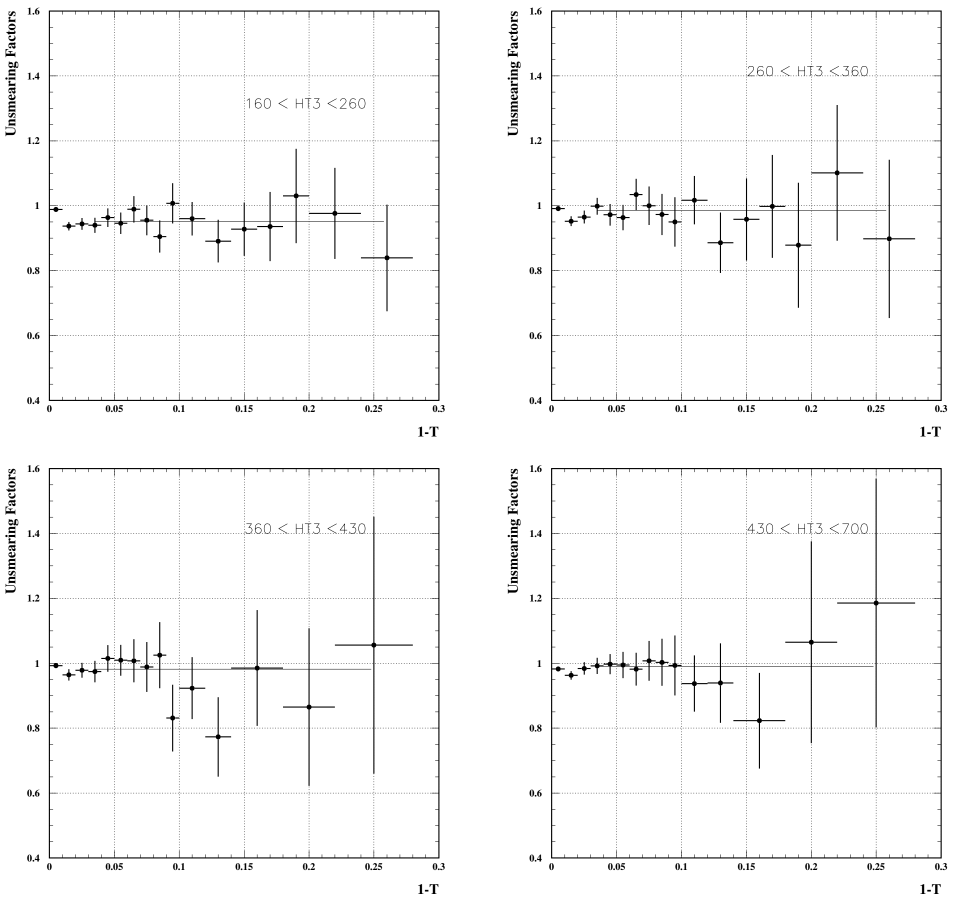

Figure 7.15: Unsmearing factors as a function of 1-T. The bars are the statistical errors. The correction has been extracted from the points up to 1-T=0.04 (this is the region where most of the statistics resides). From there, in order to smooth out the curve, the points are fitted with a constant function.

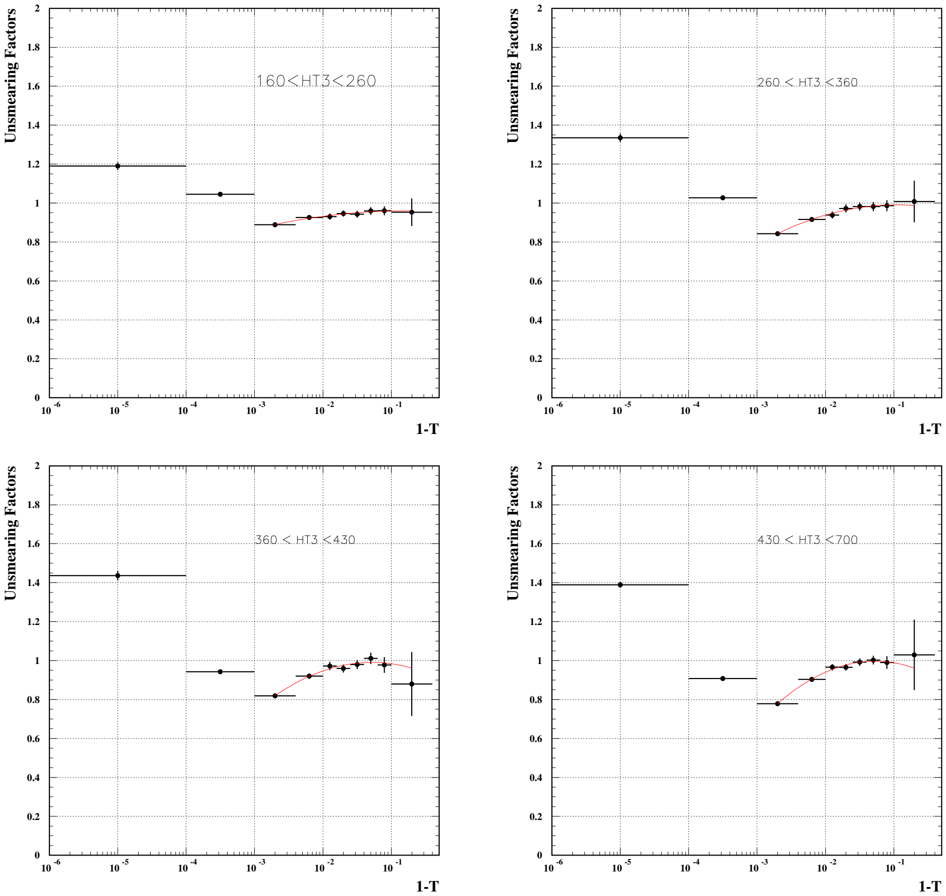

Figure 7.16: Unsmearing factors as a function of 1-T. The bars are the statistical errors. A fit has been done to smooth out statistical fluctuations.

has a N-variable paraboloid dependence around χ^2_{min} (see Figure 7.17), where the quadratic coefficients correspond to the inverse of the covariance matrix on the coefficients $\{y_i\}$ that parametrize the arbitrary shape of the ansatz function:

$$\chi^2(y) = \chi^2_{min} + (y - \hat{y})^T \; Cov^{-1}(\hat{y}) \; (y - \hat{y}) \tag{7.2}$$

The error on the unsmearing factor (F) is then propagated as

$$(\Delta\, F)^2 = \frac{\partial\, F}{\partial\, y_i} \frac{\partial\, F}{\partial\, y_j} \; Cov(y_i, y_j) \tag{7.3}$$

where the $\frac{\partial F}{\partial y_i}$ derivatives are calculated numerically.

Figure 7.18 shows the results of the unsmearing factor for the lowest HT3 bin. The error bars correspond to the uncertainty on the ansatz. The size of the errors increases from around 7% at $1 - T_2^t = 1 \times 10^{-1}$ to around 85% at $1 - T_2^t = 1 \times 10^{-4}$. However, there is a strong correlation point to point in $1 - T_2^t$, which introduces a stringent constraint on the shape of the correction. This is illustrated in Figure 7.19.

Besides the ansatz uncertainty, there is another contribution due to the angular and the E_T resolutions errors. In order to account for these, we have calculated Thrust by smearing the generated HERWIG distribution with the high and low corrections for each of the three components. The E_T and η resolutions introduce an error smaller than 0.5% and have been neglected. The effect of the ϕ resolutions is shown in Figures 7.20–7.21, for a logarithmic and linear $1 - T_2^t$ scale, where the fractional difference between the high (low) unsmearing factors and the nominal ones are plotted. The errors are quite symmetric, the largest between the two in each point has been used in the subsequent calculations. This error is then propagated to the unsmearing factor using equation 7.3.

Statistical errors

The statistical error was modified to take into account the fluctuations produced by using different sequences of random numbers in the HERWIG event generation

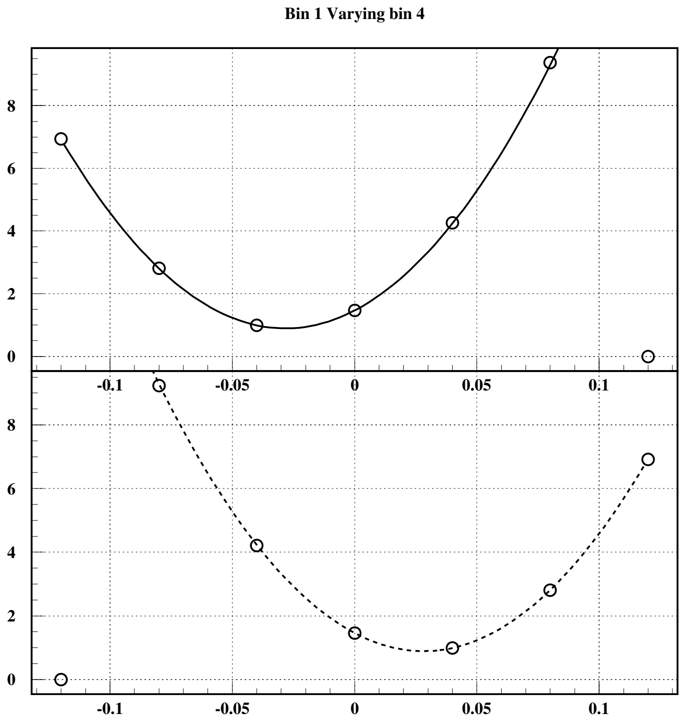

Figure 7.17: χ^2 difference between smeared distributions for two different ansatz distributions: the nominal (shown in Figure 7.14) and the same one with 4% events added (subtracted) in bin 4 for the top (bottom) plot. The abscissa corresponds to the fractional variation of events in bin 1. This example shows negative correlation between the two bins. The plot corresponds to N-paraboloid fit in equation 7.2.

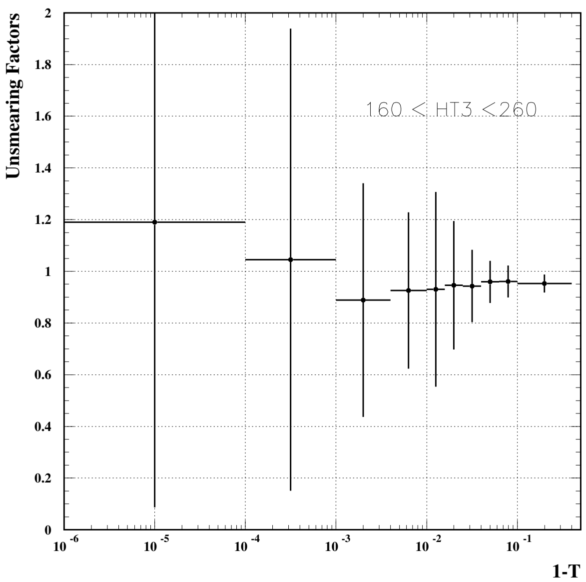

Figure 7.18: Unsmearing factors as a function of 1-T. The error bars correspond to the uncertainty on the ansatz (ΔF, see equation 7.3).

process [1]. The original sample was divided in 30 smaller ones repeating for each of them the process of finding the unsmearing factors. Thus, a distribution of factors, consisting in 30 values, is obtained for each T_2^t bin and the uncertainty is defined as the error of the mean of this distributions.

In the linear case, the factors were fitted with a constant function, however, due to the large statistical fluctuations, the uncertainty was determined from a linear fit to the points.

Final errors are listed in the next chapter where a summary of all experimental uncertainties is presented.

[1] To compensate for the lack of statistics in the gaussian smearing process, events have been reused.

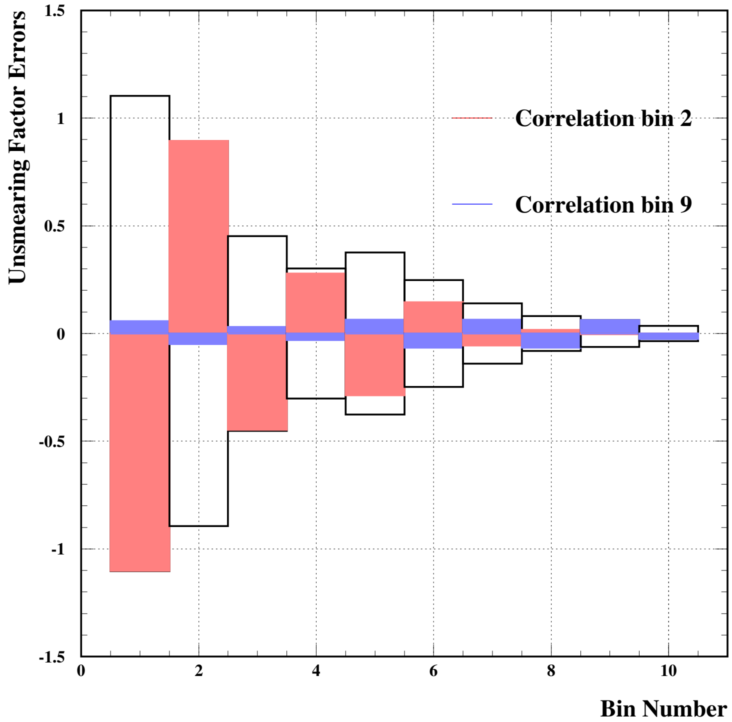

Figure 7.19: Unsmearing factor errors as a function of bin number (the 10 bins correspond to the ones in Figure 7.18). The size of the correlation between bins ($\rho_{ij} = Cov_{ij}/\sqrt{Cov_{ii}\,Cov_{jj}}$) are illustrated by the amount of the error bars filled with a particular color. As an example, the light gray shows the correlation factors of all (1-T) bins with respect to the second one. The first and second bin are therefore fully anti-correlated. In dark gray are shown the correlation factors with respect to the ninth bin.

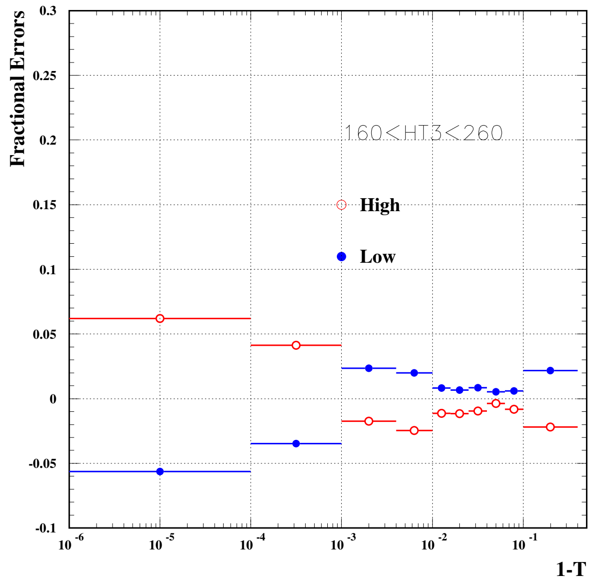

Figure 7.20: Fractional errors on the unsmearing factors due to the ϕ resolution uncertainty (logarithmic scale).

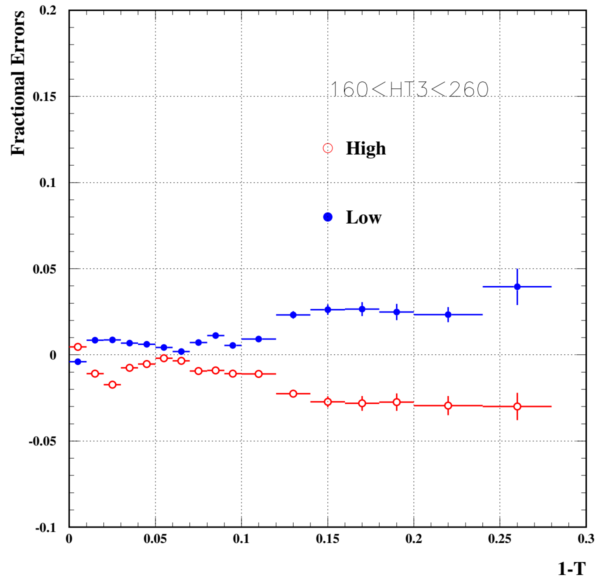

Figure 7.21: Fractional errors on the unsmearing factors due to the ϕ resolution uncertainty (linear scale).

Chapter 8

Final Results and Comparison to Theory

This chapter presents the final results for the differential cross section as a function of dijet transverse thrust, which are derived from the measured distributions (Figures 7.1 and 7.2) after applying the unsmearing corrections.
Figures 8.1 and 8.2 show the cross section for each HT3 bin, as a function of $1 - T_2^t$ in linear and logarithmic scales, respectively. The numerical values along with the statistical uncertainties are summarized in Tables 8.1–8.4.
The experimental errors associated with the measurement, each of which was analyzed in the previous chapter, are presented in the first section, while in the second we compare the final cross section to the NLO (JETRAD) and NLO three jet (NLOJET++) perturbative QCD predictions. Differences between data and theory are first qualitatively discussed and then a quantitative χ^2 hypothesis test conducted.

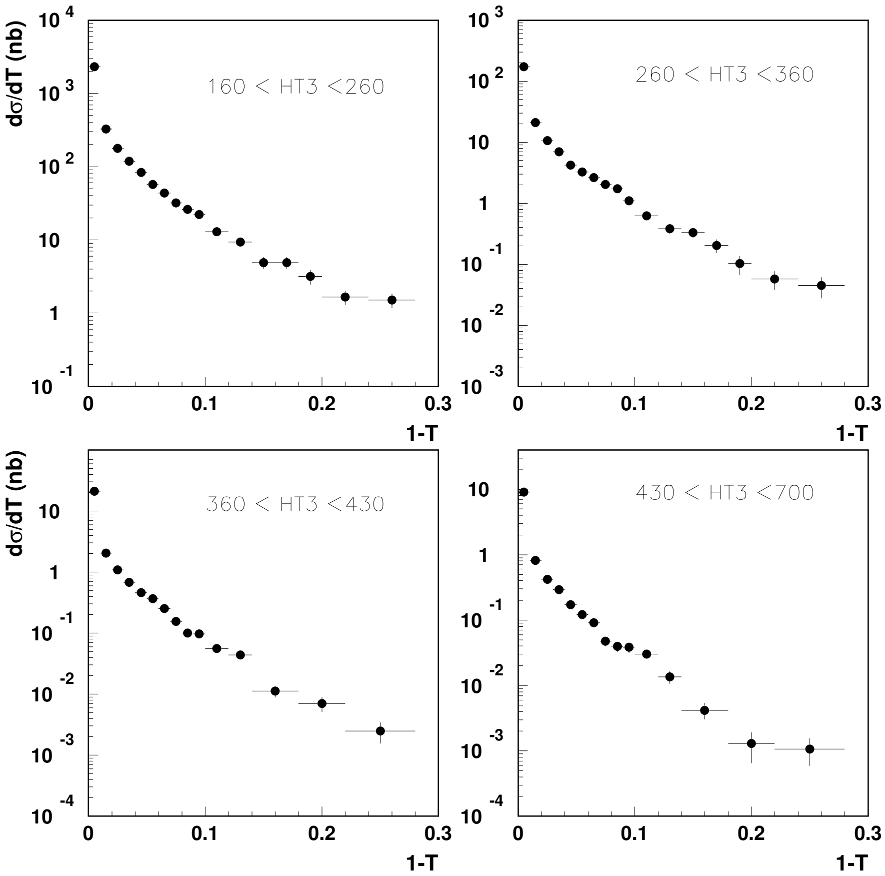

Figure 8.1: Final, unfolded T_2^t cross sections obtained from Run 1b data, for each HT3 bin.

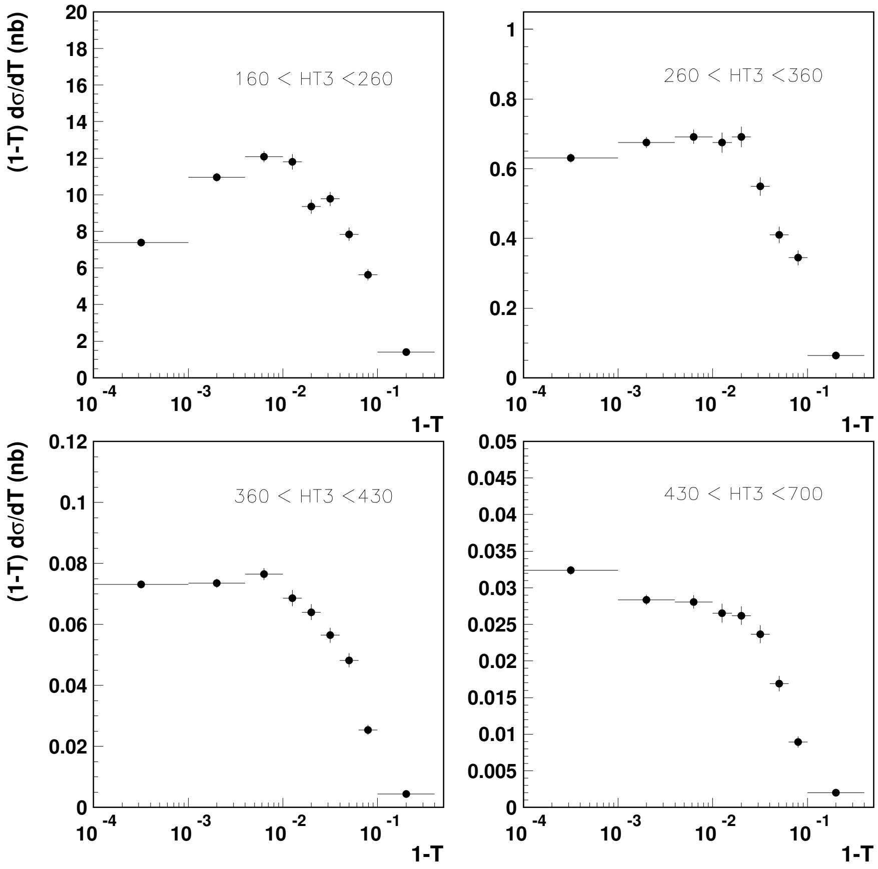

Figure 8.2: Final, unfolded T_2^t cross sections obtained from Run 1b data, for each HT3 bin. The logarithmic scale enhances the region close to $T_2^t = 1$.

Bin Range T_2^t	**Cross Section ± Statistic (nb)** **HT3: [160-260] GeV**	**Cross Section ± Statistic (nb)** **HT3: [260-360] GeV**
0.00-0.01	$(2.31 \pm 0.03)\times10^{3}$	$(1.72 \pm 0.02)\times10^{2}$
0.01-0.02	$(3.28 \pm 0.10)\times10^{2}$	$(2.09 \pm 0.07)\times10^{1}$
0.02-0.03	$(1.77 \pm 0.08)\times10^{2}$	$(1.06 \pm 0.05)\times10^{1}$
0.03-0.04	$(1.18 \pm 0.06)\times10^{2}$	$(6.95 \pm 0.04)\times10^{0}$
0.04-0.05	$(8.38 \pm 0.52)\times10^{1}$	$(4.19 \pm 0.03)\times10^{0}$
0.05-0.06	$(5.74 \pm 0.43)\times10^{1}$	$(3.27 \pm 0.03)\times10^{0}$
0.06-0.07	$(4.35 \pm 0.37)\times10^{1}$	$(2.63 \pm 0.03)\times10^{0}$
0.07-0.08	$(3.20 \pm 0.32)\times10^{1}$	$(2.04 \pm 0.02)\times10^{0}$
0.08-0.09	$(2.60 \pm 0.29)\times10^{1}$	$(1.74 \pm 0.02)\times10^{0}$
0.09-0.10	$(2.22 \pm 0.26)\times10^{1}$	$(1.10 \pm 0.02)\times10^{0}$
0.10-0.12	$(1.29 \pm 0.14)\times10^{1}$	$(6.26 \pm 0.89)\times10^{-1}$
0.12-0.14	$(9.36 \pm 1.21)\times10^{0}$	$(3.83 \pm 0.70)\times10^{-1}$
0.14-0.16	$(4.92 \pm 0.88)\times10^{0}$	$(3.32 \pm 0.65)\times10^{-1}$
0.16-0.18	$(4.92 \pm 0.88)\times10^{0}$	$(2.04 \pm 0.51)\times10^{-1}$
0.18-0.20	$(3.17 \pm 0.71)\times10^{0}$	$(1.02 \pm 0.36)\times10^{-1}$
0.20-0.24	$(1.66 \pm 0.36)\times10^{0}$	$(5.75 \pm 1.92)\times10^{-2}$
0.24-0.28	$(1.51 \pm 0.35)\times10^{0}$	$(4.47 \pm 1.69)\times10^{-2}$

Table 8.1: T_2^t cross sections for two different HT3 bins.

Bin Range T_2^t	**Cross Section ± Statistic (nb)** **HT3: [360-430] GeV**	**Cross Section ± Statistic (nb)** **HT3: [430-700] GeV**
0.00-0.01	$(2.12 \pm 0.02)\times10^{1}$	$(9.08 \pm 0.11)\times10^{0}$
0.01-0.02	$(2.04 \pm 0.06)\times10^{0}$	$(8.20 \pm 0.32\times10^{-1}$
0.02-0.03	$(1.08 \pm 0.05)\times10^{0}$	$(4.18 \pm 0.23\times10^{-1}$
0.03-0.04	$(6.78 \pm 0.38)\times10^{-1}$	$(2.92 \pm 0.19\times10^{-1}$
0.04-0.05	$(4.57 \pm 0.31)\times10^{-1}$	$(1.72 \pm 0.14\times10^{-1}$
0.05-0.06	$(3.67 \pm 0.28)\times10^{-1}$	$(1.21 \pm 0.12\times10^{-1}$
0.06-0.07	$(2.51 \pm 0.23)\times10^{-1}$	$(9.13 \pm 1.08\times10^{-2}$
0.07-0.08	$(1.55 \pm 0.18)\times10^{-1}$	$(4.76 \pm 0.78)\times10^{-2}$
0.08-0.09	$(1.01 \pm 0.14)\times10^{-1}$	$(3.99 \pm 0.72)\times10^{-2}$
0.09-0.10	$(9.67 \pm 1.44)\times10^{-2}$	$(3.85 \pm 0.70)\times10^{-2}$
0.10-0.12	$(5.58 \pm 0.77)\times10^{-2}$	$(3.02 \pm 0.44)\times10^{-2}$
0.12-0.14	$(4.40 \pm 0.69)\times10^{-2}$	$(1.35 \pm 0.29)\times10^{-2}$
0.14-0.18	$(1.13 \pm 0.25)\times10^{-2}$	$(4.18 \pm 1.16)\times10^{-3}$
0.18-0.22	$(6.98 \pm 1.94)\times10^{-3}$	$(1.29 \pm 0.64)\times10^{-3}$
0.22-0.28	$(2.51 \pm 0.95)\times10^{-3}$	$(1.07 \pm 0.48)\times10^{-3}$

Table 8.2: T_2^t cross sections for two different HT3 bins.

Bin Range $1 - T_2^t$	**Cross Section ± Statistic (nb)** **HT3: [160-260] GeV**	**Cross Section ± Statistic (nb)** **HT3: [260-360] GeV**
$10^{-4.0} - 10^{-3.0}$	$(7.39 \pm 0.16)\times10^{0}$	$(6.31 \pm 0.13)\times10^{-1}$
$10^{-3.0} - 10^{-2.4}$	$(1.10 \pm 0.02)\times10^{1}$	$(6.75 \pm 0.16)\times10^{-1}$
$10^{-2.4} - 10^{-2.0}$	$(1.21 \pm 0.03)\times10^{1}$	$(6.91 \pm 0.20)\times10^{-1}$
$10^{-2.0} - 10^{-1.8}$	$(1.18 \pm 0.04)\times10^{1}$	$(6.74 \pm 0.28)\times10^{-1}$
$10^{-1.8} - 10^{-1.6}$	$(9.35 \pm 0.38)\times10^{0}$	$(6.91 \pm 0.29)\times10^{-1}$
$10^{-1.6} - 10^{-1.4}$	$(9.77 \pm 0.39)\times10^{0}$	$(5.49 \pm 0.26)\times10^{-1}$
$10^{-1.4} - 10^{-1.2}$	$(7.85 \pm 0.35)\times10^{0}$	$(4.10 \pm 0.23)\times10^{-1}$
$10^{-1.2} - 10^{-1.0}$	$(5.63 \pm 0.30)\times10^{0}$	$(3.44 \pm 0.21)\times10^{-1}$
$10^{-1.0} - 10^{-0.4}$	$(1.42 \pm 0.09)\times10^{0}$	$(6.40 \pm 0.52)\times10^{-2}$

Table 8.3: T_2^t cross sections for two different HT3 bins.

Bin Range $1 - T_2^t$	**Cross Section ± Statistic (nb)** **HT3: [360-430] GeV**	**Cross Section ± Statistic (nb)** **HT3: [430-700] GeV**
$10^{-4.0} - 10^{-3.0}$	$(7.32 \pm 0.12)\times10^{-2}$	$(3.24 \pm 0.06)\times10^{-2}$
$10^{-3.0} - 10^{-2.4}$	$(7.35 \pm 0.15)\times10^{-2}$	$(2.84 \pm 0.07)\times10^{-2}$
$10^{-2.4} - 10^{-2.0}$	$(7.65 \pm 0.19)\times10^{-2}$	$(2.81 \pm 0.09)\times10^{-2}$
$10^{-2.0} - 10^{-1.8}$	$(6.85 \pm 0.27)\times10^{-2}$	$(2.65 \pm 0.13)\times10^{-2}$
$10^{-1.8} - 10^{-1.6}$	$(6.40 \pm 0.26)\times10^{-2}$	$(2.62 \pm 0.13)\times10^{-2}$
$10^{-1.6} - 10^{-1.4}$	$(5.65 \pm 0.25)\times10^{-2}$	$(2.36 \pm 0.12)\times10^{-2}$
$10^{-1.4} - 10^{-1.2}$	$(4.82 \pm 0.23)\times10^{-2}$	$(1.69 \pm 0.11)\times10^{-2}$
$10^{-1.2} - 10^{-1.0}$	$(2.54 \pm 0.16)\times10^{-2}$	$(8.94 \pm 0.76)\times10^{-3}$
$10^{-1.0} - 10^{-0.4}$	$(4.33 \pm 0.37)\times10^{-3}$	$(2.01 \pm 0.21)\times10^{-3}$

Table 8.4: T_2^t cross sections for two different HT3 bins.

8.1 Experimental Uncertainties

The experimental uncertainties due to the data selection efficiencies, luminosity determination, the low E_T jets effect (noise and reconstruction inefficiencies), the jet momentum scale (JMS), position bias and unfolding corrections were discussed in detail in the previous chapter. This section presents a summary which includes the magnitude of each error along with the total uncertainties calculated as the quadrature sum of all contributions. Figures 8.3-8.4 show the fractional uncertainties in percentage for the lowest and highest HT3 bin, excluding the unfolding error, as a function of T_2^t for logarithmic and linear scales. The total errors range between $15 - 25\%$. The JMS and the Luminosity uncertainties dominate except for high T_2^t values where the errors due to the unfolding method have a large impact. It is in this region where the migration of events between T_2^t bins due to the finite ϕ resolution becomes important. The unfolding error is presented separately in Figures 8.5 and 8.6. The bars in the plots correspond to the quadrature sum of the statistical errors and the systematics due to the uncertainty on the ansatz and the angular resolutions. It is the uncertainty on the ansatz which dominates at high T_2^t, reaching around 85% for the lower HT3 bin. However, since there is a strong negative correlation point-to-point in 1-T_2^t, the freedom for the thrust distribution to fluctuate within the systematic error band is severely constrained (see Figure 7.19).

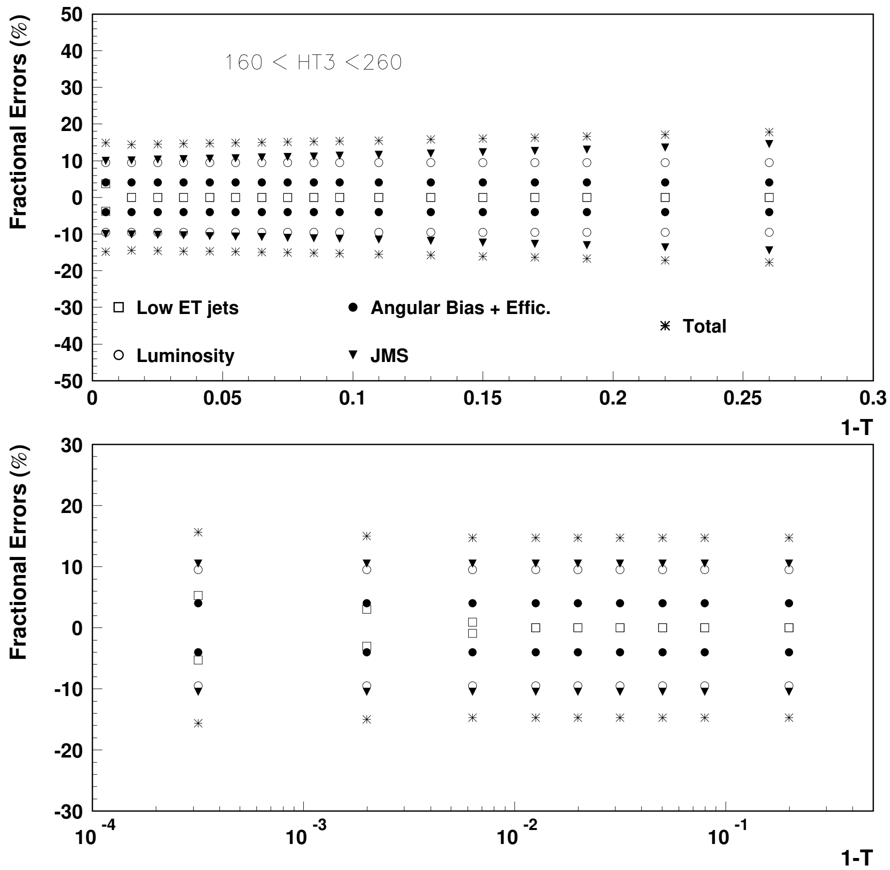

Figure 8.3: Fractional experimental uncertainties as a function of 1-T_2^t in linear and logarithmic scale. The total errors correspond to the quadrature sum of each of the contributions shown in the plots (it does not include the contribution from the error on the unsmearing factors).

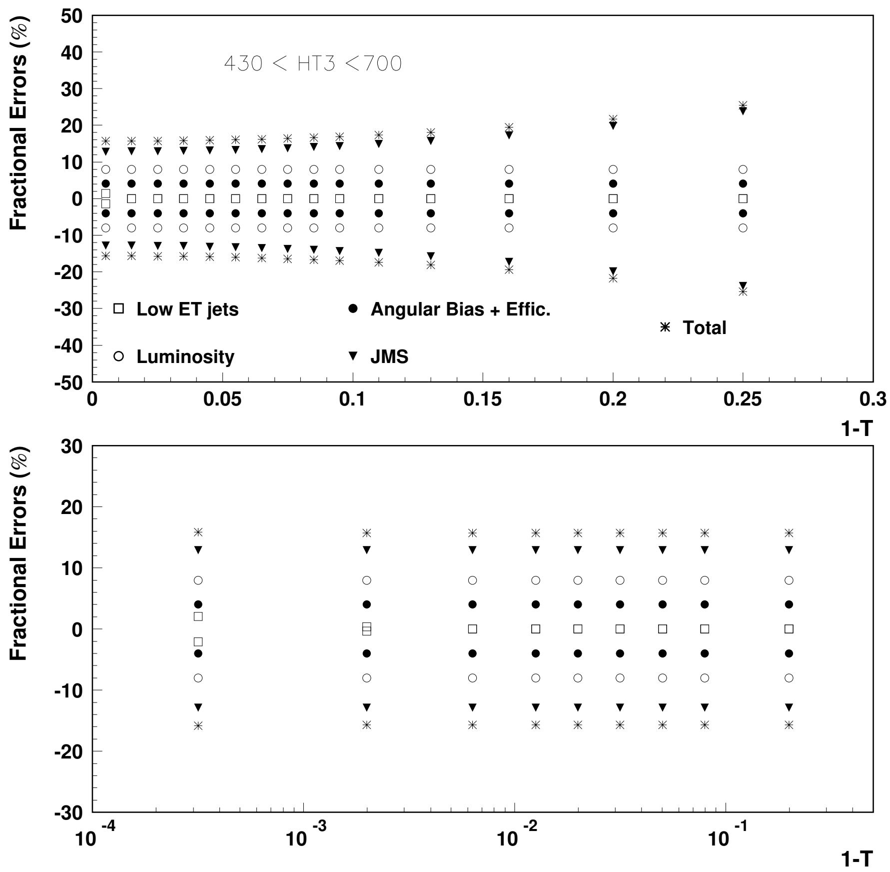

Figure 8.4: Fractional experimental uncertainties as a function of 1-T_2^t in linear and logarithmic scale. The total errors correspond to the quadrature sum of each of the contributions shown in the plots (it does not include the contribution from the error on the unsmearing factors).

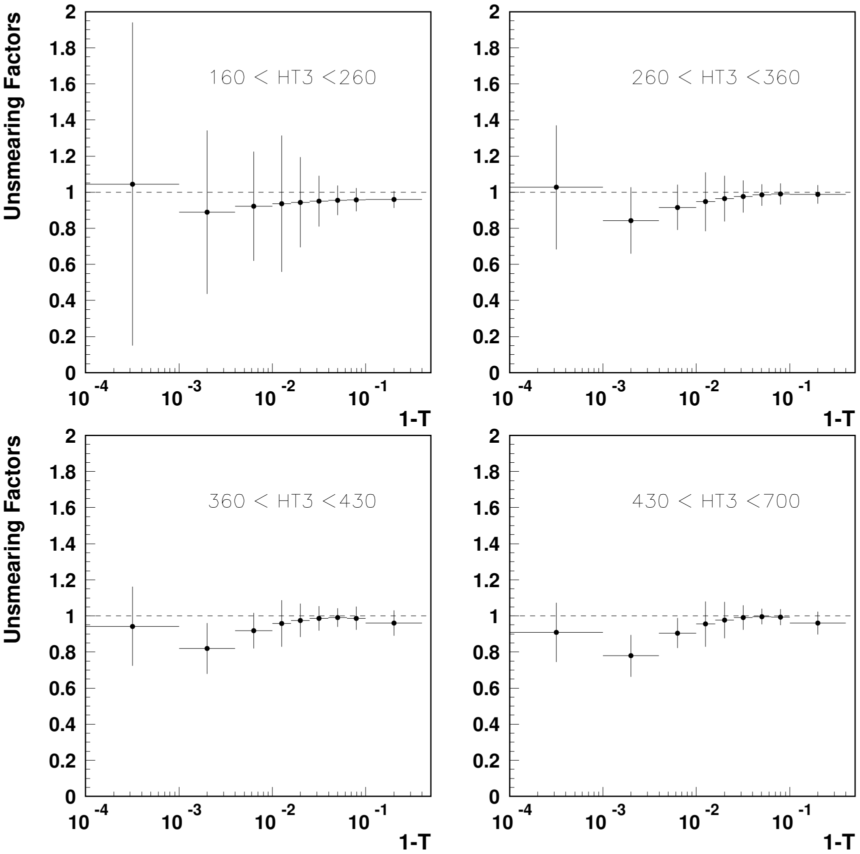

Figure 8.5: Unsmearing factors as a function of 1-T. All errors are included.

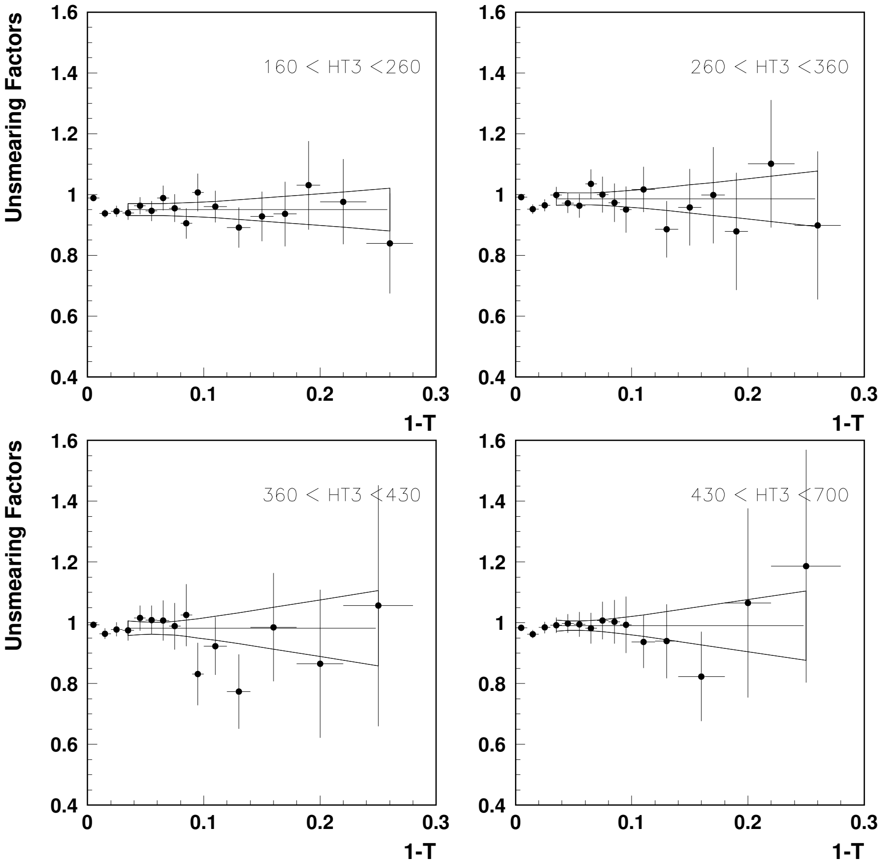

Figure 8.6: Unsmearing factors as a function of 1-T. A constant fit has been done from $T_2^t = 0.04$. The band corresponds to the unsmearing factor error in this region.

The errors sources relevant to this analysis, with their degree of correlation, are listed in Table 8.5. The uncertainties due to each component of the jet momentum scale correction were determined from the ratio between the nominal T_2^t distribution and the one calculated by varying each contribution within its error. The different errors together with their degree of correlation and the statistical uncertainties are combined into a full error matrix, which is available on the web [46].

Error Source	**Correlation in T_2^t**	**Order of Magnitude**	**Correlation in HT3**
Statistical	uncorrelated	$0.5 - 25\%$	uncorrelated
Luminosity	correlated	8%	correlated
Luminosity Matching			
Jet_30	correlated	5%	correlated
Jet_50	correlated	3%	correlated
Resolution + Unfold	anti-correlated	up to 85%	partially corr.
Select Efficiencies	correlated	3.5%	partially corr.
Mom Scale Response	correlated	$10 - 22\%$	partially corr.
Mom Scale Offset Errors	correlated	$2 - 10\%$	correlated

Table 8.5: Sources of errors of the cross section and their degree of correlation.

8.2 Data and Theory Comparison

This section presents a comparison between data and the theoretical predictions given by JETRAD and NLOJET++ . As it was discussed before, a prediction of order $O(\alpha_s^3)$, such as JETRAD, can only reach the value $T_2^t = \sqrt{3}/2$ since it has at most three partons in the final state. The LO prediction for the variable in the range

$\sqrt{2}/2 \le T_2^t < \sqrt{3}/2$, corresponds to a calculation of order $O(\alpha_s^4)$. This prediction is provided by NLOJET++ , a NLO three jet generator.

8.2.1 Comparison with NLO perturbative QCD predictions

Data T_2^t distributions (D) and NLO JETRAD predictions (T) are shown in Figures 8.7-8.10 in logarithmic and linear scale. For this comparison we have used the CTEQ4HJ PDF and set $\mu_R = \mu_F = \mu = p_{T_{max}}/2$.

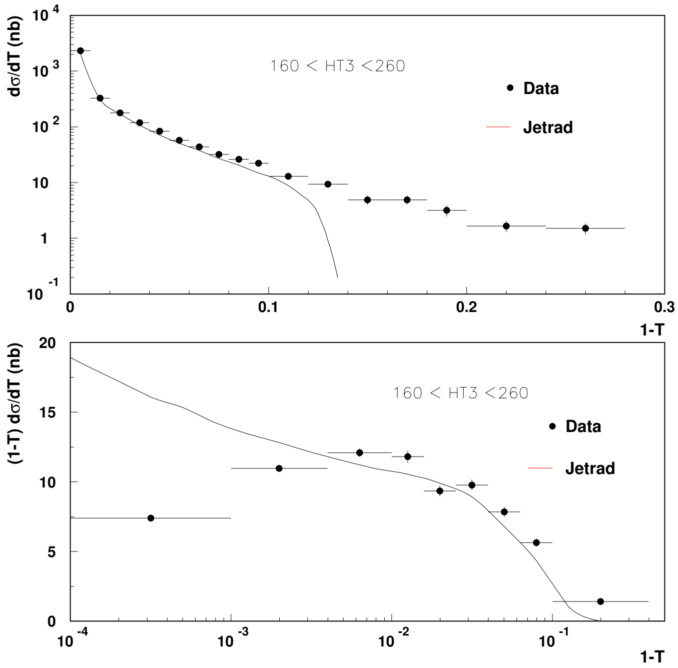

Figure 8.7: Data comparison with NLO JETRAD prediction, for the first HT3 bin (with CTEQ4HJ, $s_{min} = 1$ GeV^2 and $\mu = p_{T_{max}}/2$). Only statistical errors are plotted.

Data and theory agree quite well except at both ends of the T_2^t range. It is interesting to note that the disagreement at high thrust values seems to diminish as HT3 increases.

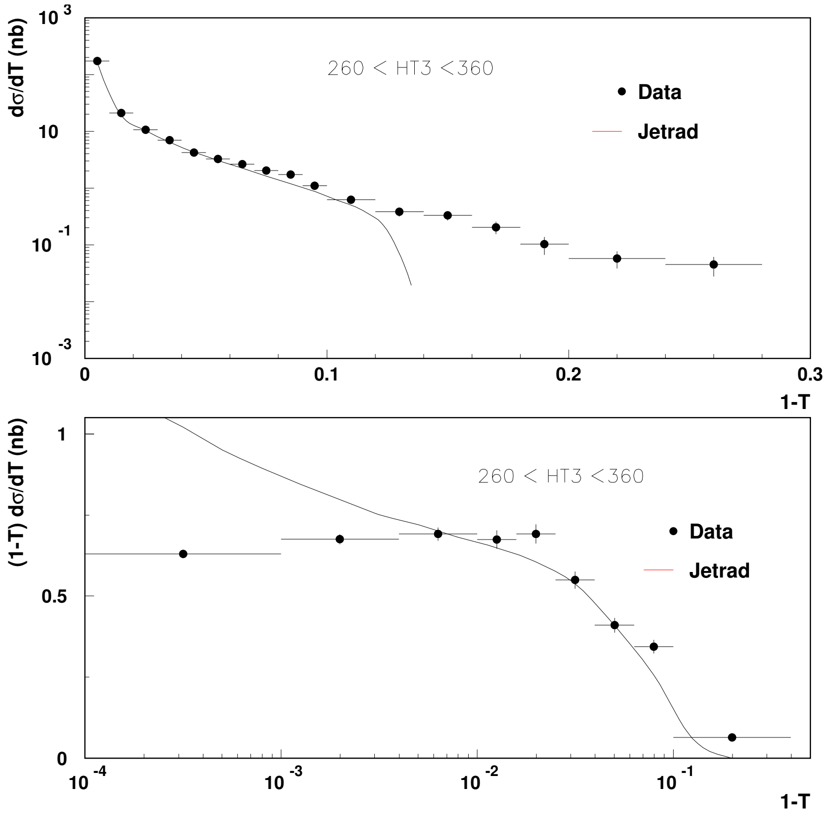

Figure 8.8: Data comparison with NLO JETRAD prediction, for the second HT3 bin (with CTEQ4HJ, $s_{min} = 1$ GeV^2 and $\mu = p_{T_{max}}/2$). Only statistical errors are plotted.

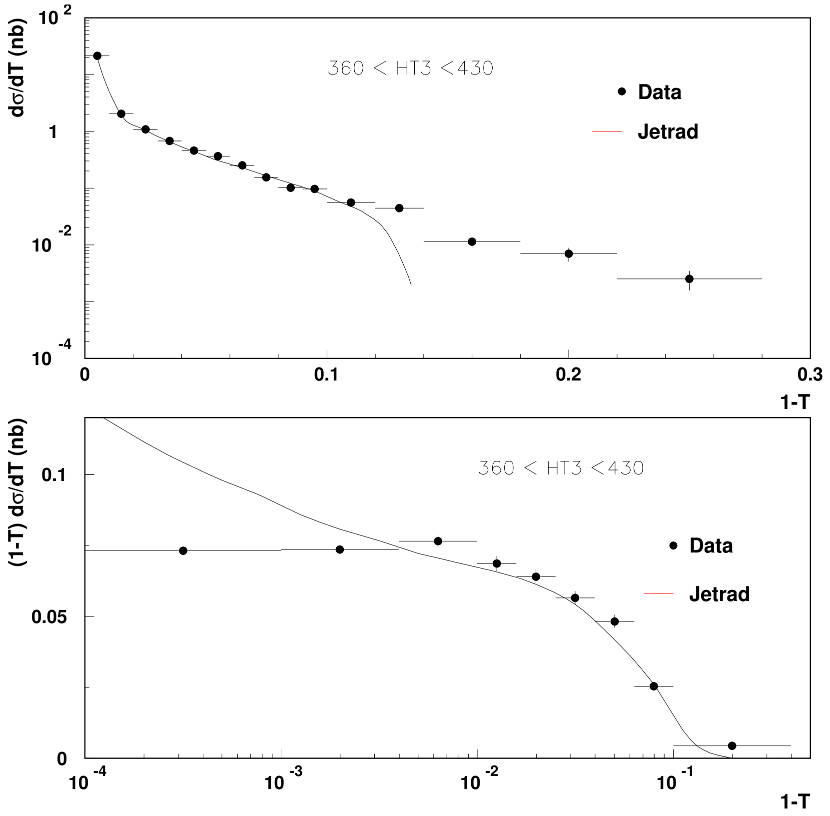

Figure 8.9: Data comparison with NLO JETRAD prediction, for the third HT3 bin (with CTEQ4HJ, $s_{min} = 1$ GeV^2 and $\mu = p_{T_{max}}/2$). Only statistical errors are plotted.

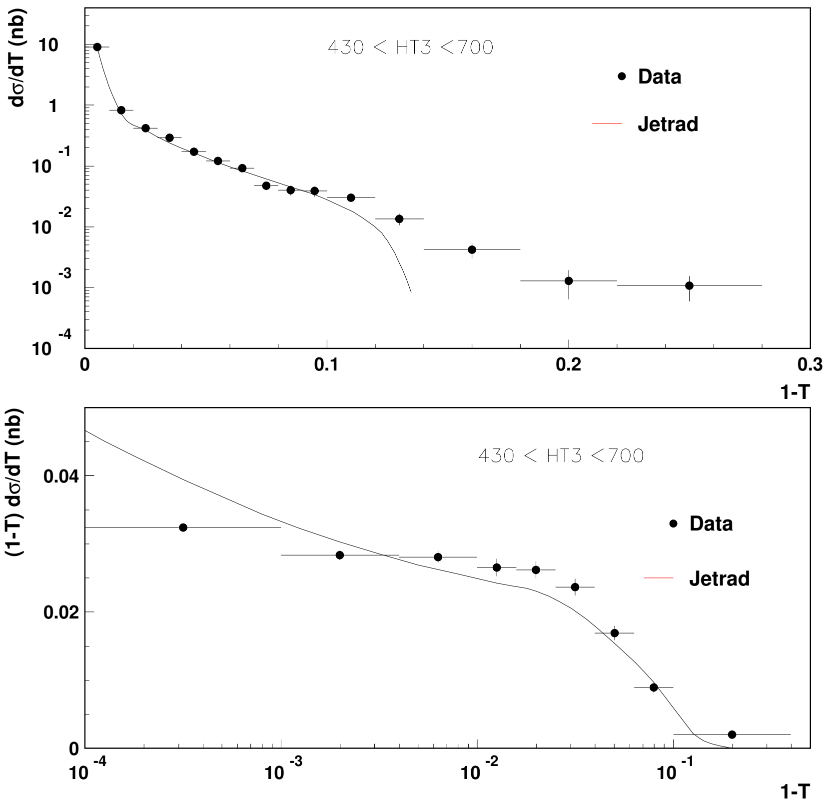

Figure 8.10: Data comparison with NLO JETRAD prediction, for the fourth HT3 bin (with CTEQ4HJ, $s_{min} = 1$ GeV^2 and $\mu = p_{T_{max}}/2$). Only statistical errors are plotted.

A more quantitative measure is given by the χ^2 test:

$$\chi^2 = \sum_{ij} (D_i - T_i)\, Cov_{ij}^{-1}\, (D_j - T_j) \tag{8.1}$$

where $D_i - T_i$ is the difference between the measured cross section and the theoretical prediction in the i–th bin, and Cov_{ij} is the full covariance matrix of our measurements. It is calculated from the absolute errors and the fractional ones which have been multiplied by a fit to the data in order not to introduce a statistical component to the systematic errors [47]. Figures 8.11–8.18 show the linear differences, *ie*, $(D - T)/T$, between data and theoretical predictions. The bars correspond to the statistical errors while the bands are the systematic ones. Tables 8.6–8.13 show the results of the test.

The results in linear scale indicate that there is agreement with the NLO JETRAD prediction for $1 - T_2^t$ in the range [0,0.12], with χ^2 probabilities that vary between 6 and 76%. Above $1 - T_2^t = 0.12$ the χ^2 comparison worsens up quickly. Higher order calculations are therefore important near and above the theoretical limit of $T_2^t = \sqrt{3}/2$.

In logarithmic scale, there is agreement for $1 - T_2^t$ in the range $[10^{-3}, 10^{-1.2}]$. The χ^2 test fails completely when extending the range down to 10^{-4}. Although data and theory are within the systematic error band in this region, the χ^2 test is not satisfied because the dominant systematic error, due to the unsmearing ansatz, shows a strong negative correlation from bin to bin.

In the $T_2^t \to 1$ limit fixed order predictions were expected to fail. The results show that the variable is indeed sensitive to the effect of soft and collinear radiation emission. This disagreement diminishes as HT3 increases. At large HT3, the value of α_s decreases and higher order contributions, which are of the form $(\alpha_s \ln^2(1-T))^n$, are therefore expected to be smaller.

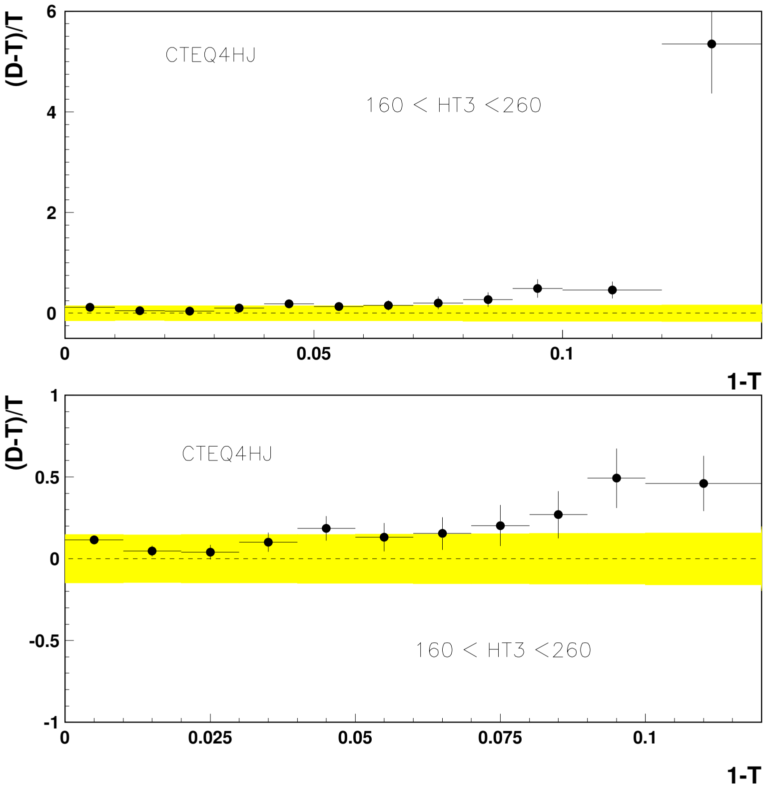

Figure 8.11: Data comparison with NLO JETRAD prediction ($\mu = p_{T_{max}}/2$). The bars correspond to the statistical errors while the bands are the systematic ones. They are basically fully correlated.

Thrust Range (1-T)	PDF	χ^2	ndof	Prob(%)
0.–0.10	CTEQ4HJ	10.19	10	42.40
0.–0.12	CTEQ4HJ	12.98	11	29.46
0.–0.14	CTEQ4HJ	41.52	12	0.004

Table 8.6: Results of the χ^2 test between data and JETRAD predictions, for different ranges in T_2^t .

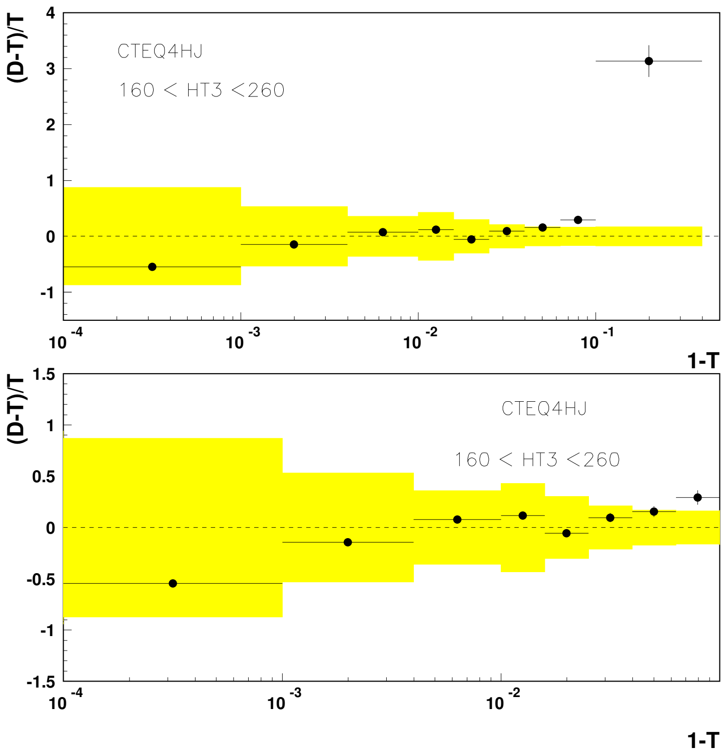

Figure 8.12: Data comparison with NLO JETRAD prediction ($\mu = p_{T_{max}}/2$). The bars correspond to the statistical errors while the bands are the systematic ones.

Thrust Range (1-T)	PDF	χ^2	ndof	Prob(%)
$10^{-2.4} - 10^{-1.2}$	CTEQ4HJ	2.69	5	74.76
$10^{-3.0} - 10^{-1.2}$	CTEQ4HJ	3.76	6	70.9
$10^{-2.4} - 10^{-1.0}$	CTEQ4HJ	9.93	6	12.76
$10^{-4.0} - 10^{-1.2}$	CTEQ4HJ	95.08	7	0.

Table 8.7: Results of the χ^2 test between data and JETRAD predictions, for different ranges in T_2^t .

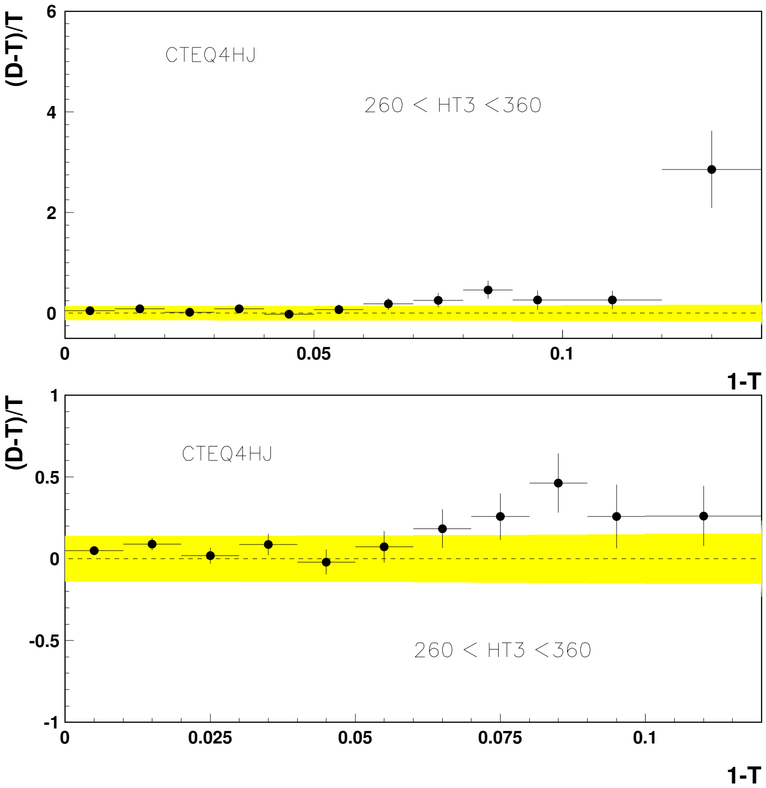

Figure 8.13: Data comparison with NLO JETRAD prediction (with CTEQ4HJ and $\mu = p_{T_{max}}/2$). The bars correspond to the statistical errors while the bands are the systematic ones. They are basically fully correlated.

Thrust Range (1-T)	PDF	χ^2	ndof	Prob(%)
0.–0.10	CTEQ4HJ	10.20	10	42.31
0.–0.12	CTEQ4HJ	10.88	11	45.33
0.–0.14	CTEQ4HJ	22.85	12	2.9

Table 8.8: Results of the χ^2 test between data and JETRAD predictions, for different ranges in T_2^t .

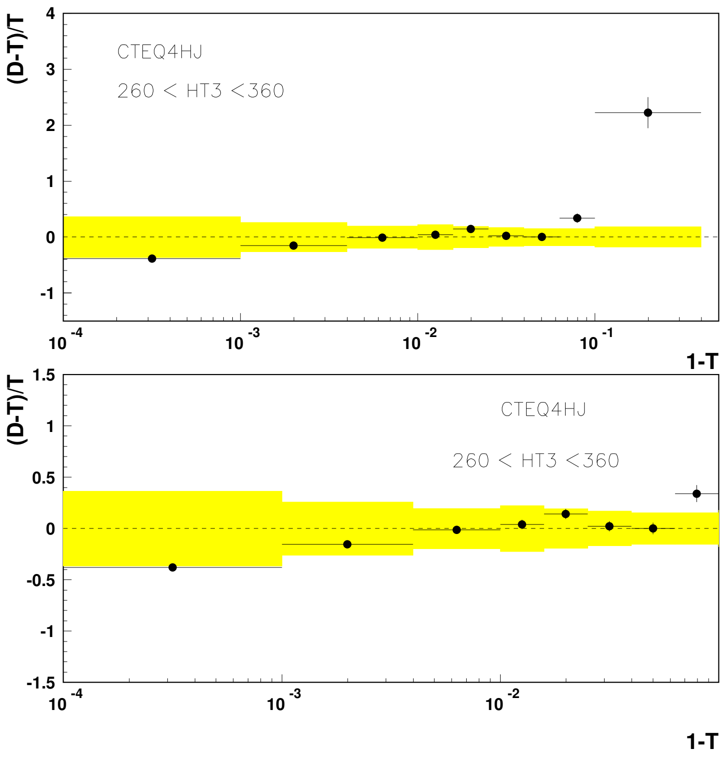

Figure 8.14: Data comparison with NLO JETRAD prediction (with CTEQ4HJ and $\mu = p_{T_{max}}/2$). The bars correspond to the statistical errors while the bands are the systematic ones.

Thrust Range (1-T)	PDF	χ^2	ndof	Prob(%)
$10^{-2.4} - 10^{-1.2}$	CTEQ4HJ	2.12	5	83.2
$10^{-3.0} - 10^{-1.2}$	CTEQ4HJ	8.36	6	21.29
$10^{-2.4} - 10^{-1.0}$	CTEQ4HJ	8.33	6	21.49
$10^{-4.0} - 10^{-1.2}$	CTEQ4HJ	81.68	7	0.

Table 8.9: Results of the χ^2 test between data and JETRAD predictions, for different ranges in T_2^t .

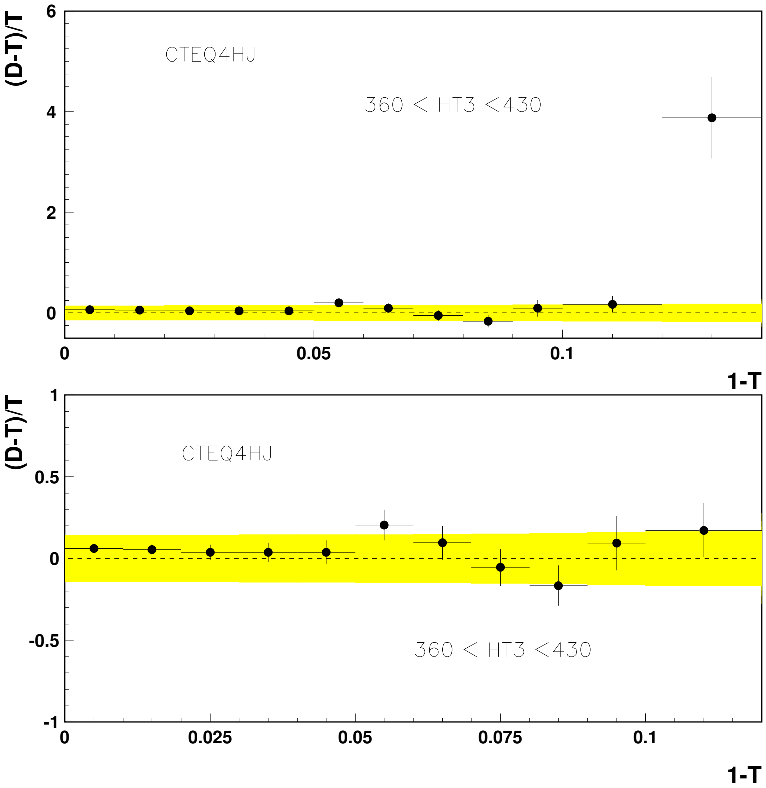

Figure 8.15: Data comparison with NLO JETRAD prediction (with CTEQ4HJ and $\mu = p_{T_{max}}/2$). The bars correspond to the statistical errors while the bands are the systematic ones. They are basically fully correlated.

Thrust Range (1-T)	PDF	χ^2	ndof	Prob(%)
0.–0.10	CTEQ4HJ	6.96	10	72.92
0.–0.12	CTEQ4HJ	7.39	11	76.67
0.–0.14	CTEQ4HJ	29.49	12	0.33

Table 8.10: Results of the χ^2 test between data and JETRAD predictions, for different ranges in T_2^t .

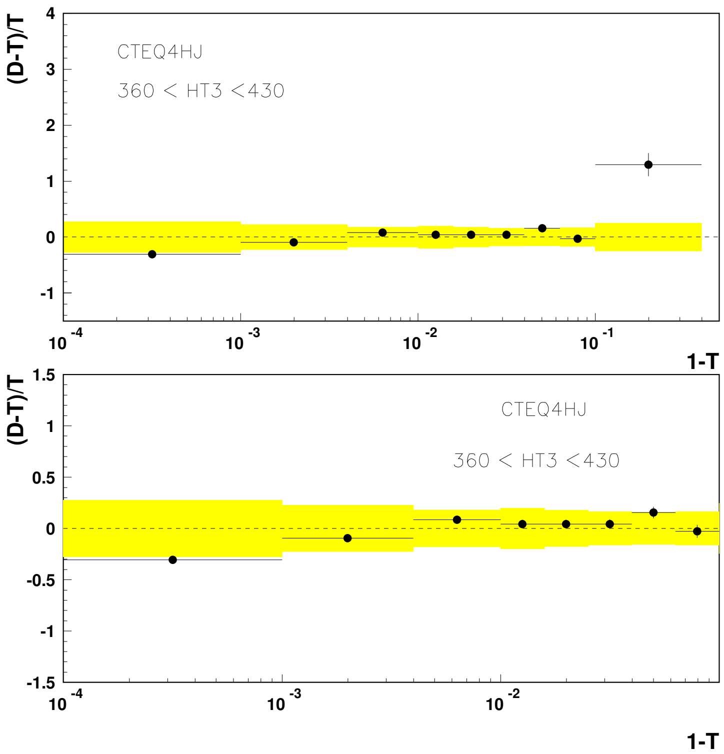

Figure 8.16: Data comparison with NLO JETRAD prediction (with CTEQ4HJ and $\mu = p_{T_{max}}/2$). The bars correspond to the statistical errors while the bands are the systematic ones.

Thrust Range (1-T)	PDF	χ^2	ndof	Prob(%)
$10^{-2.4} - 10^{-1.2}$	CTEQ4HJ	1.77	5	87.9
$10^{-3.0} - 10^{-1.2}$	CTEQ4HJ	3.07	6	80.
$10^{-2.4} - 10^{-1.0}$	CTEQ4HJ	2.08	6	91.2
$10^{-4.0} - 10^{-1.2}$	CTEQ4HJ	62.15	7	0.

Table 8.11: Results of the χ^2 test between data and JETRAD predictions, for different ranges in T_2^t .

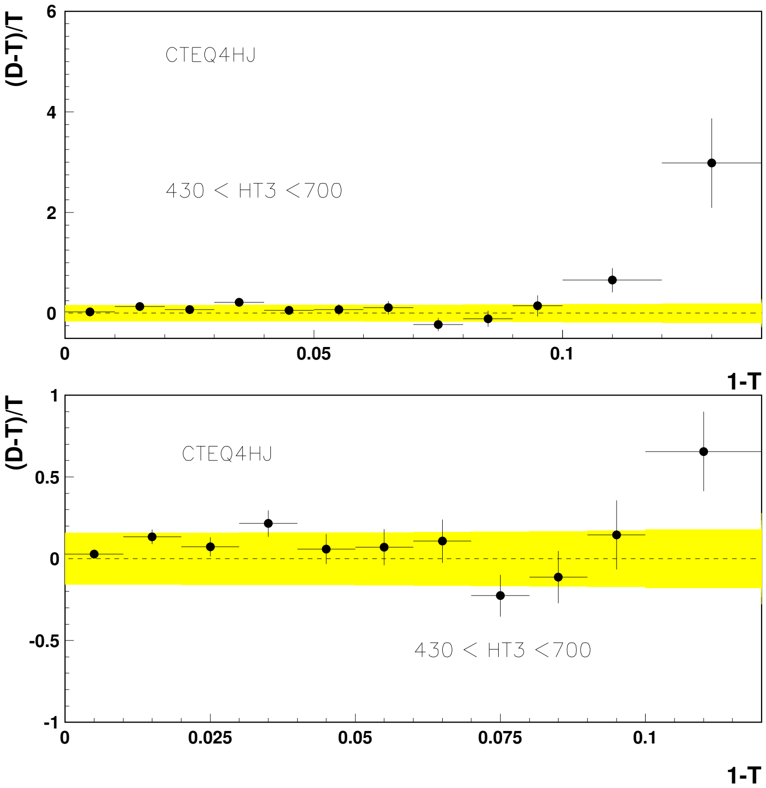

Figure 8.17: Data comparison with NLO JETRAD prediction (with CTEQ4HJ and $\mu = p_{T_{max}}/2$). The bars correspond to the statistical errors while the bands are the systematic ones. They are basically fully correlated.

Thrust Range (1-T)	PDF	χ^2	ndof	Prob(%)
0.–0.10	CTEQ4HJ	12.99	10	22.42
0.–0.12	CTEQ4HJ	18.77	11	6.53
0.–0.14	CTEQ4HJ	28.26	12	0.51

Table 8.12: Results of the χ^2 test between data and JETRAD predictions, for different ranges in T_2^t .

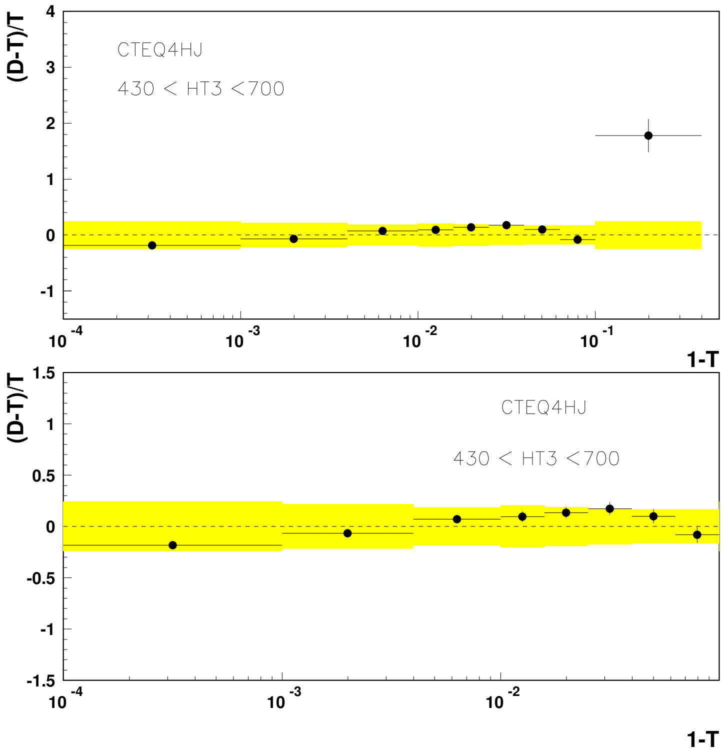

Figure 8.18: Data comparison with NLO JETRAD prediction (with CTEQ4HJ and $\mu = p_{T_{max}}/2$). The bars correspond to the statistical errors while the bands are the systematic ones.

Thrust Range (1-T)	PDF	χ^2	ndof	Prob(%)
$10^{-2.4} - 10^{-1.2}$	CTEQ4HJ	1.58	5	90.3
$10^{-3.0} - 10^{-1.2}$	CTEQ4HJ	4.75	6	57.6
$10^{-2.4} - 10^{-1.0}$	CTEQ4HJ	5.44	6	48.9
$10^{-4.0} - 10^{-1.2}$	CTEQ4HJ	27.69	7	0.025

Table 8.13: Results of the χ^2 test between data and JETRAD predictions, for different ranges in T_2^t .

8.2.1.1 Dependence of theoretical predictions on PDF and renormalization scale

In order to generate the NLO QCD prediction, the parton distribution function (PDF) and the renormalization and factorization scales (μ_R and μ_F) need to be chosen. The dependence on the PDF was tested using different distributions. Figures 8.19 shows that the theoretical uncertainty is less than 5% for the whole kinematic range.

Truncation of the QCD predictions at some order introduces a dependence on the renormalization scale. This dependence should reduce as more terms are included in the perturbative calculation. In this case, we have used 3 different μ values. As it is shown in Figures 8.20, a change on μ does not distort the shape of the distribution, although it affects the normalization. The variation with μ for any value of T_2^t different from 1 is due only to the α_s dependence on the scale since JETRAD prediction corresponds to a LO calculation. The functional dependence at two loops is $\alpha_s(\mu^2) = \frac{1}{b \ln \mu^2/\lambda^2}\left[1 - \frac{b' \ln\ln \mu^2/\lambda^2}{b \ln \mu^2/\lambda^2}\right]$, where λ is the order of magnitude at which α_s becomes strong [48]. The ratio with $\mu = p_T/2$ and $\mu = p_T$ is consistent with what it is shown in the plot (recall that the order of the calculation is α_s^3). For $T_2^t = 1$, where the prediction is NLO, the dependence on the renormalization scale partially cancels between the tree level and 1-loop $2 \to 2$ parton diagrams.

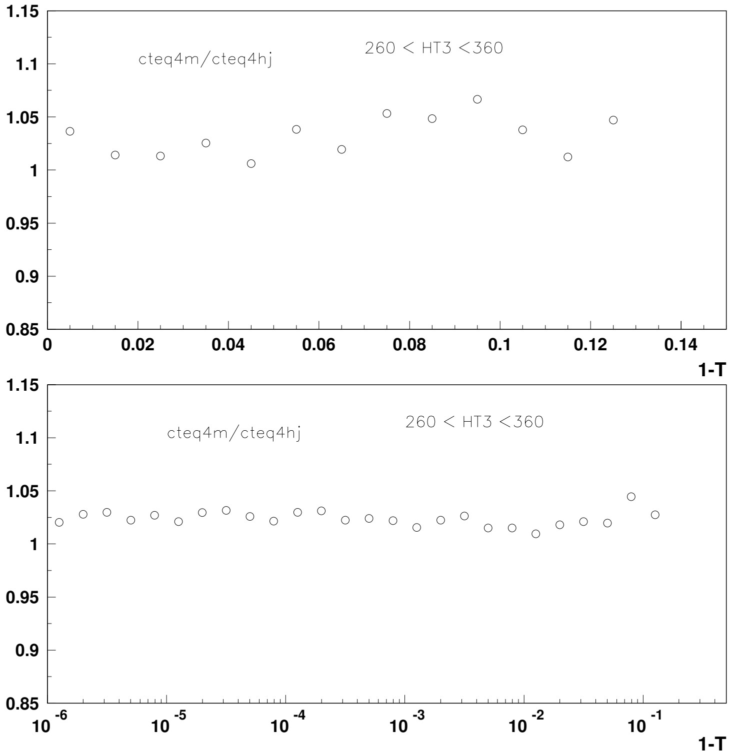

Figure 8.19: Dependence of JETRAD T_2^t distributions on the PDF for the second HT3 bin. The open circles correspond to the ratio cteq4m/cteq4hj.

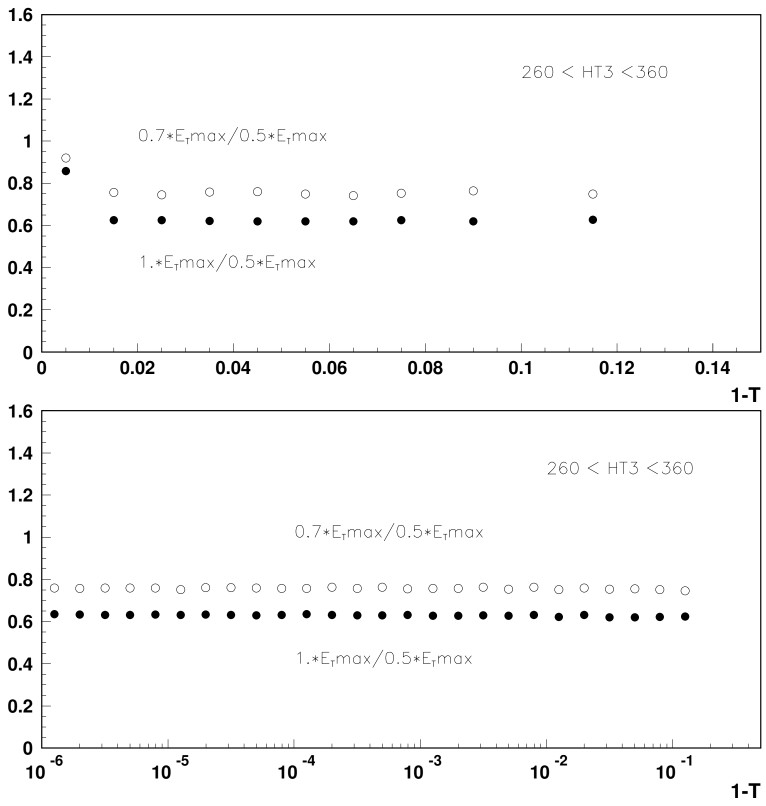

Figure 8.20: Dependence of JETRAD T_2^t distributions on the renormalization scale for the second bin of HT3. The open circles correspond to the ratio of $0.7 * E_T max/0.5 * E_T max$ and the full ones to $1 * E_T max/0.5 * E_T max$.

8.2.2 Comparison with NLO three jet perturbative QCD predictions

This section is devoted to the comparison with the recently developed NLO 3 jet generator, NLOJET++ . His author has kindly provided us with the T_2^t cross section prediction using our same cuts and binning which we have compared with our results and also with JETRAD cross sections. It can be observed from Figures 8.21– 8.24, which present the cross sections in logarithmic and linear scales, that the NLO 3-jet calculation indeed provides a prediction that extends to the whole T_2^t range. The bin that contains the $T_2^t = 1$ point is excluded. It is clear from the plots in logarithmic scale that NLOJET++ cross sections are smaller both with respect to the ones provided by JETRAD and to the measured distributions. This effect diminishes as HT3 increases.

The fact that we use HT3 to estimate the energy scale of the event could be the reason that the $O(\alpha_s^4)$ prediction is lower than the $O(\alpha_s^3)$ one. In this case, HT3 is equal to the transverse energy involved in the hard interaction, since they have at most three partons in the final state. When this observable is calculated for NLOJET++ generated events, HT3 could be smaller than the available transverse energy if four jets are obtained in the final state. The probability for this to happen decreases with HT3. At high energies radiated partons tend to be more collimated and do not form a separate jet. Besides, α_s decreases with the energy scale of the hard interaction and therefore it becomes harder to produce four partons in the final state. This α_s dependence with the energy also implies that higher order corrections are smaller as HT3 increases.

For a clearer comparison, linear differences, $(D-T)/T$, between data and theoretical predictions are presented in Figures 8.25-8.28 while Tables 8.14-8.17 show the results of a χ^2 test.

Since the program is not available for us to run, we could not study the dependence neither on the PDF nor on the renormalization scale which we expect to be important above $T_2^t = \sqrt{3}/2$ where the prediction is again LO.

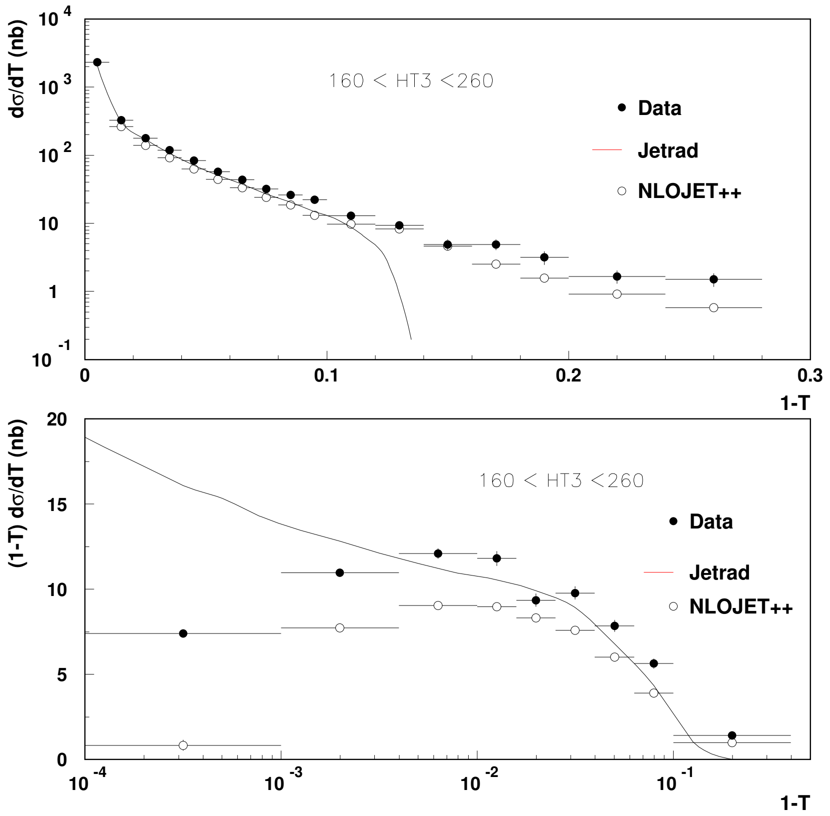

Figure 8.21: Data and NLO three jets NLOJET++ cross sections. JETRAD predictions are also shown for comparison. Only statistical errors are plotted.

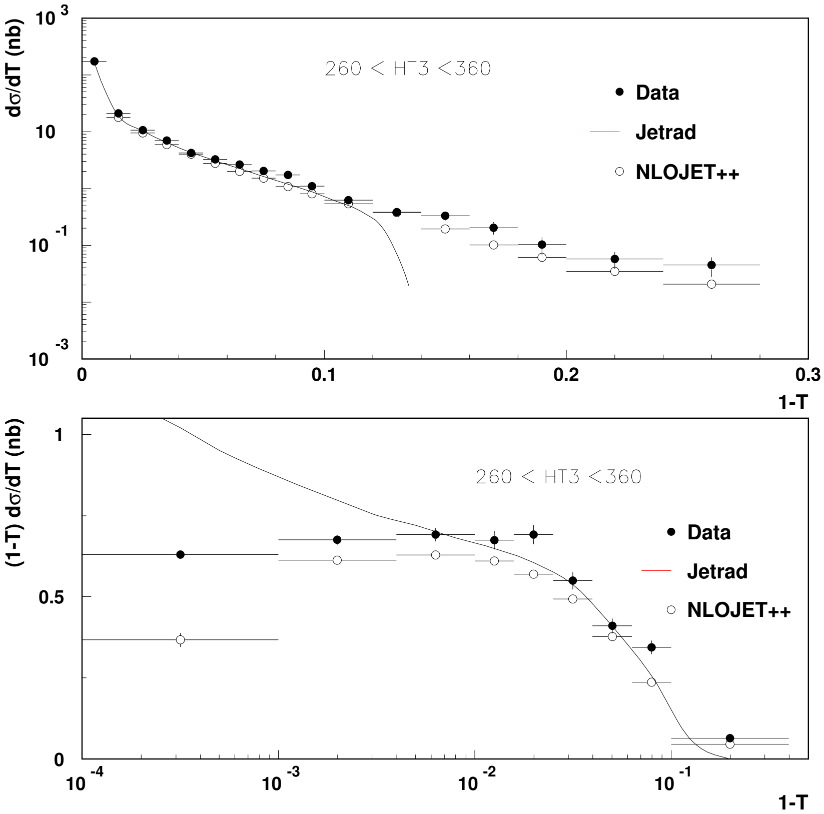

Figure 8.22: Data and NLO three jets NLOJET++ cross sections. JETRAD predictions are also shown for comparison. Only statistical errors are plotted.

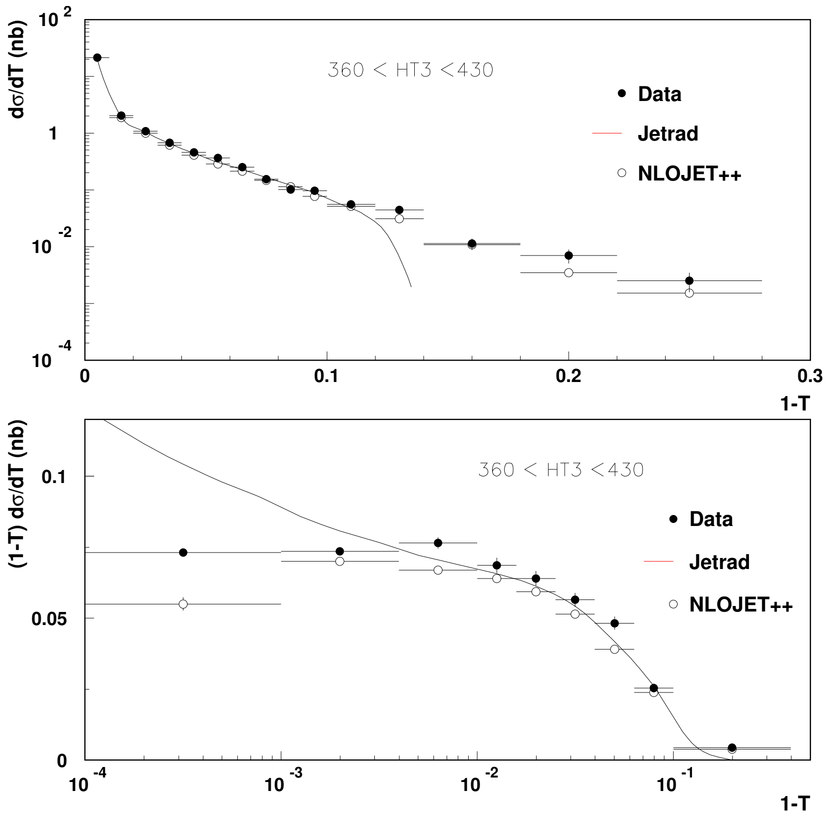

Figure 8.23: Data and NLO three jets NLOJET++ cross sections. JETRAD predictions are also shown for comparison. Only statistical errors are plotted.

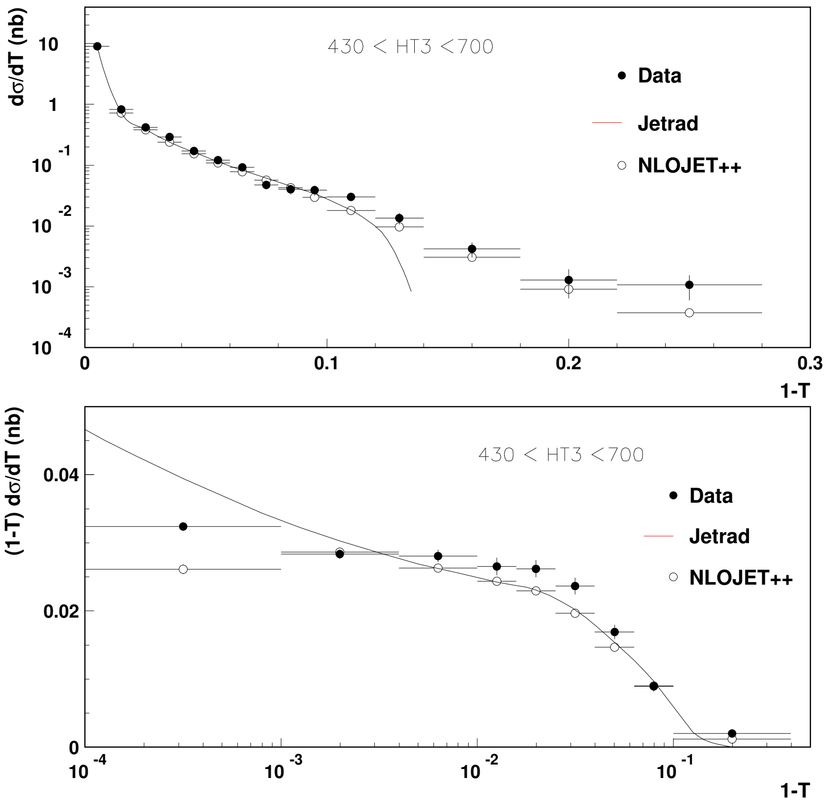

Figure 8.24: Data and NLO three jets NLOJET++ cross sections. JETRAD predictions are also shown for comparison. Only statistical errors are plotted.

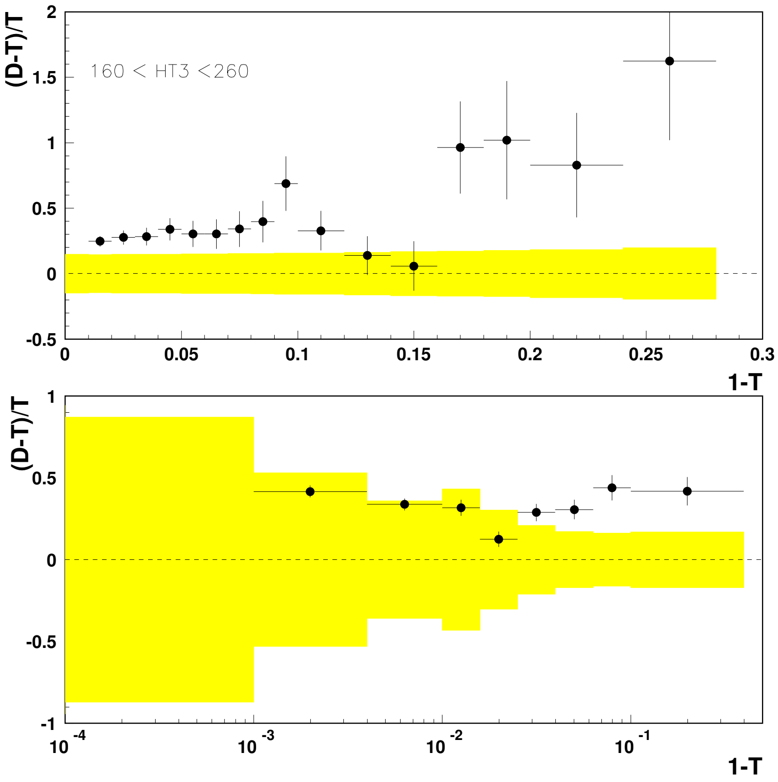

Figure 8.25: Data comparison with NLO 3 jets NLOJET++ prediction. The bars correspond to the statistical errors while the bands are the systematic ones.

Thrust Range (1-T)	χ^2	ndof	Prob(%)
0.01–0.12	6.10	10	80.67
0.01–0.14	6.78	11	81.66
0.01–0.28	15.15	16	51.36
$10^{-2.4} - 10^{-1.2}$	3.19	5	67
$10^{-3.0} - 10^{-1.2}$	6.26	6	39.5
$10^{-4.0} - 10^{-1.2}$	28.86	7	0.01
$10^{-4.0} - 10^{-0.4}$	30.5	9	0.03

Table 8.14: Results of the χ^2 test between data and NLOJET++ predictions, for different ranges in T_2^t .

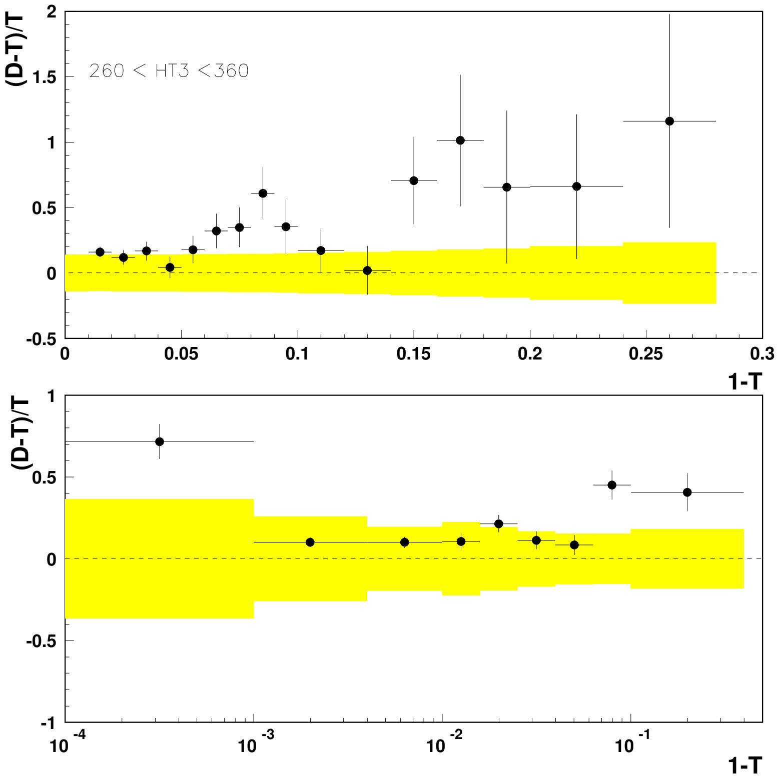

Figure 8.26: Data comparison with NLO 3 jets NLOJET++ prediction. The bars correspond to the statistical errors while the bands are the systematic ones.

Thrust Range (1-T)	χ^2	ndof	Prob(%)
0.01–0.12	10.63	10	38.7
0.01–0.14	11.16	11	43
0.01–0.28	16.75	16	40.2
$10^{-2.4} - 10^{-1.2}$	2.00	5	84.9
$10^{-3.0} - 10^{-1.2}$	2.35	6	88.48
$10^{-4.0} - 10^{-1.2}$	8.25	7	31.10
$10^{-4.0} - 10^{-0.4}$	16.37	9	5.6

Table 8.15: Results of the χ^2 test between data and NLOJET++ predictions, for different ranges in T_2^t .

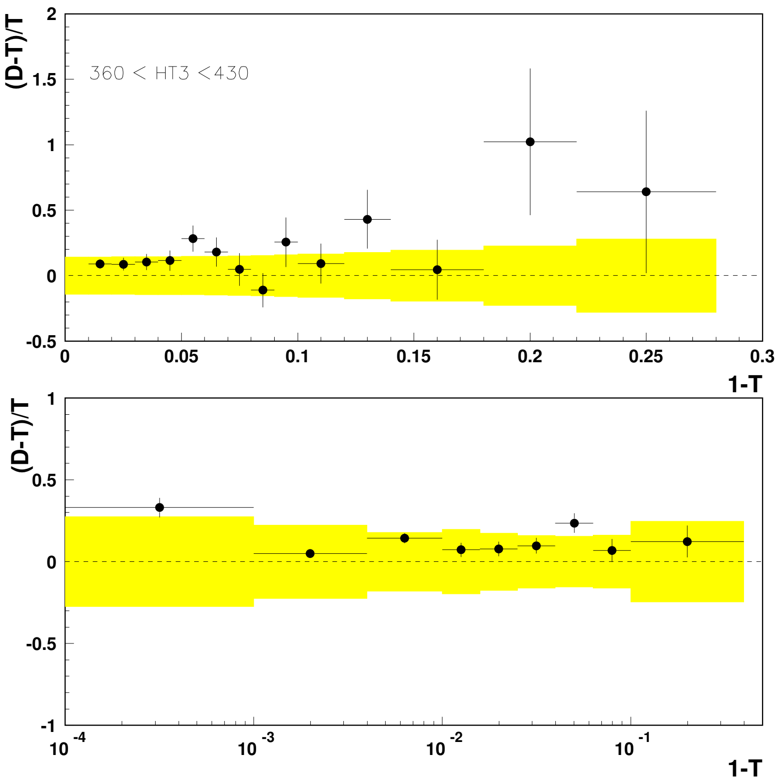

Figure 8.27: Data comparison with NLO 3 jets NLOJET++ prediction. The bars correspond to the statistical errors while the bands are the systematic ones.

Thrust Range (1-T)	χ^2	ndof	Prob(%)
0.01–0.12	7.19	10	70.74
0.01–0.14	9.32	11	59.24
0.01–0.28	11.28	14	66.4
$10^{-2.4} - 10^{-1.2}$	3.19	5	67.07
$10^{-3.0} - 10^{-1.2}$	3.19	6	78.46
$10^{-4.0} - 10^{-1.2}$	3.89	7	79.24
$10^{-4.0} - 10^{-0.4}$	3.9	9	91.78

Table 8.16: Results of the χ^2 test between data and NLOJET++ predictions, for different ranges in T_2^t .

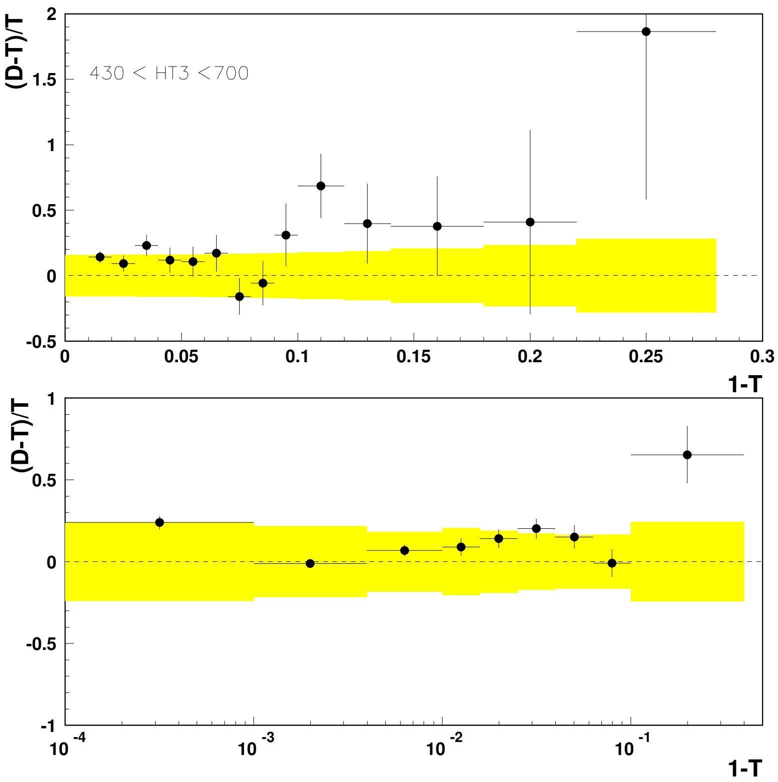

Figure 8.28: Data comparison with NLO 3 jets NLOJET++ prediction. The bars correspond to the statistical errors while the bands are the systematic ones.

Thrust Range (1-T)	χ^2	ndof	Prob(%)
0.01–0.12	13.1	10	21.81
0.01–0.14	13.76	11	24.65
0.01–0.28	14.38	14	42.2
$10^{-2.4} - 10^{-1.2}$	2.44	5	78.55
$10^{-3.0} - 10^{-1.2}$	4.54	6	60.40
$10^{-4.0} - 10^{-1.2}$	4.54	7	71.59
$10^{-4.0} - 10^{-0.4}$	8.79	9	45.68

Table 8.17: Results of the χ^2 test between data and NLOJET++ predictions, for different ranges in T_2^t .

The χ^2 probabilities indicate that data and NLOJET++ predictions agree in the range [0.01-0.28] and the trend for the data to be systematically above the prediction is well within the experimental systematic uncertainties that, to first order, correspond to a global scale factor.

In the logarithmic scale, the agreement extends up to 10^{-4} for the two highest HT3 bins but only up to 10^{-3} for the two lowest ones, indicating the importance of resummation corrections at low HT3.

The difference observed between the prediction and data, which is of order of 30% at low HT3, has been already seen at DØ, in [42]. The inclusive jet cross section measured using $k_\perp$ was found to be above the NLO prediction (which in this case is of $O(\alpha_s^3)$) and the cone cross section at low p_T . This effect is not fully understood. On one hand, a 5% (2%) difference in jet $p_T$was measured between cone and $k_\perp$ jets at 90 GeV (250 GeV), which would explain 25% of the observed discrepancy between their corresponding cross sections ($\sigma \sim {p_T}^{-5}$). The fact that $k_\perp$ are more energetic that the cone ones, especially at low p_T, can be partially explained as a consequence of how hadronization affects the different kind of jets. MC studies have shown that particle $k_\perp$ jets are more energetic than their partners at the parton level, while for cone it is the other way around. This effect can however explain only 5% of the excess seen at low p_T between the theoretical prediction and data for $k_\perp$.

8.3 Conclusions

We have presented the first measurement of the Dijet Transverse Thrust cross section in a $p\overline{p}$ collider at $\sqrt{s} = 1.8$ TeV, using the DØ detector. The Thrust variable, previously measured in e^+e^- and ep experiments, has been adapted to overcome the noisy nature of hadron colliders. It is measured using only the two leading jets in the event and presented in four HT3 bins. This observable has proved to be an excellent tool to test not only NLO perturbative QCD but also predictions of higher orders since the LO contribution for the range $\sqrt{2}/2 \leq T_2^t < \sqrt{3}/2$ is of order α_s^4. This is the first measurement with this characteristics at DØ.

We find good agreement with fixed-order $O(\alpha_s^3)$ perturbative QCD predictions, except at high T_2^t, where resummation corrections are expected to be important, and below $T_2^t \simeq \sqrt{3}/2$, where the leading order diagrams contributing to T_2^t are $O(\alpha_s^4)$. The data show a very good level of agreement with a recent Next-to-Leading pQCD three jet generator which covers the full T_2^t range, except for the $T_2^t = 1$ point since the two loop $2 \rightarrow 2$ parton diagrams are not yet implemented in the theory.

Appendix A

Calculating Thrust

The algorithm implemented to calculate Thrust is based on Ref. [35], which has been developed to reduce the calculating time, in experiments such as e^+e^- colliders, from 2^N, where N is the number of particles involved, to N^2. The problem to solve is to find the axis that maximizes $\sum_i |\vec{p_i} \cdot \hat{n}|$. This can be done by taking a set of signs s_i for $i = 1, N$ and $s_i = 1$ or -1, and forming for all sign combinations $|\sum_i s_i \vec{p_i}|$. It can be demonstrated that $max_{\{s_i\}} |\sum_i s_i \vec{p_i}| = max \sum_i |\vec{p_i} \cdot \hat{n}|$ and that the thrust axis is along the direction $\sum_i s_i \vec{p_i}$. The author proposes a method to reduce the number of combinations and therefore the computing time. However, when two particles are considered there are only two possible combinations. Let's analyze this case.

The numerator of equation 1.8 reduces to:

$$max_\theta \left(|p_{x_1} \cos\theta + p_{y_1} \sin\theta| + |p_{x_2} \cos\theta + p_{y_2} \sin\theta|\right) \tag{A.1}$$

where θ indicates the direction of the unit vector $\hat{n}$. By defining $s_{1(2)} = sign(p_{x_{1(2)}} \cos\theta + p_{y_{1(2)}} \sin\theta)$, equation A.1 can be written as:

$$max_\theta \left[s_1 \left(p_{x_1} \cos\theta + p_{y_1} \sin\theta\right) + s_2 \left(p_{x_2} \cos\theta + p_{y_2} \sin\theta\right)\right] = \tag{A.2}$$

$$max_\theta \left[(s_1 p_{x_1} + s_2 p_{x_2}) \cos\theta + (s_1 p_{y_1} + s_2 p_{y_2}) \sin\theta\right] \tag{A.3}$$

This is equivalent to the scalar product between $\hat{n}$ and a vector $\vec{p_0}$ whose components are the four possible combinations $p_{0x} = s_1 p_{x_1} + s_2 p_{x_2}$ and $p_{0y} = s_1 p_{y_1} + s_2 p_{y_2}$.

It is clear that the maximum is attained when the direction of $\hat{n}$ is the same as $\vec{p_0}$. Thus $\tan\theta = p_{0y}/p_{0x}$ and equation A.3 transforms to:

$$max_{s_1,s_2}\sqrt{(p_{0x})^2 + (p_{0y})^2} = max_{s_1,s_2}|\sum_i^2 s_i\,\vec{p_i}| \tag{A.4}$$

So, the four combinations give only two possible solutions by adding or subtracting the vectors $\vec{p_1}$ and $\vec{p_2}$. The maximum is obtained when either the angle between the vectors is 0° or 180° and the minimum when they are at 90°. In the first case Thrust is equal to one. In the second one, T is given by:

$$T = \frac{\sqrt{1 + (\frac{|\vec{p_2}|}{|\vec{p_1}|})^2}}{1 + \frac{|\vec{p_2}|}{|\vec{p_1}|}} \tag{A.5}$$

The minimum Thrust is obtained when $|\vec{p_1}| = |\vec{p_2}|$ and is equal to $\sqrt{2}/2$. The axis in this case is located at 45° between $\vec{p_1}$ and $\vec{p_2}$.

Appendix B

Luminosity Dependence Study

As it was explained in section 7.1, a luminosity study was performed in order to analyze the global effect of various sources of systematics. The data sample for each jet trigger was divided into two subsamples (of comparable statistic) of different instantaneous luminosity. The integrated luminosities (L) of each subsample were extracted from the PDB. Since the results of the PDB are not accurate for Jet_30 and Jet_50, several cross checks were done. Figures B.1–B.4 show the ratios between the E_T spectra of the leading jet (et1) for the different subsamples of each trigger. The fits were done from the value of et1 where the triggers become fully efficient. As it is explained in [38], no luminosity dependence is expected for the leading jet. The same conclusion can be inferred from the fact that in all plots the ratio is flat, otherwise, the relative effect should be different for high and low E_T. In order to extract the value of L, in the cases where the ratio fit is not consistent with unity, a normalization factor was extracted for one of the subsamples (the high one). The bottom plots present the ratios corresponding to HT3, for events that pass the et1 threshold, where the distributions have been normalized using the factor obtained from the et1 ratios. All curves were fitted with a constant function. The fits are flat and consistent with unity.

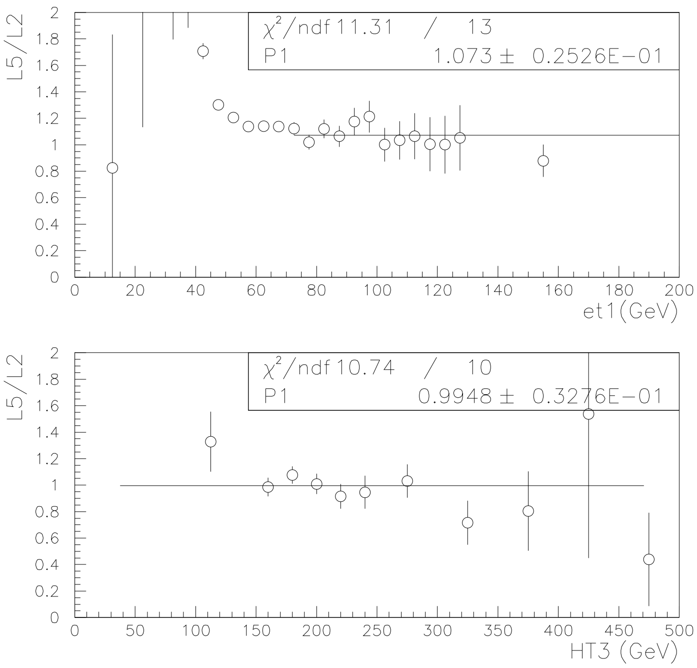

Figure B.1: Top: Ratio between the leading jet E_T spectra for two subsamples of Jet_30 . Bottom: Ratio between the HT3 spectra, for the same subsamples, the distributions have been normalized to account for inaccuracies on PDB results.

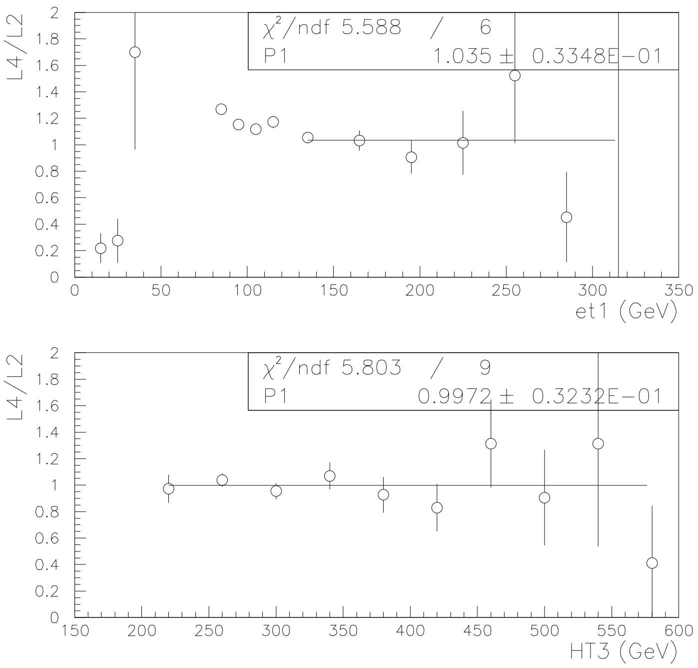

Figure B.2: Top: Ratio between the leading jet E_T spectra for two subsamples of Jet_50 . Bottom: Ratio between the HT3 spectra for the same subsamples, the distributions have been normalized to account for inaccuracies on PDB results.

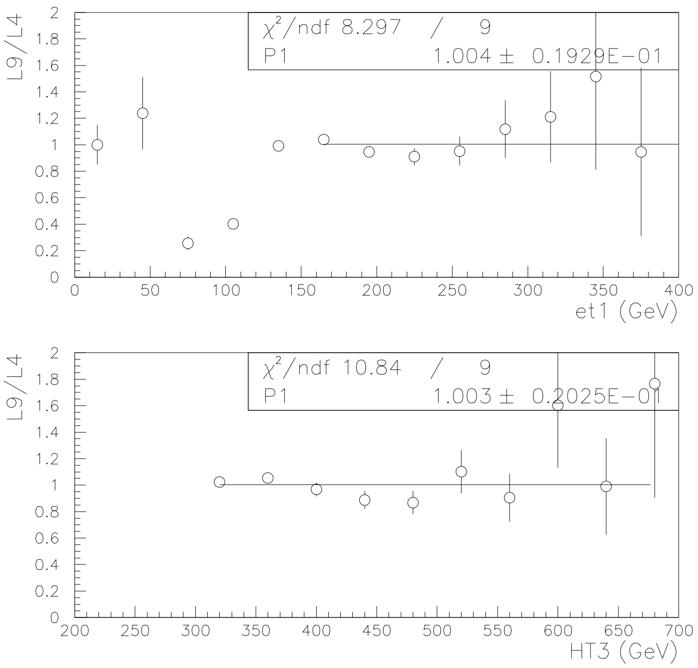

Figure B.3: Top: Ratio between the leading jet E_T spectra for two subsamples of Jet_85 . Bottom: Ratio between the HT3 spectra for the same subsamples, the distributions have been normalized to account for inaccuracies on PDB results.

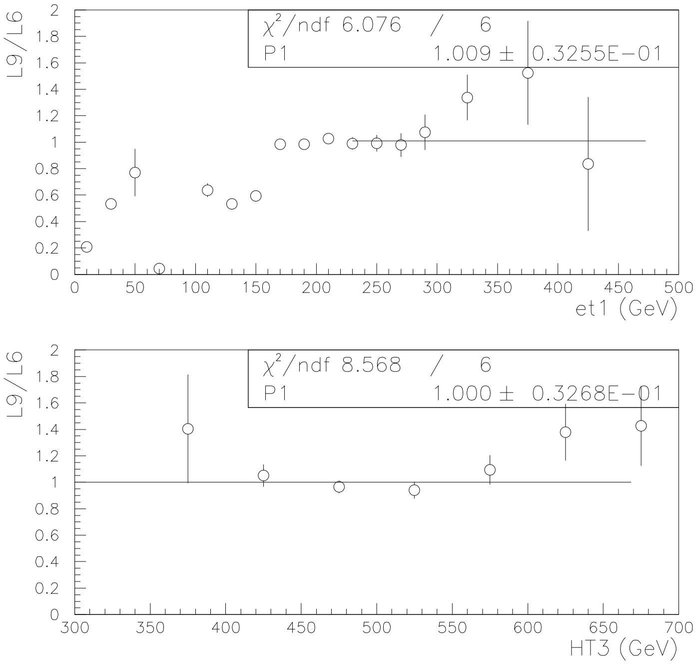

Figure B.4: Top: Ratio between the leading jet E_T spectra for two subsamples of Jet_Max . Bottom: Ratio between the HT3 spectra for the same subsamples, the distributions have been normalized to account for inaccuracies on PDB results.

Bibliography

[1] S.L. Glashow, Nucl. Phys. 22, 579 (1961).
S. Weinberg, Phys. Rev. Lett. 19, 1264 (1967).
A. Salam, in "Elementary Particle Physics", Nobel Symp. No. 8, ed. N. Svartholm, Almqvist and Wilsell, Stockolm (1968).

[2] K. Hagiwara *et al.* Phys. Rev. D 66, 010001 (2002).

[3] R.E. Taylor, H.W. Kendall and J.J. Friedman, "Lectures on the occasion of the presentation of the 1990 Nobel Prize in Physics", Rev. Mod. Phys. 63 (1991) 573.

[4] V. Barger and R. Phillips, *Collider Physics*, Frontiers in Physics Lecture Note Series, Addison-Wesley, 1987.

[5] G.'t Hooft and M. Veltman, Nucl. Phys. B (1972) 189.

[6] G.C. Blazey *et al.*, Run II Jet Physics: Proceedings of the Run II QCD and Weak Boson Physics Workshop, Batavia, Illinois, 4-6 Nov (1999) hep-ex/0005012.

[7] J. Huth *et al.*, in Proceedings of Research Directions for the Decade, Snowmass, 1990, edited by E.L. Berger (World Scientific, Signapore, 1992).

[8] S.D. Ellis, Z. Kunszt and D.E. Soper, Phys. Rev. Lett. **69** , 3615 (1992).

[9] M.H. Seymour, presented at the XXXIst Rencontres de Moriond, Moriond, Les Arcs, March 21-28 (1998) hep-ph/9807226.

[10] S. Catani, Yu.L. Dokshitzer and B.R. Webber, Phys. Lett. B **285**, 291 (1992)

[11] S. Catani, Yu.L. Dokshitzer, M.H. Seymour and B.R. Webber, Nucl. Phys. B **406**, 187 (1993)

[12] S.D. Ellis and D.E. Soper, Phys. Rev. D **48**, 3160 (1993)

[13] E.W.N. Glover and D.A. Kosower, Phys. Lett. B **367**, 369 (1996)

[14] ALEPH Collaboration, D. Decamp et al., Phys. Lett **B234** (1990) 399, Phys. Lett **B255** (1991) 623
DELPHI Collaboration, P. Aarnio et al., Phys. Lett. **B240** (1990) 271
L3 Collaboration, B. Adeva et al., Phys. Lett. **B237** (1990) 136
OPAL Collaboration, M.Z. Akrawy et al., Phys. Lett. **B235** (1990) 389,Z. Phys. **C47** (1990) 505
TASSO Collaboration, W. Bartel et al., Z.Phys. **C33** (1990) 187

[15] OPAL Collaboration, K. Ackerstaff et al., Z.Phys. **C75** (1997) 193
DELPHI Collaboration, P. Abreu et al., Z.Phys. **C73** (1997) 229
H1 Collaboration, C. Adloff et al., Phys.Lett. **B406** (1997) 256
K. Rabbertz and U. Wollmer hep-ex/0008006
G. J. McCance hep-ex/0008009
G.P.Korchemsky and S.Tafat hep-ph/0007005
Y. Dokshitzer hep-ph/9911299
O. Biebel, P. Movilla and S. bethke, Phys.Lett. **B459** (1999) 326
S. Catani, L. Trentadue, G. turnock and B. Webber Phys.Lett. **B263** (1991) 491
G.P.Korchemsky and G.Sterman,Nucl.Phys. **B555** (1999) 335

[16] DELPHI collaboration P. Abreu and others, Zeit. Phys, **C59** (1993) 21

[17] W.T. Giele, E.W.N. Glover, and D.A. Kosower, Phys. Rev. Lett. **73** , 2019 (1994).

[18] Z. Nagy, hep-ph/0110315

[19] H.L. Lai *et al.*, Phys. Rev. D **55**, 1280 (1997).

[20] W.B. Kilgore and W.T. Giele, hep-ph/9903361

[21] G. Marchesini, B.R. Webber, G. Abbiendi, I.G. Knowles, M.H. Seymour and L. Stanco, Computer Phys. Commun. **67**, 465 (1992)

[22] M. H. Seymour, Comput. Phys. Commun. 90 (1995) 95.

[23] B.R. Webber, Nucl. Phys. B 238 (1984) 492.

[24] J. Thompson, "Introduction to colliding beams at Fermilab", Fermilab Tech. Memo, FERMILAB-TM-1909 (1994).

[25] S. Abachi *et al.* (DØ Collaboration), Nucl. Instr. Meth. Phys. in Res. A **338**, 185 (1994).

[26] G. Manning *et al.*, "The DØ Software Documentation", Calorimeter Reconstruction Section (1995).

[27] B. Abbot, G. Watts, DØ Internal Note ♯3006, (1996).

[28] B. J. May, "Rapidity Gaps between Jets in $p\overline{p}$ Collisions at $\sqrt{s} = 1.8$ TeV", Ph.D. Dissertation (1994).

[29] R. Brun and F. Carminati, "GEANT Detector Description and Simulation Tool", CERN Program Library Long Writeup W5013 (1993).

[30] W. Dharmaratne, R. Raja and C. Stewart, DØ Internal Note ♯1730, (1993); W.J. Womersley, R. Raja and A.M. Jonckheere, DØ Internal Note ♯650, (1987)

[31] B. Abbott *et. al.*, Nucl. Instr. and Methods A **424**, 352 (1999)

[32] B. Abbott *et. al.*, DØ Internal Note ♯3585, (1999).

[33] B. Abbott, *et. al.*, DØ Internal Note ♯3287, (1997).

[34] HERWIG 5.9, hep-ph/9607393; G. Marchesini (Milano), B.R. Webber (Cambridge), G. Abbiendi (Padova), I.G. Knowles (Glasgow), M.H. Seymour (CERN), L. Stanco (Padova)

[35] H. Yamamoto, J. Comput. Phys.**52**, (1983)

[36] D. Chakraborty, DØ News ♯3750, (1995)

[37] L. Babukhadia and others, DØ Internal Note ♯3408, (1998)

[38] L. Babukhadia, "Rapidity Dependence of the Single Inclusive Jet Cross Section in $p\bar{p}$ Collisions at $\sqrt{s} = 1.8$ TeV with the DØ Detector", Ph.D. Dissertation, University of Arizona, (1999)

[39] V.D. Elvira, "Measurements of the Inclusive Jet Cross Section at $\sqrt{s} = 1.8$ TeV with the DØ Detector", Ph.D. Dissertation, Universidad de Buenos Aires, (1994)

[40] G. Blazey and R. Hirosky, DØ Internal Note ♯3276

[41] M. Strang, private Communication

[42] S. Grinstein, "The inclusive Jet Cross Section using the $k_\perp$ algorithm" Ph.D. Dissertation, Universidad de Buenos Aires, (2003)

[43] S .Chopra and L. Lueking, private communication.

[44] V.D. Elvira, DØ Internal Note ♯2173 (1994)

[45] Statistical Data Analysis, Glen Cowan, Section 11.3

[46] See http://www.df.uba.ar/∼vsorin/

[47] B. Abbott *et al.* (DØ Collaboration), Phys. Rev. D 64, 032003 (2001).

[48] R. Keith Ellis, W. James Stirling and Bryan R. Webber, *QCD and Collider Physics*, Cambridge Monographs on Particle Physics, Nuclear Physics and Cosmology (1996), Cambridge University Press.